Deep Tissue Fluorescence Imaging with Time-Reversed Light

Thesis by

Ying Min Wang

In Partial Fulfillment of the Requirements for the Degree

of

Doctor of Philosophy

CALIFORNIA INSTITUTE OF TECHNOLOGY

Pasadena, California

2013

(Defended March 20, 2013)

To my family.

Acknowledgements

I am extremely grateful to my advisor, Professor Changhuei Yang. I had no previous experience in optics, but Yang took a chance on me by offering a studentship. More than just giving me the opportunity though, Yang's tireless guidance, encouragement and enthusiasm for science have been instrumental to the growth of my technical competence and scientific confidence. I realize that having a mentor who believes in me is not an everyday occurrence, but a rare blessing.

My committee members Professor Scott E. Fraser, Professor Chin-Lin Guo, Professor Viviana Gradinaru and Professor Hyuck Choo have been extremely supportive. I am very grateful for their invaluable insights and generous help. In particular, I would like to thank Professor Fraser, who has given me a lot of advice and encouragement in my scientific endeavors.

You will find that this thesis contains a lot of work that I have done together with Dr. Benjamin Judkewitz. Our collaboration has been far more fruitful and enjoyable than I could have hoped for. I have learned a lot from our collaboration, and in addition I am extremely thankful for his friendship. Besides Benjamin, Roarke Horstmeyer, Dr. Alexendre Mathy and Professor Charles A. DiMarzio have also contributed to work described in this thesis and I would like to gratefully acknowledge their efforts. The specific contributions of all my co-authors will be noted at the beginning of the relevant chapters. Professor Ivo Vellekoop provided important insights during his visits to our lab and via email correspondences, for which I am very grateful.

I would like to express my gratitude towards all members of the Biophotonics Lab (both past and present) for their camaraderie and generous help, especially Dr. Benjamin Judkewitz, Dr. Emily McDowell, Dr. Xiquan Cui, Dr. Guoan Zheng, Dr. Jian Ren, Roarke

Horstmeyer, Mooseok Jang, Haojiang (Edward) Zhou, Xiaoze Ou, Dr. Shuo Pang, Seung Ah Lee, Dr. Jigang Wu, Dr. Lap Man Lee, and Chao Han. I have benefited much from being in the company of these extremely talented and driven scientists. Anne Sullivan, our lab mom, has really lived up to that title, providing seamless administrative support and taking good care of everyone's wellbeing.

I am very grateful to my parents, who always believed in me and supported my life choices. I would like to thank them for sharing the joy of my successes and putting my failures in proper positive contexts. I am extremely thankful for my husband, Kelvin. His love, patience and off-the-charts optimism (ironically, an attribute I often complain about) has sustained me through this journey. I also thank my parents-in-law for understanding why we have to be away from them for so long and for believing in our visions for our future.

There is really nothing like confiding in and being cheered on by friends who have themselves taken the arduous journey. Kim, Shawn, Fongtian, Brian, Mingzi, and Limei: thank you so much for listening to my crazy rants and sharing my joy. There are probably few better tests of friendship than forcing people who are not graduate students to empathetically listen to the woes and joys of graduate school. Weyling, Carine (Ng), Carine (Lim), and Rachel: you guys are great. Also, I have been blessed with the good fortune to get to know artists whose passion and tenacity in the pursuit of their art forms inspired me to do the same in science: Nena and Cihtli, thank you!

Lastly, I would like to acknowledge support from the National Science Scholarship, awarded by the Agency for Science, Technology and Research, Singapore.

Abstract

Advances in optical techniques have enabled many breakthroughs in biology and medicine. However, light scattering by biological tissues remains a great obstacle, restricting the use of optical methods to thin *ex vivo* sections or superficial layers *in vivo*. In this thesis, we present two related methods that overcome the optical depth limit—digital time reversal of ultrasound encoded light (digital TRUE) and time reversal of variance-encoded light (TROVE). These two techniques share the same principle of using acousto-optic beacons within tissues for time reversal optical focusing. Ultrasound, unlike light, is not significantly scattered in soft biological tissues, allowing for ultrasound focusing within biological samples. In addition, a fraction of the scattered optical wavefront that passes through an ultrasound focus gets frequency-shifted via the acousto-optic effect. Thus, light passing through the ultrasound focus essentially becomes a virtual source of frequency-shifted light inside the tissue. The scattered ultrasound-tagged wavefront can be selectively measured outside the tissue and time-reversed to form an optical focus at the location of the ultrasound focus within the tissue. In the original implementation by Xu et al., a photorefractive crystal is used as the time reversal mirror. Due to the limitations in reflectivity of the photorefractive crystal, the time-reversed optical focus is relatively low intensity and thus only allows absorption characterization of the sub-millimeter scale focused spot.

In digital TRUE, we time-reverse ultrasound-tagged light with an optoelectronic time reversal device (the digital optical phase conjugate mirror, DOPC). The use of the DOPC enables high optical gain, allowing for high intensity optical focusing and focal fluorescence imaging inside complex media. To illustrate the potential of our method, we image complex fluorescent objects and tumor microtissues at an unprecedented depth of ~ 2.5 mm in biological tissues at a lateral resolution of 36 μm by 52 μm. This demonstration sets the stage

for a wide range of deep tissue imaging applications in biomedical research and medical diagnostics. Although digital TRUE is a simple conceptual improvement to the original demonstration, its implementation is technically challenging. Here, we will also discuss these technical challenges and touch upon future improvements and limitations.

The resolution of the TRUE approach is fundamentally limited to that of the wavelength of ultrasound. As a result, the ultrasound focus (~ tens of microns wide) usually contains hundreds to thousands of optical modes, such that the scattered wavefront measured is a linear combination of the contributions of all these optical modes. In TROVE, we make use of our ability to digitally record, analyze and manipulate the scattered wavefront to demix the contributions of these spatial modes using variance encoding. In essence, we encode each spatial mode inside the scattering sample with a unique variance, allowing us to computationally derive the time reversal wavefront that corresponds to a single optical mode. In doing so, we uncouple the system resolution from the size of the ultrasound focus, demonstrating optical focusing and imaging between highly diffusing samples at an unprecedented, speckle-scale lateral resolution of ~ 5 μm. Our methods open up the possibility of fully exploiting the prowess and versatility of biomedical optics in deep tissues.

Table of Contents

Acknowledgements iv

Abstract vi

List of Figures xi

Chapter 1 Introduction 1

1.1 Interaction of Light with Tissues: Effect of Scattering and Absorption 1

1.2 Methods to Overcome Scattering 6

1.3 Digital Time Reversal of Ultrasound-Encoded and Variance-Encoded Light 11

1.4 Outline of Thesis 13

Appendix: Some Important Concepts 14

References 19

Chapter 2 Introduction to Optical Phase Conjugation 22

2.1 Principles of Optical Phase Conjugation 22

2.2 Deviations from the Ideal 25

2.3 Conventional Phase Conjugate Mirrors 26

2.4 Previous Work in Turbidity Suppression Using Optical Phase Conjugation 31

2.5 Perspectives and Relevance 32

References 34

Chapter 3 Principles of Digital Optical Phase Conjugation 36

3.1 Concept and Setup 36

3.2 Partial Phase Conjugation 44

3.3 Sample Motion 51

3.4 Conclusions and Outlook 56

References 57

Chapter 4 Deep Tissue Focal Fluorescence Imaging with Digitally Time-reversed Ultrasound-encoded Light 59

4.1 Introduction 59

4.2 Setup and Principles 61

4.3 Results 65

4.4 Discussion 70

4.5 Methods 72

Appendix: Full Setup Diagram 81

References 82

Chapter 5 Speckle-scale Focusing in the Diffusive Regime with Time-reversal of Variance-encoded Light (TROVE) 86

5.1 Introduction 87

5.2 Principles 88

5.3 Results 93

5.4 Discussion 96

5.5 Methods 98

Appendix: Supplementary Methods 104

References 112

Chapter 6 Future Work and Conclusion 114

6.1 Future Work 114

6.2 Conclusion 121

References 122

Appendix: Building a DOPC 123

List of Figures

	Page
1.1 Optical phase conjugation	10
1.2 The concept of time reversal of ultrasound-encoded light (TRUE)	12
1.3 Speckles within the ultrasound focus	13
1.4 Speckle intensity pattern projected onto a CCD sensor with an objective lens	14
1.5 Transmission matrix representation of light propagation	16
2.1 Comparison between a phase conjugate mirror and a conventional mirror	23
2.2 Static holography	28
2.3 Schematic of degenerate four-wave mixing and stimulated Brillouin scattering	31
3.1 First generation DOPC system	39
3.2 Second generation DOPC system	41
3.3 Intuitive explanation of peak to background ratio	45
3.4 Representative area of a typical phase map	50
3.5 Results of typical DOPC experiment	50
3.6 Schematic of DOPC setup for decorrelation measurements	53
3.7 Phase conjugate focus decay with time due to sample decorrelation	54
4.1 Schematic of the imaging principle	63
4.2 Demonstration of optical focusing between thick layers of biological tissue	66
4.3 Demonstration of point-spread-function	69
4.4 Fluorescence imaging of complex objects	70
4.5 Timing of acquisition	77

4.6 Effects of coherence length 78

4.A Setup diagram 81

5.1 Schematic comparison of TRUE and TROVE focusing 89

5.2 Characterization of frequency-shifted wavefronts at the ultrasound plane 91

5.3 Visualization of speckle-scale focusing 94

5.4 Point spread function and image acquisition 96

5.5 Setup diagram 103

5.A Variance encoding of optical transmission modes 106

6.1 Plot of ultrasound attenuation with depth and frequency 117

A.1 Detailed schematic of a typical DOPC system 123

A.2 Imaging the SLM onto the camera 126

A.3 A typical SLM phase curvature compensation map 128

A.4 Dots displayed and imaged for fine alignment 129

Chapter 1
Introduction

Optical methods occupy an important niche amongst the many forms of biomedical imaging and analysis techniques available today. The sub-micrometer diffraction limited resolution of light allows for visualization of cellular and subcellular structures and processes. Recent developments of super-resolution techniques further enable nanometer-scale resolution. [1-3] In addition, the range of molecular tools and sources of intrinsic optical contrast provide for high biochemical specificity and information output in optical imaging studies. Aside from imaging and sensing, there is also growing interests in the utility of light for the control and manipulation of biological systems, for example with optogenetics, [4,5] and optical tweezers. [6,7]

Although instrumental to many biomedical breakthroughs, these optical tools fail at large tissue depths. This is because as light propagates through biological tissues, refractive index inhomogeneities cause diffuse scattering of light that increases with depth. As a result, the application of optical methods beyond thin sections or superficial tissue layers is a tremendous challenge. In this chapter, we provide an overview of light-tissue interactions, discuss the current methods used in overcoming optical scattering, and finally introduce the methods presented in this thesis.

1.1 INTERACTION OF LIGHT WITH TISSUES: EFFECT OF SCATTERING AND ABSORPTION

Light interacts with tissue in two main ways—absorption and scattering. Compared to absorption, scattering dominates tissue-light interactions. [8] Here, we discuss the origins and characteristics of scattering and absorption in the context of biological tissues.

Absorption

When a molecule within the tissues (e.g. water, hemoglobin, melanin, bilirubin, deoxyribonucleic acids) absorbs light, it is elevated from a lower energy level E_1 to a higher energy level E_2 [9,10]. The difference between these two energy levels is equal to the energy in the photon absorbed, such that

$$E_2 - E_1 = h\frac{c}{\lambda} \tag{1.1}$$

where h is the Planck's constant, c is the speed of light (3 x 10^8 m/s) and λ is the wavelength of light. Molecules in this elevated energy state can release some energy released through non-radiative mechanisms, and the rest can be released in the form of another photon of lower energy (thus, longer wavelength). This is the basis of many optical contrast mechanisms (e.g. fluorescence, phosphorescence, Raman scattering etc.) that enables biomolecular-specific detection and imaging. Energy transfer to a neighboring molecule can also occur and is the basis of fluorescence resonance energy transfer (FRET) [11]. [15]

The absorption cross-section σ_a [mm^2] of a single absorber describes the effective area of the particle that absorbs light [10]

$$\sigma_a = \frac{P_a}{I_o} \tag{1.2}$$

where P_a is the power absorbed [J·s^{-1}] and $I_o$is the intensity of incident light [J·s^{-1}·mm^{-2}]. The absorption cross section is a conceptual description of the ability of a chromophore to absorb light. The absorption cross section is generally smaller than the geometrical cross section of the chromophore. [10]

When there is a collection of a particular specie of chromophore with the same absorption cross section distributed within three-dimensional sample, the absorption characteristics of the sample per length is described by the absorption coefficient μ_a [mm^{-1}] and the absorption mean free path l_a [mm]: [10]

$$\mu_a = \sigma_a N \tag{1.3a}$$

$$l_a = \frac{1}{\mu_a} \tag{1.3b}$$

where N is the density of chromophores per unit volume [mm^{-3}]. It is often useful to quantify the intensity decay as light travels through an absorptive medium of a certain thickness. To do so, we express dI as the intensity change as light travels through an absorbing material with absorption coefficient μ_a and thickness dl: [10]

$$\frac{dI}{I} = -\mu_a dl \tag{1.4a}$$

Integrating equation (1.4a), we obtain the familiar Beer-Lambert law: [10]

$$I(l) = I_o \exp(-\mu_a l) \tag{1.4b}$$

where I_o is the light intensity incident on the material and $I(l)$ is the transmitted intensity after traveling length l of the sample. We need to keep in mind that the above discussion considers the interaction of a particular type of chromophore with a specific wavelength of light. To fully describe the absorption behavior of a biological tissue, we have to consider all the chromophores in the tissue and their spectral responses.

Elastic scattering

Scattering originates from refractive index inhomogeneities within the tissue; for example, at the interface of lipid membranes and cytosols, and of collagen matrices and its aqueous surroundings. [9,10] Unlike in the process of absorption, elastically scattered light does not lose energy. Instead, the scattered light is deflected from its path. Similar to absorption, scattering properties of the single scatterer are dependent on the scatterer itself and the wavelength of the impinging light. There exist three scattering regimes, depending on the relative size of the scatterer (d) to the wavelength of the incident light (λ). [15]

In the first regime, the scatterer is much larger than the optical wavelength ($d >> \lambda$) such that the bending of the incident light can be fully described by geometric optics. In the

second regime, the Rayleigh regime, the scattering particle is much smaller than the wavelength of light ($d << \lambda$). In the third, known as the Mie regime, the scattering particle is on the order of the wavelength. Biological tissues contain both Mie and Rayleigh scatterers, although Mie scattering dominates. The origins of Rayleigh scattering include subcellular components such as membrane structures and macromolecules, while Mie scattering can be attributed to lysosomes, vesicles, mitochondria etc. [9]

The scattered intensity distributions of Rayleigh scattering events (expressed here in polar coordinates, $I_s(r,\theta)$) are fairly isotropic and can be described as a function of the incident light intensity (I_o) and wavelength (λ), and the respective refractive index of the scatterer and its surrounding medium (n_s and n_m): [10,12]

$$I_s(r,\theta) = 8\pi^4 n_m^4 \left(\frac{n_s^2 - n_m^2}{n_s^2 + 2n_m^2}\right)\frac{a^6}{r^2\lambda^4}(1-\cos^2\theta)I_o \tag{1.5}$$

The inverse dependency on λ^4 indicates preferential scattering of shorter wavelengths in the Rayleigh regime. Mie scattering can be described by the Mie solution to the Maxwell's equations, in which a plane monochromatic wave is incident on an isotropic scatterer in an otherwise homogenous medium. [10] The solutions are in the form of infinite series, describing, amongst other parameters, scattering cross sections and scattering angles. [10,13]

Analogous to absorption, the scattering cross section for a single scatterer σ_s [mm^2] is described as: [10]

$$\sigma_s = \frac{P_s}{I_o} \tag{1.6}$$

where P_s is the power of the scattered light and I_o is the intensity of the incident light. This can be thought of as the effective area that guarantees scattering when a photon impinges. Again, σ_s is not necessarily equal to the physical cross section of the scatterer. In the same manner as in the description of absorption, the scattering coefficient μ_s [mm^{-1}] and the scattering mean free path l_s [mm] are: [10]

$$\mu_s = \sigma_s N \tag{1.7a}$$

$$l_a = \frac{1}{\mu_a} \tag{1.7b}$$

where N is the density of scatterers per unit volume [mm^{-3}]. The decay of ballistic (non-scattered) light intensity as light travels through a scattering medium with scattering coefficient μ_s and thickness l can be derived, obtaining Beer's law for scattering:

$$I(l) = I_o \exp(-\mu_s l) \tag{1.8}$$

where I_o is the light intensity incident on the material. [10]

The angular spread of light scattered off a particle is quantified by the scattering anisotropy g: [10]

$$g = \langle \cos\theta \rangle \tag{1.9}$$

where θ is the scattering angle. The values of g can range from 0 to 1, where a higher value represents more forward scattering. As we have seen in equation (1.5), Rayleigh scatterers are fairly isotropically scattering. In general, Mie scatterers are more forward scattering. However, in considering the anisotropy of a scatterer, the refractive index of the scatterer and the surrounding medium will have to be considered in all cases.

Incorporating the anisotropy of the scatterers, scattering media are sometimes described by their reduced scattering coefficient μ_s' [mm^{-1}] or transport mean free path l_s' [mm] which incorporates the anisotropy of the scatterers such that: [10]

$$\mu_s^{'} = (1 - g)\mu_s \tag{1.10a}$$

$$l_s^{'} = \frac{1}{\mu_s^{'}} \tag{1.10b}$$

The region from the mean free path to the transport mean free path is defined as the quasi-ballistic regime. [10] In this regime, photons are scattered a few times but are just slightly

deflected from their paths. The quasi-diffusive regime is described as between one and ten transport mean free paths, where photons have been scattered many times but still retain some memory of their original directionality. [10] The length scale beyond ten transport mean free paths is defined as the diffusive regime where the photons have scattered so many times that the memory of their original directions are nearly lost. [10]

Again, we need to keep in mind that the above discussion considers the interaction of only one particular type of scatterer with one particular wavelength of light. To fully describe the scattering behavior of a sample, we have to consider all the scatterers in the sample and the complete spectral response. Most biological tissues are significantly scattering in the shorter wavelengths but also highly forward scattering. [8,14]

The problem of scattering

Scattering poses an important and interesting challenge. Unlike in absorption where light is still traveling along the sample path albeit with reduced energy, scattering causes light to be diffused (both spatially and temporally). While the total energy in the diffused beam remains the same, the power in the ballistic component drops exponentially with depth as the power in the scattered component grows. For the purpose of optical imaging, since we can only accurately attribute the spatial origin of the ballistic components by conventional means, scattered light is often considered undesirable noise. In addition, for applications like optogenetics and photodynamic therapy, the reduction of delivered light intensity with depth due to diffuse scattering constitutes a significant challenge.

1.2 METHODS TO OVERCOME SCATTERING

Ballistic light selection—gating out scattered light as noise

Because scattered light is often seen as noise, many methods have been devised to gate out the scattered light, retaining and measuring only the ballistic components. Here, we discuss how this goal is commonly achieved by spatial gating, temporal gating and coherence gating.[15] Temporal gating techniques rely on the fact that the ballistic components

and singly scattering components exit the tissue much quicker than multiply-scattering components due to a shorter path of travel. Thus, illuminating a scattering sample with a short pulse laser and measuring only the early-arriving light components, multiply scattered light can be rejected while retaining information only from the unscattered and singly scattered components. [15, 16]

Spatial gating techniques like confocal microscopy and multiphoton microscopy reject light with significantly altered propagation direction. In confocal microscopy, a pinhole is placed at the conjugate plane of a lens that illuminates a focal volume in the sample. [17] In such a way, ballistic light from the focal volume will pass through the pinhole, while scattered (and out of focus) light will be rejected. The decrease in the number of ballistic photons with depth results in weaker excitation at the focal volume and a decrease in unscattered fluorescence emission admitted through the pinhole. Typically, the maximum imaging depth of confocal microscopy is limited to ~ 2 to 3 mean free paths (~ few hundred micrometers). [15,18]

Multiphoton microscopy works on the premises that (1) longer wavelengths are scattered less, allowing for deeper focusing and (2) only the unscattered light at the optical focus will be intense enough to result in the simultaneous absorption of two [19] (recently even three [20]) photons by fluorophores within the focus, as if a photon of half the wavelength is absorbed. As such, all the fluorescence signals detected can be attributed to the fluorophores at the unscattered optical focus, doing away with the need for a pinhole. This alleviates the signal detection problem. With these two advantages, the penetration depth limit of multiphoton microscopy is ~ 3–4 mean free paths (~a few hundred micrometers to <1 mm).[18]

Optical coherence tomography (OCT) is a well-known coherence gating technique that has found widespread clinical imaging applications in recent years. [21] Using a short coherence length light source, only unscattered light that is reflected from various depths in the sample can significantly interfere with a reference beam that is perfectly pathlength matched with the ballistic light that returns. An important advantage of such interferometric

detection is that the weak reflected ballistic signal can be brought above the shot-noise of the scattered background such that it is only fundamentally limited by its own shot-noise. Making use of this detection advantage, the OCT is typically capable of imaging depths up to a few millimeters, depending on tissue properties. One limitation of OCT is that because the technique requires coherent signals, it does not avail itself to fluorescence detection.

Since the ballistic light component decreases exponentially with depth (see equation (1.8)), the signals obtained with the abovementioned gating techniques will ultimately reach its limits, falling below the detection limits of even the most sensitive detectors beyond superficial depths.

Optical clearing

Optical clearing methods reduce scattering by minimizing the refractive index mismatches in biological samples. [22] This can be achieved, for example, by dehydrating the sample and replacing the aqueous components with organic chemicals that closely match the refractive index of the lipid membranes of the cellular components. Recently, an aqueous clearing agent has been reported, solving the issues of fluorophore quenching and sample shrinkage that are associated with the use of the organic clearing agents. [23] Optical clearing methods have been shown to render *ex vivo* tissues transparent, enabling optical imaging of embryos and whole organs without physical sectioning. [24,25] However, since the clearing processes are currently only applicable to fixed tissues, this strategy is unsuitable for *in vivo* longitudinal studies.

Diffuse optical tomography

In diffuse optical tomography (DOT), measurements of the distribution of scattered light exiting the tissue as a function of varying spatial positions of input light are utilized to construct a model of the optical properties of the sample. [10,26] This results in a large dataset with which a model of light propagation in a tissue of presumed local scattering and absorption properties can be constructed and compared against. The scattering and absorption parameters in the model are iteratively refined until the solution resembles the

measured data. Since this is an ill-posed inverse problem, the solutions are susceptible to noise and are often non-unique. Therefore, although the penetration depth of DOT can reach centimeters, the spatial resolution of DOT is rather modest, usually on the order of a fifth of the imaging depth. [10] However, the excellent imaging depth and inherent non-invasive nature of DOT makes it useful for many applications in tumor imaging and functional neuroimaging. [26-28]

Optical phase conjugation and wavefront shaping

In the past few years, various wavefront shaping methods have been proposed to overcome the problem of scattering in complex media such as biological tissues (reference [29] provides an excellent overview and discussion). The basic premise of these methods rests on the fact that scattering is a deterministic process. Thus, an appropriately shaped wavefront can traverse through the complex medium in a predictable way, for our purposes, to form an undistorted focus. The correct "shape" of a wavefront is specific to the particular medium and the particular arrangement of the scatterers within the medium through which light propagates. The methods to derive the correct shaped wavefront are numerous but can be grouped into two main categories—iterative shaping and direct measurements.

In the iterative methods, the wavefront is shaped with a spatial light modulator while monitoring the growth of light intensity at the location of the desired focus. [30-33] Wavefront shaping methods have been used for focusing through a wide variety of samples (e.g. paint, [33] living organisms [34]). In addition, these studies have provided important insights into the transport and control of light through disordered media. Alternatively, the time reversal symmetry of the sample can be used to derive the correct input wavefront via a method known as optical phase conjugation or time reversal (figure 1.1): Since scattering is deterministic and time reversible, the phase conjugate copy of a wavefront scrambled by a scattering medium can be propagated back through the same scattering medium to recover the input wavefront. [35] Optical phase conjugation has been shown to be able to reverse the effects of aberrations through non-biological samples like diffuser glass, and more recently

in biological tissues, in a method named turbidity suppression by optical phase conjugation (TSOPC). [36-39]

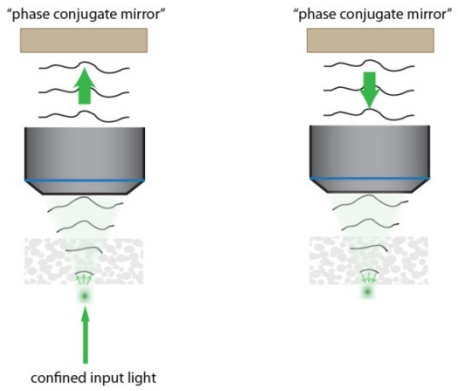

Fig. 1.1 | Optical phase conjugation. A focused input light scatters as it propagates through scattering medium. Making use of the time reversal symmetry (see chapter 2), the phase conjugate of the scattered wavefront can travel back through the scattering medium, undoing the effects of scattering as it re-converges at the location of the original focused input.

The wavefront shaping and optical phase conjugation methods introduced above measure only the transmission one of the many possible input modes, i.e. a small subset of the transmission properties of the medium under study. [29] In 1990, Isaac Freund proposed that any sample (even scattering objects) can be used as if it is a flawless optical element as long as its transmission properties are well characterized. [29,40] Indeed, it has been shown that with a more complete measurement of the transmission properties of a scattering medium (the transmission of many different input modes through the scattering medium), it is possible to both accurately unscramble and control the propagation of a wavefront through a scattering medium. [41-43]

The abovementioned methods present exciting opportunities for focusing and image transfer across scattering media. For biomedical applications, however, the important challenge is to focus inside. As a step towards this goal, an artificial "guide-star" is used (e.g. fluorescent sphere, [42] second harmonic particle, [43] gold nanoparticle [44]). The location of the focus is restricted to the location of the immobile guide-star, which has to be artificially inserted into the sample. Although the focus can be scanned around the target to which it is

optimized through the so-called "memory effect", [45] the scan range is determined by the range of the memory effect. This tends to be small in thick tissues. In addition, the condition of sparse distribution of the targets to be focused to has to be fulfilled. Thus, there is a need for a method that enables optical focusing at freely-defined locations within a scattering sample. The ability to do so will pave the way for many important biomedical applications in deep tissues such as optical imaging, spatially confined light delivery for optogenetics and photodynamic therapy.

1.3 DIGITAL TIME REVERSAL OF ULTRASOUND-ENCODED LIGHT AND VARIANCE-ENCODED LIGHT

Unlike light, ultrasound is insignificantly scattered in tissues. Therefore, an ultrasound focus can be defined within the tissue non-invasively using a focused ultrasound transducer. A small fraction of the scattered light that enters the ultrasound focus can be frequency-shifted via the acousto-optic effect. The ultrasound focus thus acts like a virtual source of frequency-shifted light. By measuring and time reversing the frequency-shifted light, an optical focus can be obtained at the vicinity of the ultrasound focus (figure 1.2). This novel concept was first demonstrated by Xu et al. [46] The team used a photorefractive crystal based phase conjugate mirror, which is limited in reflectivity. As a result, a low intensity focus was obtained and the team's demonstration was limited absorption contrast at submillimeter-scale resolution. Moreover, the analog recording device did not allow for further wavefront analysis and manipulation.

In this thesis, we present two methods—digital time reversal of ultrasound-encoded light (digital TRUE) [47] and time reversal of variance-encoded light (TROVE) [48]—that utilize the combination of ultrasound guide-stars with an optoelectronic phase conjugate mirror (digital optical phase conjugation, DOPC) to achieve focusing inside scattering media. There are two distinct advantages to the use of an optoelectronic phase conjugate mirror. First, the optoelectronic phase conjugate mirror provides much higher reflectivity compared to traditional analog phase conjugate mirrors. Second, by digitally measuring the ultrasound

frequency-shifted wavefront, we can analyze and manipulate the wavefront that is to be propagated back into the sample (in TROVE). With digital TRUE, we show high intensity focusing and fluorescence excitation in tissues and fluorescence imaging of complex fluorescent features and fluorescent-labeled tumors at tens of microns resolution, ~ 2.5 mm deep in *ex vivo* tissue.

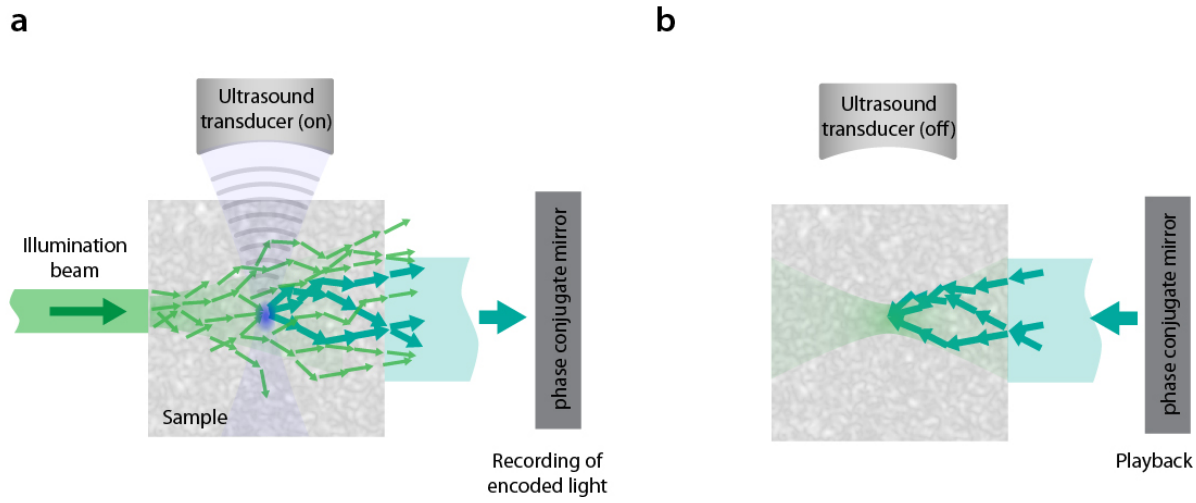

Fig. 1.2 | The concept of time reversal of ultrasound-encoded light (TRUE). [46] **a,** Part of the scattered light that passes through the ultrasound focus is frequency-shifted and impinges on the phase conjugate mirror along with non-shifted background. **b,** The phase conjugate mirror selectively phase conjugates the frequency-shifted light such that it focuses at the vicinity of the ultrasound.

The resolution of TRUE techniques is fundamentally limited by the size of the ultrasound focus, which is on the order of the acoustic wavelength (~tens of micrometers). This essentially means that the virtual source of frequency-shifted light contains many speckles, and their contributions to the output wavefront we measure contains a mixture of optical fields originating from each of these speckles (figure 1.3). In TROVE, we demix the contributions of the optical spatial modes using an ultrasound envelope imposed variance-encoding of individual spatial modes. By analysing the frequency-shifted wavefronts that result from a mix of the variance-encoded spatial modes, we computationally derive the wavefront that uniquely corresponds to one spatial mode. Phase-conjugating this wavefront, we obtain an optical speckle sized phase conjugate focus. Thus, with TROVE, we uncouple

the system resolution from that of the ultrasound focus, demonstrating optical focusing and imaging in the diffusive regime at unprecedented lateral resolution of ~5 μm.

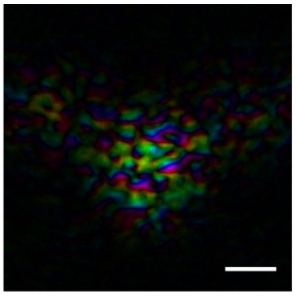

Fig. 1.3 | Speckles within ultrasound focus. A complex image of speckles within an ultrasound focus; in this case, as a result of passing through a diffusing tape. Hue represents phase and saturation represents amplitude. These speckles after propagating through another layer of scattering medium, each contribute to the complex map measured. In TROVE, we use a computational algorithm to demix the contribution of the speckles to find a phase conjugate field that focuses onto one speckle. Scale bar: 25 μm. [48]

Although only fluorescence excitation and imaging are demonstrated, digital TRUE and TROVE are capable of providing a wide range of optical contrasts with ultrasound resolution and depth and can potentially find use in optical manipulation techniques like optogenetics and optical tweezing and trapping.

1.4 OUTLINE OF THESIS

The appendix that accompanies this chapter contains brief explanations of some concepts that underlie the work presented in this thesis. In chapter 2, we will provide some background on the theory and practical implementations of optical phase conjugation. This also serves as a motivation to and a comparison for chapter 3, where we will introduce the principles of the digital optical phase conjugation (DOPC) technique that is used in digital time reversal of ultrasound-encoded light (digital TRUE) and time reversal of variance-encoded light (TROVE). We will highlight the improvements made to the DOPC since its first conception by Cui and Yang. [49] In addition, we will discuss the effect of partial phase conjugation and sample motion on phase conjugation fidelity. In chapters 4 and 5, we will report on the demonstrations of digital TRUE and TROVE. These chapters are largely

reproduced from published (or, soon to be published) work on digital TRUE [47] and TROVE [48] respectively. Finally, in chapter 6, we will discuss improvements that can be made to the systems and possible future applications.

APPENDIX: SOME IMPORTANT CONCEPTS

Speckles — Origins and statistics

As light impinges onto a scatterer, it gives rise to a scattered wavefront that can be thought of as consisting of wavelets each with its unique phase and amplitude. [31] Each of these wavelets impinges other scatterers and produces more wavelets. Thus, as light propagates through a scattering medium more and more of these wavelets form. Because of the complex nature of the interaction of light with highly disordered medium, the wavelets emerging from the scattering medium have traveled through randomized paths due to the wavefront's interactions with scatterers. If the light source is coherent, these wavelets (with randomized phase and amplitudes) meeting at each spatial location can interfere to form a stable speckle pattern. [50] Figure 1.4 shows a speckle intensity map, with the bright spots being the result of localized constructive interference and the dark spots resulting from localized destructive interference.

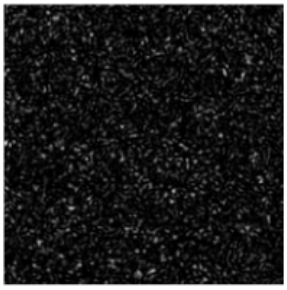

Fig. 1.4 | A speckle intensity pattern projected onto a CCD sensor with an objective lens.

Several useful statistical properties of a perfectly polarized, fully developed speckle field have been derived with the assumptions that (1) the phases of the contributing wavelets at each spatial location are uniformly distributed, and (2) the amplitude and phase

of each wavelet is independent. [50,51,31] With these assumptions, the addition of these wavelets (phasors) at each spatial location of the scattered field is analogous to the classical problem of random walk in a plane. [50,51,31] It can be found that the resultant real and imaginary components of the complex scattered field are uncorrelated and have zero means and same variances. Without going into the details of derivations that can be found in references, if the number of phasors contributing to the speckle is very large, the central limit theorem can be used to derive that the joint probability density function of the real and imaginary components of the speckle field ($\mathrm{Re}(E)$ and $\mathrm{Im}(E)$ respectively): [50,51,31]

$$p\big(\mathrm{Re}(E), \mathrm{Im}(E)\big) = \frac{1}{\pi\langle I\rangle}\exp\left(-\frac{|\mathrm{Re}(E)|^2 + |\mathrm{Im}(E)|^2}{\langle I\rangle}\right) \tag{1.13}$$

In other words, the real and imaginary components are independent circular Gaussian distributed random variables with zero mean, where $\langle I\rangle$ is the ensemble average of the intensity of the speckles.

The intensity of the speckles I follows a negative exponential distribution: [50,51,31]

$$p(I) = \frac{1}{\langle I\rangle}\exp\left(-\frac{I}{\langle I\rangle}\right) \tag{1.14}$$

This means that the probability of the occurrence of a speckle decreases exponentially with its intensity. In other words, a speckle has the greatest probability of having zero intensity.

Transmission matrix representation

A transmission matrix $\boldsymbol{T}$ can be used to describe how the phase and amplitude of an input field is modified by the medium it is propagating through. [29,31] An N by M transmission matrix maps N independent input modes to M independent output modes. For simplicity, we restrict our discussion here and in the rest of the thesis to the mapping of spatial modes. If the medium is optically clear, the transmission matrix is the identity matrix, perfectly transmitting the input field to the output. The representation of the transmission of light through a random scattering medium is more complicated. When the complete transmission can be quantified and there is no loss in the system, the medium is sometimes

modeled by a random unitary matrix, [31] such that $\boldsymbol{TT^{\dagger} = I}$. This describes the time reversal symmetry further discussed in chapter 2. A good summary and explanation of the random matrix theory and the interesting transmission properties it predicts are given in chapter 8 of reference [31].

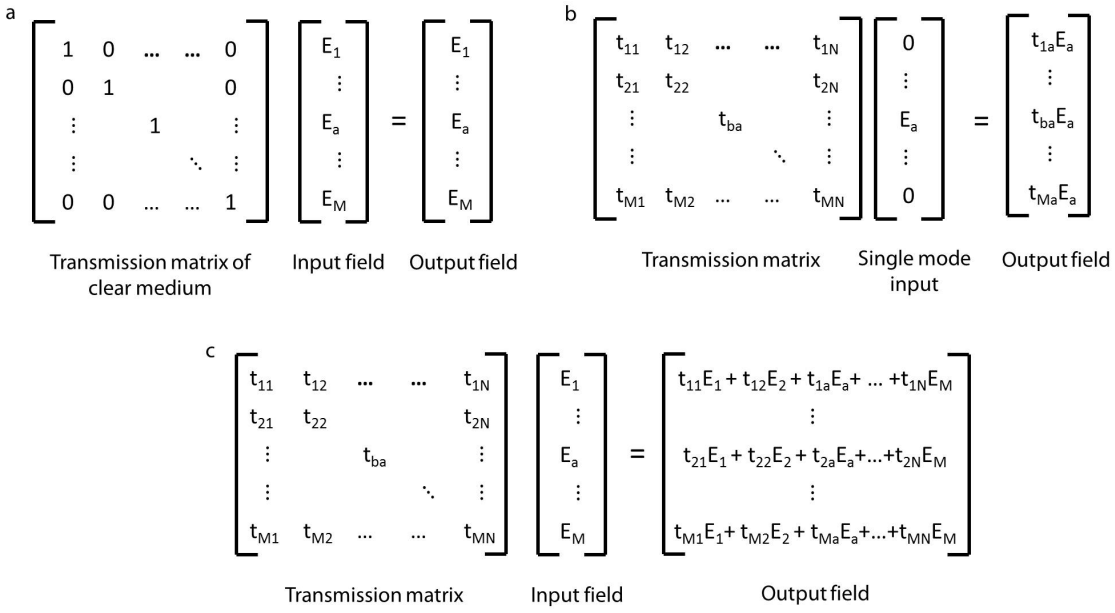

Fig. 1.5 | Transmission matrix representation of light propagation. a, When the medium is completely clear, the transmission matrix is diagonal, transmitting the input field faithfully. **b,** A random scatterer where only a small subset of the transmission is measured, the matrix elements are represented by t_{ba} independently drawn from a circular Gaussian distribution [28]. The subscripts *a* and *b* refer to the input and output channels respectively and also corresponds to the matrix element at row b, column a. With a single mode input, the output field is directly corresponds to a column of the transmission matrix. **c,** When there are more than one inputs, the output field is a linear superposition of the wavefronts that would result from the individual input modes.

However, in most cases, we only experimentally measure (and manipulate) a small subset of the complete transmission. In this case, the transmission matrix is modeled with matrix elements t_{ba} whose real and imaginary components are independently drawn from a circular Gaussian distribution. [31,51] Here, the subscripts *a* and *b* refer to the input and output channels respectively and t_{ba} corresponds to the matrix element at row b, column a. When there is only one input mode, the resultant speckle field (output modes) corresponds essentially to a column in the transmission matrix, giving rise to the familiar speckle

statistics discussed in the section above (figure 1.5b). With several input modes, the output field is the linear sum of the fields that would result from each individual input mode (figure 1.5c). Both wavefront shaping and optical phase conjugation utilize this deterministic additive relationship between input and output modes to spatially focus light through scattering medium (see chapter 3.2).

Frequency shifting due to acousto-optic effect

In this thesis, we utilize the acousto-optic phenomenon to frequency-shift light that has passed through the ultrasound focus.

Particle description

The easiest way to understand this frequency shifting is to make use of the particle-wave duality, which can be applied to both light and sound. [52,53] Light waves of frequency f_L and sound waves of frequency f_{us} can be thought of as streams of photons and phonons with energy hf_L and hf_{us} respectively, where h is the Planck constant. A phonon is a massless particle that represents mechanical vibrations in the medium it travels through. When a photon collides with a phonon, there is a probability of it absorbing the phonon (in what is called an anti-Stokes Brillouin process) or losing energy in a form of a phonon (Stokes Brillouin process). As a result of energy conservation, the resultant frequency of the photon becomes $f = f_L \pm f_{us}$.

Wave description

In the wave picture, the frequency-shifting of light by ultrasound can be related to two mechanisms. The first is based on the photoelastic effect, where the refractive index of the medium is modulated by mechanical rarefaction and compression caused by the acoustic waves. The refractive index change that results is related to the power of the acoustic waves by: [53-56]

$$\Delta n = \sqrt{\frac{n^6 p^2 P_a}{2\rho v^3 A}} \tag{1.15}$$

where n is the refractive index of the medium, p is the element of the photoelastic tensor corresponding to the direction of mechanical strain (for the purpose of our discussions, we assume an isotropic medium), P_a is the acoustic power, ρ is the mass density, v is the sound velocity, and A is the cross-sectional area of the ultrasound beam perpendicular to the direction of propagation. As a result, a phase grating traveling at the speed of sound is set up. The amount of frequency-shifted light is proportional to the strength of the phase grating (Δn). The second mechanism is the periodic displacement of scattering particles due to the acoustic waves. Both mechanisms result in optical path length (thus, phase) variations over time at the acoustic frequency akin to Doppler effect, resulting in a frequency-shift equal to the frequency of the acoustic wave. We note that the former is dominant in the regime where the scattering mean free path is on the order of (or larger) than the acoustic wavelength, which is the case in our experiments where both scattering mean free path and acoustic wavelength are ~30 microns. [56,57]

REFERENCES

1 Rust, M.J., Bates, M. & Zhuang, X. Sub-diffraction-limit imaging by stochastic optical reconstruction microscopy (STORM). *Nature Methods* **3**, 793-795, (2006).

2 Betzig, E. *et al.* Imaging Intracellular Fluorescent Proteins at Nanometer Resolution. *Science* **313**, 1642-1645, (2006).

3 Westphal, V. *et al.* Video-rate far-field optical nanoscopy dissects synaptic vesicle movement. *Science* **320**, 246-249, (2008).

4 Zhang, F., Wang, L.-P., Boyden, E.S. & Deisseroth, K. Channelrhodopsin-2 and optical control of excitable cells. *Nature Methods* **3**, 785-792, (2006).

5 Zhang, F. *et al.* Multimodal fast optical interrogation of neural circuitry. *Nature* **446**, 633-U634, (2007).

6 Svoboda, K. & Block, S.M. Biological Applications of Optical Forces. *Annual Review of Biophysics and Biomolecular Structure* **23**, 247-285, (1994).

7 Moffitt, J.R., Chemla, Y.R., Smith, S.B. & Bustamante, C. Recent Advances in Optical Tweezers. *Annual Review of Biochemistry* **77**, 205-228, (2008).

8 Cheong, W.F., Prahl, S.A. & Welch, A.J. A review of the optical properties of biological tissues. *Quantum Electronics, IEEE Journal of* **26**, 2166-2185, (1990).

9 Steiner, R. in *Laser and IPL Technology in Dermatology and Aesthetic Medicine* (eds C. Raulin & S. Karsai) (Springer-Verlag Berlin Heidelberg, 2011).

10 Wang, L.V. & Wu, H.-I. *Biomedical Optics: Principles and Imaging*. (Wiley, 2007).

11 Cheng, P.-C. in *Handbook Of Biological Confocal Microscopy* (ed James B. Pawley) Ch. 8, 162-206 (Springer US, 2006).

12 Van de Hulst, H. *Light scattering by small particles*. (Dover Publications, 1981).

13 Prahl, S.A. *Mie Scattering Calculator*, <http://omlc.ogi.edu/calc/mie_calc.html>

14 Tuchin, V. *Tissue optics: light scattering methods and instruments for medical diagnosis*. (SPIE Press 2007).

15 McDowell, E.J. *Low optical signal detection in biological materials: SNR considerations and novel techniques* Ph.D. thesis, California Institute of Technology, (2010).

16 Demos, S.G. & Alfano, R.R. Temporal gating in highly scattering media by the degree of optical polarization. *Optics Letters* **21**, 161-163, (1996).

17 Inoue, S. in *Handbook Of Biological Confocal Microscopy* (ed James B. Pawley) Ch. 1, 1-16 (Springer US, 2006).

18 Ntziachristos, V. Going deeper than microscopy: the optical imaging frontier in biology. *Nat Meth* **7**, 603-614, (2010).

19 Denk, W., Strickler, J.H. & Webb, W.W. Two-photon laser scanning fluorescence microscopy. *Science* **248**, 73-76, (1990).

20 Horton, N.G. *et al.* In vivo three-photon microscopy of subcortical structures within an intact mouse brain. *Nat Photon* **7**, 205-209, (2013).

21 Huang, D. *et al.* Optical coherence tomogrpahy. *Science* **254**, 1178-1181, (1991).

22 Zhu, D., Larin, K.V., Luo, Q. & Tuchin, V.V. Recent progress in tissue optical clearing. *Laser & Photonics Reviews*, n/a-n/a, (2013).

23 Hama, H. *et al.* Scale: a chemical approach for fluorescence imaging and reconstruction of transparent mouse brain. *Nat Neurosci* **14**, 1481-1488, (2011).

24 Sharpe, J. *et al.* Optical Projection Tomography as a Tool for 3D Microscopy and Gene Expression Studies. *Science* **296**, 541-545, (2002).

25 Oldham, M. *et al.* Three-dimensional imaging of whole rodent organs using optical computed and emission tomography. *Journal of Biomedical Optics* **12**, 014009-014009, (2007).

26 Boas, D.A. *et al.* Imaging the body with diffuse optical tomography. *Signal Processing Magazine, IEEE* **18**, 57-75, (2001).

27 Tromberg, B.J. *et al.* Assessing the future of diffuse optical imaging technologies for breast cancer management. *Medical Physics* **35**, 2443-2451, (2008).

28 Boas, D.A., Dale, A.M. & Franceschini, M.A. Diffuse optical imaging of brain activation: approaches to optimizing image sensitivity, resolution, and accuracy. *Neuroimage* **23**, S275-S288, (2004).

29 Mosk, A.P., Lagendijk, A., Lerosey, G. & Fink, M. Controlling waves in space and time for imaging and focusing in complex media. *Nature Photonics* **6**, 283-292, (2012).

30 Vellekoop, I.M. & Mosk, A.P. Focusing coherent light through opaque strongly scattering media. *Opt. Lett.* **32**, 2309-2311, (2007).

31 Vellekoop, I.M. *Controlling the propagationg of light in disordered scattering media* PhD thesis, University of Twente, (2009).

32 Vellekoop, I.M. & Mosk, A.P. Universal Optimal Transmission of Light Through Disordered Materials. *Physical Review Letters* **101**, 120601, (2008).

33 Vellekoop, I.M., LagendijkA & Mosk, A.P. Exploiting disorder for perfect focusing. *Nat Photon* **4**, 320-322, (2010).

34 Vellekoop, I.M. & Aegerter, C.M. Focusing light through living tissue. *Proc. of SPIE* **7554**, 755430-755430, (2010).

35 Yariv, A. Phase conjugate optics and real-time holography. *Quantum Electronics, IEEE Journal of* **14**, 650-660, (1978).

36 Leith, E.N. & Upatnieks, J. Holographic Imagery Through Diffusing Media. *J. Opt. Soc. Am.* **56**, 523-523, (1966).

37 Yaqoob, Z., Psaltis, D., Feld, M.S. & Yang, C. Optical phase conjugation for turbidity suppression in biological samples. *Nat Photon* **2**, 110-115, (2008).

38 McDowell, E.J. *et al.* Turbidity suppression from the ballistic to the diffusive regime in biological tissues using optical phase conjugation. *Journal of Biomedical Optics* **15**, 025004-025004, (2010).

39 Cui, M., McDowell, E.J. & Yang, C. An in vivo study of turbidity suppression by optical phase conjugation (TSOPC) on rabbit ear. *Opt. Express* **18**, 25-30, (2010).

40 Freund, I. Looking through walls and around corners. *Physica A: Statistical Mechanics and its Applications* **168**, 49-65, (1990).

41 Popoff, S., Lerosey, G., Fink, M., Boccara, A.C. & Gigan, S. Image transmission through an opaque material. *Nat Commun* **1**, 81, (2010).

42 Vellekoop, I.M., Cui, M. & Yang, C. Digital optical phase conjugation of fluorescence in turbid tissue. *Applied Physics Letters* **101**, (2012).

43 Hsieh, C.-L., Pu, Y., Grange, R. & Psaltis, D. Digital phase conjugation of second harmonic radiation emitted by nanoparticles in turbid media. *Opt. Express* **18**, 12283-12290, (2010).

44 Popoff, S.M. *et al.* Exploiting the Time-Reversal Operator for Adaptive Optics, Selective Focusing, and Scattering Pattern Analysis. *Physical Review Letters* **107**, 263901, (2011).

45 Freund, I., Rosenbluh, M. & Feng, S. Memory Effects in Propagation of Optical Waves through Disordered Media. *Physical Review Letters* **61**, 2328-2331, (1988).

46 Xu, X., Liu, H. & Wang, L.V. Time-reversed ultrasonically encoded optical focusing into scattering media. *Nat Photon* **5**, 154-157, (2011).

47 Wang, Y.M., Judkewitz, B., DiMarzio, C.A. & Yang, C. Deep-tissue focal fluorescence imaging with digitally time-reversed ultrasound-encoded light. *Nat Commun* **3**, 928, (2012).

48 Judkewitz, B., Wang, Y.M., Horstmeyer, R., Mathy, A. & Yang, C. Speckle-scale focusing in the diffusive regime with time-reversal of variance-encoded light (TROVE). *Nature Photonics* 7, 300-305, (2013).

49 Cui, M. & Yang, C. Implementation of a digital optical phase conjugation system and its application to study the robustness of turbidity suppression by phase conjugation. *Opt. Express* **18**, 3444-3455, (2010).

50 Goodman, J.W. Some fundamental properties of speckle. *J. Opt. Soc. Am.* **66**, 1145-1150, (1976).

51 Dainty, J.C. *et al. Laser Speckle and Related Phenomena*. Vol. 9 (Springer-Verlag 1975).

52 Band, Y.B. *Light and Matter: Electromagnetism, Optics, Spectroscopy and Lasers*. (Wiley, 2006).

53 Yariv, A. & Yeh, P. *Photonics: Optical Electronics in Modern Communications* 6edn, (Oxford University Press, 2006).

54 Elson, D.S., Li, R., Dunsby, C., Eckersley, R. & Tang, M.-X. Ultrasound-mediated optical tomography: a review of current methods. *Interface Focus* **1**, 632-648, (2011).

55 Whitaker, J.C. *The Electronics Handbook*. 2nd edn, (CRC Press, 2005).

56 Resink, S.G., Boccara, A.C. & Steenbergen, W. State-of-the art of acousto-optic sensing and imaging of turbid media. *Journal of Biomedical Optics* **17**, 040901-040901, (2012).

57 Wang, L.V. Mechanisms of ultrasonic modulation of multiply scattered coherent light: a Monte Carlo model. *Opt. Lett.* **26**, 1191-1193, (2001).

Chapter 2
Introduction to Optical Phase Conjugation

Here, we will introduce the properties of the phase conjugate field both intuitively and mathematically. We will also briefly describe the conventional means of achieving optical phase conjugation and discuss their merits and limitations. We note that the concepts discussed serve as an introduction to DOPC, a specific means to achieve phase conjugation, which will be discussed in the later chapters.

2.1 PRINCIPLES OF OPTICAL PHASE CONJUGATION

Wave equation description

Before delving into the discussions of the application of optical phase conjugation in reversing scattering, we will first describe the basic properties of the phase conjugate mirror and the complex conjugate optical field it produces. To explain the properties of a phase conjugate mirror, a comparison with a conventional mirror may be beneficial. The conventional mirror reflects light by inverting the wavevector perpendicular to the direction of propagation, fitting the common intuition that the angle of incidence is equal to the angle of reflection (figure 2.1a). The phase conjugate mirror reverses (complex conjugates) all the components of the wavevector, resulting in the conceptual observation that the light field travels backwards through its original path (figure 2.1b). [1,2]

To put optical phase conjugation in the context of distortion correction, we summarize the work of Yariv, a pioneer in optical phase conjugation, detailed in reference [1]: An optical field propagating from left to right in the z direction is represented as

$$E = \psi(\vec{r})\exp\left[i(\omega t - k_z z)\right] = A(\vec{r})\exp\left(i\omega t\right) \tag{2.1}$$

where $\psi(\vec{r})$ is the complex amplitude of the field and represents the spatial information or distortions it carries. At the phase conjugate mirror, the reflected phase conjugate field is

$$E_{OPC} = \psi^*(\vec{r})\exp\left[i(\omega t + k_z z)\right] = A_{OPC}(\vec{r})\exp\left(i\omega t\right) \tag{2.2}$$

which is a field travelling in the opposite direction, with $A_{OPC}(\vec{r}) = A^*(\vec{r})$. We observe that the spatial components of equation (2.2) are simply the complex conjugate of the spatial components to obtain equation (2.1); the temporal component (exp $(i\omega t)$) is unchanged. This is the same as not changing the spatial components but reversing the temporal component (propagating the wave back in time), which is why sometimes phase conjugation is sometimes referred to as "time reversal". [1] (Note: In the chapters that follow, we sometimes entirely leave out the temporal component, instead representing the electric field as its complex amplitude only. In this representation, $E = A\exp(i\theta)$, where A is the real and positive amplitude of the field and θ is its phase.)

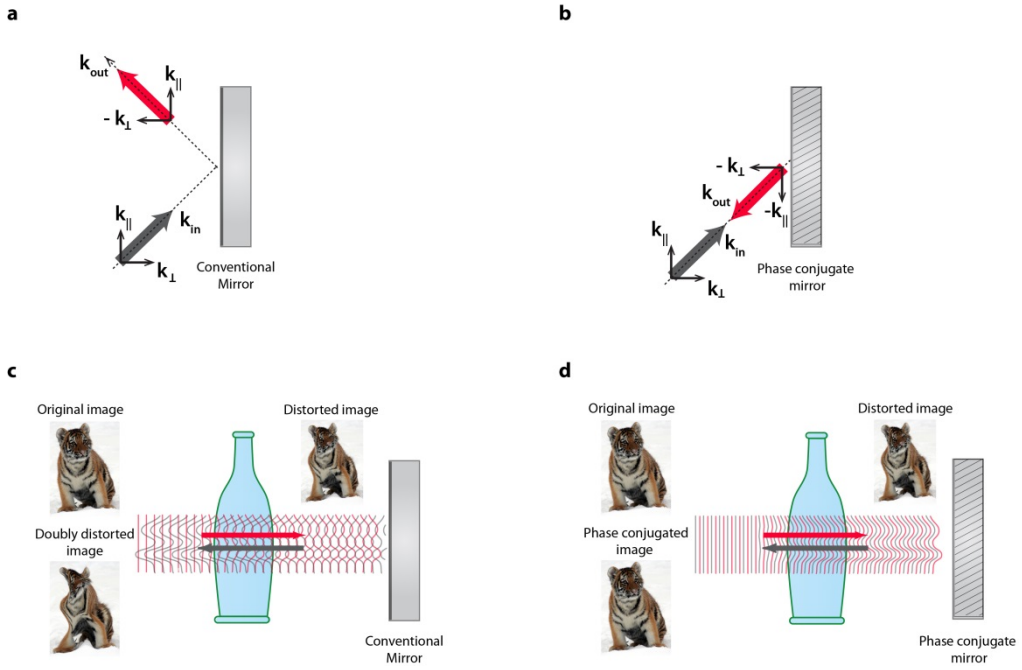

Fig. 2.1 | Comparison between a phase conjugate mirror and a conventional mirror. **a-b,** Two-dimensional representations of wavevectors reflecting off a conventional mirror and a phase conjugate mirror, respectively. Redrawn based on figure 1 of reference [2]. **a,** A conventional mirror reflects light by only reversing the component of the k vector that is normal to its surface. **b,** A phase conjugate mirror reverses all the components of the k vector, essentially changing its sign. Thus, the phase conjugate mirror can be thought of as a device that sends light back to its source, regardless of its tilt. **c,** When a conventional mirror reflects a distorted wavefront, the complex amplitude is not changed. **d,** In contrast, reflection off the phase conjugate mirror yields a reflected wavefront whose amplitude is the complex conjugate of that of the incident wavefront. **c** and **d** are modified from reference [1].

The mathematical description above also suggests that any spatial information, or any distortion, is reversed in the phase conjugate wavefront E_{OPC}. To verify the "self-healing" properties of the phase conjugate wavefront mathematically, the wave equation for the propagation of the wavefront E through a distorting medium with spatially varying refractive index $n(\vec{r})$ (recalling that scattering is caused by refractive index mismatches in a medium) can be described as [1]

$$\nabla^2 E + \frac{\omega^2}{c^2} n(\vec{r})^2 E = 0 \tag{2.3}$$

From which, we can obtain

$$\nabla^2 \psi + \left[\frac{\omega^2}{c^2} n(\vec{r})^2 - {k_z}^2\right]\psi - 2ik_z \frac{\partial \psi}{\partial z} = 0 \tag{2.4}$$

We observe that the phase conjugate of equation (2.4) gives:

$$\nabla^2 \psi^* + \left[\frac{\omega^2}{c^2} n(\vec{r})^2 - {k_z}^2\right]\psi^* + 2ik_z \frac{\partial \psi^*}{\partial z} = 0 \tag{2.5}$$

We can see that equation (2.5) is the wave equation describing the propagation of E_{OPC}, which is a wave travelling in the opposite direction to E, having the exactly the complex conjugate of the amplitude of E at each point in space. Meaning, in addition to reversing the propagation direction, the reflection off the phase conjugation mirror is identical to (except a phase conjugate of) the incident wavefront. Thus, after the phase conjugate beam passes back through the distorting medium, we should recover the undistorted wavefront (figure 2.1d).

Scattering matrix and transmission matrix descriptions

It is also possible to describe the propagation of monochromatic light through a distorting medium with a scattering matrix. If the sample has a semi-infinite slab geometry, we only have to consider the transmission and reflection on the two sides, A and B, of the sample, obtaining

$$\begin{bmatrix} \boldsymbol{E_{out}^{AB}} \\ \boldsymbol{E_{out}^{BA}} \end{bmatrix} = \begin{bmatrix} \boldsymbol{T^{AB}} & \boldsymbol{R^{BA}} \\ \boldsymbol{R^{AB}} & \boldsymbol{T^{BA}} \end{bmatrix} \begin{bmatrix} \boldsymbol{E_{in}^{AB}} \\ \boldsymbol{E_{in}^{BA}} \end{bmatrix} \tag{2.6}$$

where the T and R represents transmission and reflection respectively, and the superscripts refer to the directions of propagation (AB being from side A to side B; BA being from side B to side A). [4,5]

Often, in our experiments and also in our descriptions of OPC, we consider only the transmission. In these cases, the input wavefront is described by a vector $\boldsymbol{E_A}$, where each element represents an independent spatial mode. Likewise, the output wavefront is represented by a vector $\boldsymbol{E_B}$, where each element represents an independent spatial mode. The medium that $\boldsymbol{E_A}$ passes through, is represented by $\boldsymbol{T_{AB}}$ which maps the input modes on side A to the output modes on side B. Thus, we obtain the relation

$$\boldsymbol{E_B} = \boldsymbol{T_{AB}}\boldsymbol{E_A} \tag{2.7}$$

In the case of ideal phase conjugation, where the entire distorted wavefront is intercepted and phase conjugated, the phase conjugated playback field is

$$\boldsymbol{E_{OPC}} = (\boldsymbol{T_{AB}}\boldsymbol{E_A})^* \tag{2.8}$$

Assuming that elastic scattering is a lossless, deterministic and thus time-symmetric process, the phase-conjugated field back at input plane $\boldsymbol{E'_{in}}$ is described by

$$\boldsymbol{E'_A} = \boldsymbol{T_{BA}}(\boldsymbol{T_{AB}}\boldsymbol{E_A})^* = \boldsymbol{T_{AB}^{\dagger}}\boldsymbol{T_{AB}^{*}}\boldsymbol{E_A^{*}} = \boldsymbol{I}\boldsymbol{E_A^{*}} \tag{2.9}$$

where $\boldsymbol{T_{BA}}$ that maps the field on the output side back to the input side. [4,5] Here, * denotes complex conjugate and † denotes the complex transpose of a matrix. We find that because of the time-symmetry, we recover the field at the input plane.

2.2 DEVIATIONS FROM THE IDEAL

So far, we have described phase conjugation in a lossless, deterministic and time-symmetric framework. However, this framework contains assumptions which do not hold in reality. One key assumption here is that $\boldsymbol{T}\boldsymbol{T}^{\dagger} = \boldsymbol{I}$, or $\boldsymbol{T}^{\dagger} = \boldsymbol{T}^{-1}$ (i.e $\boldsymbol{T}$ is a unitary matrix).

However, this is only true if the entire field is phase conjugated – phase and amplitude, transmitted and reflected, propagating and evanescent (i.e. there is no loss). In reality, this is not a valid assumption even in transparent samples, considering the existence of non-propagating modes; and especially so in highly scatterings media where, in addition to evanescent loss, scattered light spread over a large solid angle. Mathematically, this means that $\boldsymbol{T}$ is no longer well approximated by a unitary matrix. As a result, although $\boldsymbol{TT}^{\dagger}$ has a strong diagonal, it also has non-zero off-diagonal values. This has some important consequences related to our work. First, the phase conjugation fidelity decreases with increasing complexity of the field. [6,7] Second, the phase conjugation fidelity decreases with the size of $\boldsymbol{T}$ recorded and phase conjugated. [8]

The other key assumption is that the scattering properties of dynamic samples (e.g. biological tissues) can be adequately described by static transmission matrices, which is practically only valid over a certain time frame. The practical consequence of the limited stability of samples is that the phase conjugation fidelity will degrade with time. The characteristic time constant of the degradation in a particular medium is closely related to how fast the transmission matrix, which describes the medium, changes. The consequences of these two deviations from ideal phase conjugation will be further dissected in the next chapter, in the context of the digital optical phase conjugation system.

2.3 CONVENTIONAL PHASE CONJUGATE MIRRORS

Up to this point, we have discussed the properties of the phase conjugate wavefront rather extensively. However, we have yet to describe how to produce such a wavefront. A phase conjugate mirror is a general term for any device that produces phase conjugate wavefronts. Until recently, phase conjugate wavefronts have been achieved most commonly through static holography, four-wave mixing and stimulated Brillouin scattering. [1] Of these strategies, static holography is the closest analog to digital optical phase conjugation (DOPC), a technique that is key to the methods presented in this thesis. Thus, a more detailed description would benefit later discussions on the DOPC. The other two methods—

Four-wave mixing and stimulated Brillouin scattering—will be briefly described. We will also discuss the merits and limits of each of these methods, motivating the choice of using DOPC for the work described in this thesis.

Static holography

Of all the three common methods to generate an OPC beam, static holography is probably the easiest to approach and is the most analogous to DOPC. In this method, a hologram (containing phase and amplitude information) of the scattered wavefront is written into a holographic material and its phase conjugate read out at a later time figure 2.2.

In the recording step, the scattered wavefront interferes with a reference beam inside the photorefractive crystal (figure 2.1a). We represent the scattered field by

$$E_{sc}(x,y) = |E_{sc}(x,y)|\exp\,[j\varphi(x,y)] \tag{2.10}$$

and the reference field by

$$E_{ref}(x,y) = \left|E_{ref}(x,y)\right|\exp\,[j\omega(x,y)] \tag{2.11}$$

The intensity of the interference pattern inside the photorefractive crystal is thus

$$I(x,y) = |E_{sc}(x,y)|^2 + \left|E_{ref}(x,y)\right|^2 + 2|E_{sc}(x,y)|\left|E_{ref}(x,y)\right|\cos[\omega(x,y) - \varphi(x,y)] \tag{2.12}$$

Given that the reference field is known (and we assume for simplicity that it has uniform amplitude and phase over the interference zone), we can see that this process couples the complex (phase and amplitude) information of the scattered wavefront to the intensity in the interference pattern. [9]

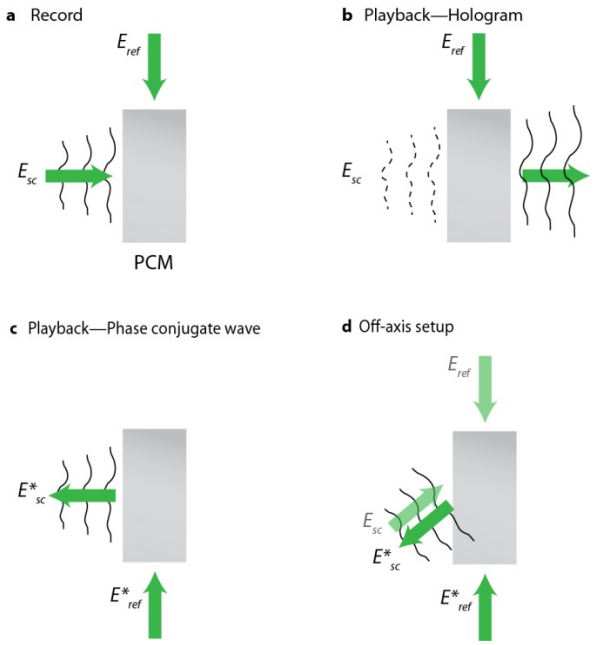

Fig. 2.2 | Static holography. a, In the recording step, the scattered beam E_{sc} interferes with a flat reference beam E_{ref} inside a holographic recoding medium, which serves as the phase conjugate mirror. The interference pattern that results causes local changes in refractive index that are proportionate to incident light intensity. **b,** If we shine an identical reference beam onto the grating that was written, we essentially play back a hologram of the scattered wavefront. **c,** However, if we play back using a phase conjugate of the reference beam E^*_{ref}, we obtain the phase conjugate of the scattered wavefront E^*_{sc}. **d,** As mentioned in the text, undesired fields are obtained in addition to E^*_{sc}. Using an off-axis setup, the fields can be angularly resolved.

This intensity grating in the photorefractive crystal results in migration of positive charges away from the areas of high light intensity. This results in localized electric fields that in turn cause refractive index changes through the linear electro-optic effect (Pockels effect). [9] Assuming that the recording is linear, the transmittance of the photorefractive crystal becomes

$$t_{sc}(x,y) = t_b + \beta'(|E_{sc}|^2 + E^*_{sc}E_{ref} + E^*_{ref}E_{sc}) \tag{2.13}$$

t_b is a DC bias that can be assumed to be spatially uniform due to the assumption of the flat reference beam, whereas β' is the slope of the characteristic transmittance vs exposure curve of the photorefractive crystal at the exposure time used. [9,10]

In the playback step (figure 2.2b), the coherent reconstruction field E_{recon} impinges onto the photorefractive crystal, obtaining

$$E_{recon}t_{sc}(x,y) = t_b E_{recon} + \beta'|E_{sc}|^2 E_{recon} + \beta' E_{sc}^* E_{ref} E_{recon} + \beta' E_{ref}^* E_{sc} E_{recon} \quad (2.14)$$

If $E_{recon} = E_{ref}^*$, the third term in equation 2.14 becomes

$$\beta' E_{ref}^* E_{sc} E_{recon} = \beta' \left|E_{ref}\right|^2 E_{sc}^* \quad (2.15)$$

Thus, we obtain a phase conjugate of the recorded scattered field E_{sc}^* that propagates back through the scattering medium (figure 2.2c). [1,9] We note that, in each case, the field of interest is accompanied by three additional field components that may be angularly separated using off-axis holography (figure 2.2d). [11]

We observe that (1) the amplitude (and thus intensity) of the playback field is always proportional to the amplitudes of the input fields, and (2) the uniform light field incident on the crystal during playback causes the electric charges in the photorefractive crystal to spread out. This essentially describes the self-erasing process during playback. Taken together, these properties limit the total energy in the phase conjugate field. Without fixing the holograms written (e.g. by heat treatment), the reflectivity of the phase conjugate mirror is usually less than unity. [12]

Degenerate four-wave mixing

In degenerate four-wave mixing (DFWM), we can think about the reading and writing steps described above as taking place simultaneously (figure 2.3). [1,2] The DFWM medium can be any material that exhibits significant third order nonlinear optical susceptibility. The scattered wavefront E_{sc}, the reference plane wave E_{ref} and the "read-out" counter-propagating plane wave E_{read} (equivalent to E_{ref}^*) interact simultaneously in this nonlinear crystal such that : (1) E_{sc} interferes with E_{ref}. [1,2] At high enough optical intensities, the polarization of the crystal becomes nonlinear with the impinging electric field setting up a refractive index grating, and (2) E_{read} instantly scatters off the grating to produce another

field E_{result}. This field is necessarily E_{sc}^{*} because the phase matching condition requires that their frequencies and wave vectors are related as $\omega_{result} = \omega_{ref} + \omega_{read} - \omega_{sc}$ and $k_{result} = k_{ref} + k_{read} - k_{sc}$ respectively. Furthermore, it can be proven that the electric field amplitude of the resultant beam is

$$E_{result} = \frac{i\omega l}{2nc} X^{(3)} E_{ref} E_{read} E_{sc}^{*} \tag{2.16}$$

where c is the speed of light, n is the refractive index of the medium and l is the beam interaction length. Thus, if $E_{read} = E_{ref}^{*}$, $E_{result} \propto E_{sc}^{*}$. [13]

We can make a few observations here. First, we note that the roles of E_{ref} and E_{read}, most commonly referred to as the pump beams, can be interchanged. Second, it is theoretically possible that the phase conjugate beam is more intense than E_{sc}. Experimentally, Feinberg and Hellwarth demonstrated a phase conjugate mirror based on DFWM mixing in Barium Titanate crystal with a gain of ~ 100. [14]

Stimulated Brillouin scattering

Stimulated Brillouin scattering (SBS) occurs when an intense laser beam E_{in} (pump beam) itself produces acoustic vibrations through electrostriction, a phenomenon where the medium becomes denser in areas of high laser intensity. This pump beam loses energy to the vibrating medium and scatters back (Stokes beam) in the opposite direction with a lower frequency (figure 2.4). [1,2,15,16] This backscattered light E_{out} can interact coherently with the incoming beam E_{in} to produce more sound waves. It turns out that this process is the most efficient and self-reinforcing when E_{out} is exactly the phase conjugate of E_{in}. Thus, producing the phase conjugate wavefront and suppressing other possible wavefronts.

Like DFWM, SBS is capable of producing phase conjugate wavefronts in real time. Due to energy conservation, SBS cannot achieve a phase conjugate beam higher in energy than the pump beam. However, the SBS reflectivity can approach unity. [17]

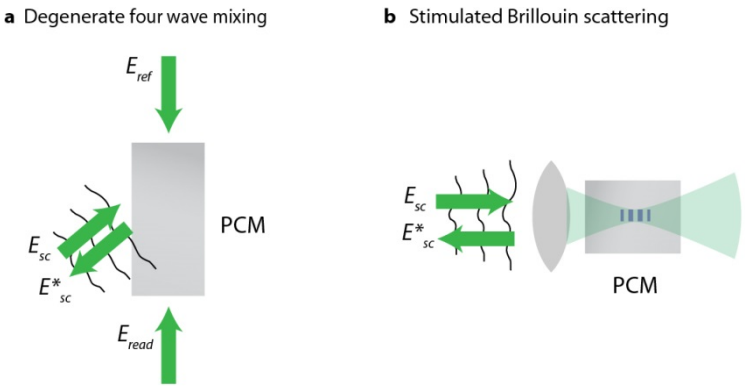

Fig. 2.3 | Schematic of degenerate four-wave mixing and stimulated Brillouin scattering. a,Degenerate four-wave mixing. We can conceptually think of degenerate four-wave mixing as real-time holography where the read and write steps occur simultaneously. The scattered wavefront E_{sc} and the reference wave E_{ref} interfere, generating a grating. The read beam E_{read} scatters off this grating immediately, resulting in E^*_{sc}. Note that the roles of E_{ref} and E_{read} are interchangeable. **b,** Stimulated Brillouin scattering**.** Stimulated Brillouin scattering (SBS) is usually achieved by focusing the pump beam (the beam to the conjugated) into a SBS medium. [2,16] The intense pump beam E_{sc} produces an acoustic wave. This acoustic wave further interacts with the input beam to result in a backscattered stokes beam. This process is the most efficient and self-reinforcing when the backscattered beam is exactly the phase conjugate of the incoming beam E^*_{sc}.

2.4 PREVIOUS WORK IN TURBIDITY SUPPRESSION USING OPTICAL PHASE CONJUGATION

The use of OPC for correction of distortions is a concept that is decades old. In fact, the first demonstration of phase conjugation for distortion compensation in etched plates was demonstrated in 1972 with SBS phase conjugation mirrors. [18,19] The theoretical groundwork [13,20] and experimental demonstrations [21,22] of DFWM for OPC through aberrating media soon followed in 1977. However, the first use of optical phase conjugation (OPC) for turbidity suppression in highly scattering biological tissues was only demonstrated in 2008. [5] In this work, static holography based OPC (using a lithium niobate crystal) was used to overcome scattering through a piece of 0.7 mm thick chicken breast tissue that did not transmit a significant ballistic component.

The phenomenon of OPC was further investigated and improved upon by McDowell et al. to show OPC through tissues up to 7 mm thick (equivalent to ~ 200 scattering events) and through tissue phantoms, where < 0.02% of the scattered wavefront was recorded and phase

conjugated. [23] This suggested that only a small portion of the wavefront needed to be phase conjugated in order to achieve an undistorted phase conjugate focus. Furthermore, it showed that the peak intensity of the phase conjugated focus decreased with increasing tissue scattering and decreasing anisotropy, which was explained in part by losses during the back-propagation of OPC beam and the fact that the reflectivity of the phase conjugate mirror is tied to the energy in the writing beams. Thus, as the energy in scattered wavefronts captured by the phase conjugate mirror decreased with increasing scattering and decreasing anisotropy, the energy in the playback beam decreased.

2.5 PERSPECTIVES AND RELEVANCE

We have discussed the theoretical basis of the use of OPC for turbidity suppression. We have also summarized the promising developments in using OPC to overcome distortions allowing focusing through highly scattering biological tissues. Nevertheless, most interesting biomedical applications require high intensity focusing inside rather than across scattering media. In chapter 4, we show how this could be made possible by combining acousto-optics with optical phase conjugation. To achieve this goal, however, there are a few major questions/issues to be addressed:

First, as discussed in this chapter, conventional phase conjugate mirrors often provide limited reflectivity. This becomes a significant issue with increasingly scattering samples, especially when the OPC focus is intended to be used for photostimulation (e.g. fluorescence excitation) or photoablation. Digital analogs of phase conjugate mirrors can be used to overcome this problem. This has indeed been suggested [2,5] and later realized and named digital optical phase conjugation (DOPC) [24]. The DOPC technique will be introduced in the next chapter. We further show in chapter 4 that DOPC can be used to phase conjugate weak ultrasound-encoded light with a reflectivity of ~5 x 10^5, enabling focal fluorescent imaging in deep tissues. Furthermore, the ability to record a wavefront by digital means allows for computational analysis of the recorded wavefront, which is crucial for the technique presented in chapter 5.

Second, although we have stated that it has been empirically shown, we have not discussed why OPC is practically possible with the capture of < 0.02% of the scattered wavefront. We briefly suggested in section 2.2 that deviations from the ideal will occur in such a scenario. In chapter 3, we will draw from the theoretical framework laid by Vellekoop et al. in wavefront shaping to explain this observation, and to quantify the expected OPC focus peak to background noise ratio in the case of non-ideal OPC. [25,26] Also in chapter 3, we will explore how small sample motions or 'sample decorrelations' degrade the OPC signal.

REFERENCES

1 Yariv, A. Phase conjugate optics and real-time holography. *Quantum Electronics, IEEE Journal of* **14**, 650-660, (1978).

2 Feldman, B.J.B., Irving J.; Fisher, Robert A.; Phipps, Claude R. Jr.; Watkins, David E.; Thomas, Scott J. . *Through the Looking Glass with Phase Conjugation*. (Los Alamos Science).

3 Wikipedia: PhaseConjugationPrinciple.en.svg <http://en.wikipedia.org/wiki/File:PhaseConjugationPrinciple.en.svg#filelink>

4 Mittra, R. & Habashy, T.M. Theory of wave-front-distortion correction by phase conjugation. *J. Opt. Soc. Am. A* **1**, 1103-1109, (1984).

5 Yaqoob, Z., Psaltis, D., Feld, M.S. & Yang, C. Optical phase conjugation for turbidity suppression in biological samples. *Nat Photon* **2**, 110-115, (2008).

6 Popoff, S., Lerosey, G., Fink, M., Boccara, A.C. & Gigan, S. Image transmission through an opaque material. *Nat Commun* **1**, 81, (2010).

7 Derode, A., Tourin, A. & Fink, M. Random multiple scattering of ultrasound. II. Is time reversal a self-averaging process? *Physical Review E* **64**, 036606, (2001).

8 Gu, C. & Yeh, P. Partial phase conjugation, fidelity, and reciprocity. *Optics Communications* **107**, 353-357, (1994).

9 Goodman, J.W. *Introduction to Fourier Optics*. 3rd edn, (Roberts and Company Publishers, 2005).

10 McDowell, E.J. *Low optical signal detection in biological materials: SNR considerations and novel techniques* Ph.D. thesis, California Institute of Technology, (2010).

11 Leith, E.N. & Upatnieks, J. Reconstructed Wavefronts and Communication Theory. *J. Opt. Soc. Am.* **52**, 1123-1128, (1962).

12 Gunter, P.H., J. P. *Photorefractive Materials and their Applications. 1 Basic Effects*. (Springer, 2006).

13 Yariv, A. & Pepper, D.M. Amplified reflection, phase conjugation, and oscillation in degenerate four-wave mixing. *Opt. Lett.* **1**, 16-18, (1977).

14 Feinberg, J. & Hellwarth, R.W. Phase-conjugating mirror with continuous-wave gain. *Opt. Lett.* **5**, 519-521, (1980).

15 Ruffin, A.B. in *Optical Fiber Measurements, 2004. Technical Digest: Symposium on.* 23-28.

16 Kong, H.J.L., S. K.; Yoon, J. W.; Shin, J. S.; Park, S.; . in *Advances in Lasers and Electro Optics* Ch. 12, (InTech, 2010).

17 Boyd, R.W. *Nonlinear Optics*. (Academic Press Inc., 1992).

18 Nosach, O.Y.P., V. I.; Ragul'Skii, V. V.; Faizullov, F. S. Cancellation of Phase Distortions in an Amplifying Medium with a "Brillouin Mirror". *ZhETF Pis ma Redaktsiiu* **Vol. 16**, 617, (1972).

19 Zel'Dovich, B.Y.P., V. I.; Ragul'Skii, V. V.; Faizullov, F. S. Connection Between the Wave Fronts of the Reflected and Exciting Light in Stimulated Mandel'shtem-Brillouin Scattering. *Journal of Experimental and Theoretical Physics Letters* **15**, 109, (1972).

20 Hellwarth, R.W. Generation of time-reversed wave fronts by nonlinear refraction. *J. Opt. Soc. Am.* **67**, 1-3, (1977).

21 Jensen, S.M. & Hellwarth, R.W. Observation of the time-reversed replica of a monochromatic optical wave. *Applied Physics Letters* **32**, 166-168, (1978).

22 Bloom, D.M. & Bjorklund, G.C. Conjugate wave-front generation and image reconstruction by four-wave mixing. *Applied Physics Letters* **31**, 592-594, (1977).

23 McDowell, E.J. *et al.* Turbidity suppression from the ballistic to the diffusive regime in biological tissues using optical phase conjugation. *Journal of Biomedical Optics* **15**, 025004-025004, (2010).

24 Cui, M. & Yang, C. Implementation of a digital optical phase conjugation system and its application to study the robustness of turbidity suppression by phase conjugation. *Opt. Express* **18**, 3444-3455, (2010).

25 Vellekoop, I.M. *Controlling the propagationg of light in disordered scattering media* PhD thesis, University of Twente, (2009).

26 Vellekoop, I.M., LagendijkA & Mosk, A.P. Exploiting disorder for perfect focusing. *Nat Photon* **4**, 320-322, (2010).

Chapter 3
Principles of Digital Optical Phase Conjugation

The digital optical phase conjugate mirror (DOPC) is an optoelectronic analog of the optical phase conjugation mirrors introduced in the last chapter and is first demonstrated by Cui and Yang. [1] Its high reflectivity and ability to dynamically analyze and manipulate wavefronts enables the digital TRUE and TROVE techniques presented in this thesis. In this chapter, we will introduce the working principles of the DOPC and describe an improved DOPC setup. In addition, we will discuss the effect of partial phase conjugation and sample motion on the fidelity of the phase conjugated wavefront.

The design and construction of the improved digital optical phase conjugation device are done in close collaboration with Dr. Benjamin Judkewitz. The section "Effect of partial phase conjugation" is adapted from the supplementary material of Wang, Y.M., Judkewitz, B.*, DiMarzio, C.A. & Yang, C. "Deep-tissue focal fluorescence imaging with digitally time-reversed ultrasound-encoded light". Nature Communications 3, 928, (2012). * Denotes equal contribution and co-correspondence.*

3.1 CONCEPT AND SETUP

Much like in static holography, the process of digital optical phase conjugation can be thought of as breaking down the OPC into two steps—wavefront recording and phase conjugate playback. Unlike in static holography, the wavefront recording is achieved using a digital camera, whereas the phase conjugate beam is obtained using a spatial light modulator which modifies a blank beam into the phase conjugate of the measured wavefront (figure 3.1 and 3.2). [1]

Wavefront measurements with digital phase-shifting holography

Without modifications, a digital camera can only detect the intensity of the field and not the phase. To measure both the phase and the amplitude of the light field, we use a technique called digital phase shifting holography. [2] To explain how this technique works,

we define the sample wavefront and the spatially flat (amplitude and phase invariant) reference beam as E_{sc} and E_{ref} respectively:

$$E_{sc}(x,y) = |E_{sc}(x,y)|\exp\,[j\varphi(x,y)] \tag{3.1}$$

$$E_{ref} = \left|E_{ref}\right| \exp[j(\omega+\theta)] \tag{3.2}$$

where ω is the phase of the reference beam; θ is the phase shifts of $0, \frac{\pi}{2}, \pi, \frac{3\pi}{2}$ that will be imposed onto the reference beam during the measurement process.

Interfering the sample and phase-stepped reference beams, like in figure 3.1, we obtain

$$\begin{aligned} I_0(x,y) &= |E_{sc}(x,y)|^2 + \left|E_{ref}\right|^2 + 2|E_{sc}(x,y)|\left|E_{ref}\right| \cos[\Delta\varphi(x,y)+0] \\ &= D.C. + 2|E_{sc}(x,y)|\left|E_{ref}\right| \cos[\Delta\varphi(x,y)] \end{aligned} \tag{3.3a}$$

$$\begin{aligned} I_{\frac{\pi}{2}}(x,y) &= |E_{sc}(x,y)|^2 + \left|E_{ref}\right|^2 + 2|E_{sc}(x,y)|\left|E_{ref}\right| \cos\left[\Delta\varphi(x,y)+\frac{\pi}{2}\right] = \\ &D.C. - 2|E_{sc}(x,y)|\left|E_{ref}\right| \sin[\Delta\varphi(x,y)] \end{aligned} \tag{3.3b}$$

$$\begin{aligned} I_{\pi}(x,y) &= |E_{sc}(x,y)|^2 + \left|E_{ref}\right|^2 + 2|E_{sc}(x,y)|\left|E_{ref}\right| \cos[\Delta\varphi(x,y)+\pi] \; = \\ &D.C. - 2|E_{sc}(x,y)|\left|E_{ref}\right| \cos[\Delta\varphi(x,y)] \end{aligned} \tag{3.3c}$$

$$\begin{aligned} I_{\frac{3\pi}{2}}(x,y) &= |E_{sc}(x,y)|^2 + \left|E_{ref}\right|^2 + 2|E_{sc}(x,y)|\left|E_{ref}\right| \cos\left[\Delta\varphi(x,y)+\frac{3\pi}{2}\right] \\ &= D.C. + 2|E_{sc}(x,y)|\left|E_{ref}\right| \sin[\Delta\varphi(x,y)] \end{aligned} \tag{3.3d}$$

We see that the relative phase of $E_{sc}(x,y)$ to that of the reference beam $\Delta\varphi(x,y)$ is now coupled to the intensity of the interference pattern.

We can remove the DC terms with some easy manipulation:

$$\begin{aligned} &I_0 - I_\pi + j\left(I_{\frac{3\pi}{2}}(x,y) - I_{\frac{\pi}{2}}(x,y)\right) = \\ &4|E_{sc}(x,y)|\left|E_{ref}\right| \cos[\Delta\varphi(x,y)] + 4j|E_{sc}(x,y)|\left|E_{ref}\right| \sin[\Delta\varphi(x,y)] \end{aligned} \tag{3.4}$$

from which we can obtain the phase and amplitude of the sample beam.

$$\Delta\varphi(x,y) = \arg\left[I_0 - I_\pi + j\left(I_{\frac{3\pi}{2}}(x,y) - I_{\frac{\pi}{2}}(x,y)\right)\right] \tag{3.5a}$$

$$|E_{sc}(x,y)| = \frac{\operatorname{abs}\left[I_0 - I_\pi + j\left(I_{\frac{3\pi}{2}}(x,y) - I_{\frac{\pi}{2}}(x,y)\right)\right]}{4|E_{ref}|} \tag{3.5b}$$

Experimentally, we phase step the reference beam by using an electro-optical phase modulator or an acousto-optic modulator. We capture the interference (intensity) pattern on a digital camera at each phase step, and perform the above operations to obtain the complex maps of the sample beam. We note here that the obtained phase map is more accurately the phase difference between the reference beam and the sample beam. However, this relative measurement is not an issue since we eventually modify the same reference beam by the measured phase shifts to obtain the phase conjugate beam.

Spatial light modulation using a liquid crystal on silicon microdisplay

The spatial light modulator (SLM) used in the experiments described in this thesis is a 1920 by 1080 parallel aligned liquid crystal on silicon (LCoS) reflective array (PLUTO, Holoeye, Germany).[3] The liquid crystals (LCs) of each individually addressed pixel change their orientation, and thus birefringence, as a function of the voltage applied (also known as electrically controlled birefringence). The Jones matrix of such LC is much like a voltage-controllable waveplate

$$W = \exp(-j\varphi(V))\begin{bmatrix}\exp(-j\beta(V)) & 0\\ 0 & \exp(j\beta(V))\end{bmatrix} \tag{3.6}$$

where β the birefringence and φ the phase offset are

$$\beta = (n_{eo} - n_o)\frac{\pi d}{\lambda} \tag{3.7a}$$

$$\varphi = (n_{eo} + n_o)\frac{\pi d}{\lambda} \tag{3.7b}$$

where n_{eo} is the extraordinary refractive index of the LCs, n_o is the ordinary refractive index of the LCs, d is the thickness of the LCs cells and λ is the wavelength of the incident light.

When linearly polarized light parallel to the extraordinary axis is incident on the liquid crystals, its phase is accordingly modified as a simple function of the voltage-controlled birefringence. This gives the phase-only modulation characteristic of the SLM. [4]

Although we can obtain phase and amplitude modulation by grouping four neighboring pixels (see reference [5]), this provides diminishing returns; as we will explain later, control over amplitude in phase conjugation does not significantly increase the phase conjugate fidelity through scattering media (see section *"Effect of partial phase conjugation"*).

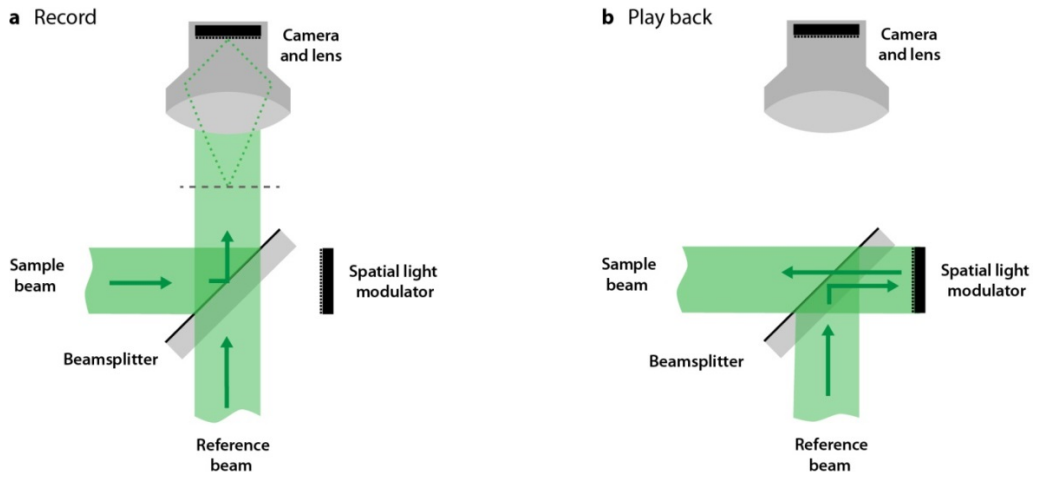

Figure 3.1 | First generation DOPC system as described in reference [1]. a, The interference pattern at the plane of the spatial light modulator (indicated by the dotted line), is imaged onto the camera. Using phase-shifting holography, the phase map of the sample beam (with respect to the reference field) can be obtained. **b,** On playback the spatial light modulator (SLM) displays the phase conjugate map. The reference beam reflected off the SLM thus becomes the phase conjugate field and is sent back to the sample. Although this arrangement is conceptually simple, the alignment process is complicated because the camera is not directly facing the SLM.

By displaying the phase conjugate of the field measured on a spatial light modulator (SLM) carefully aligned (pixel-to-pixel) at the image plane of the camera (see figure 3.1 for the first generation DOPC schematic), the same reference beam used for the field measurement can be reflected off and thus modified by the SLM to become a phase conjugate beam that propagates back through the sample. We note that the power of the phase conjugate beam is proportional only to the power of the reference beam and not that of the measured sample beam. Furthermore, because the SLM can be calibrated to work

with a wide range of wavelengths from the visible to the infrared, the DOPC is not fundamentally limited by the wavelengths of light sources.

Improvements to original DOPC setup

The pixel-to-pixel alignment of the digital camera to the SLM is a demanding task. In the approach first developed by Cui and Yang [1], a significant difficulty stems from the fact that the SLM was not directly imaged by the camera. To circumvent this, the authors first aligned the SLM to an alignment mask, which was in turn aligned to the digital camera. This process was time-consuming and made day-to-day correction of system misalignments and system drifts difficult.

In our new approach presented here, the camera directly images the light reflected off the SLM surface (see figure 3.2). As a result, the pixels on the SLM and on the camera can be easily aligned by displaying a known target pattern on the SLM and shifting the camera until the imaged pattern is at the desired pixel position on the camera. The modified process drastically reduces the complexity of system alignment, allowing for the detection and correction of misalignments on a daily basis. A practical guide to aligning this second generation DOPC system can be found in the appendix of this thesis.

One disadvantage of the second generation DOPC system is that it is less power efficient. As a result of the additional beamsplitter, only one eighth of the sample beam photons reach the detector during the recording step (as compared to half in the first generation DOPC). A similar loss in efficiency is experienced during playback. This means that a long exposure time, or a high input power in the sample beam, has to be used. In the case of biological applications, where the input power is limited by safety standards, and the exposure time is limited by sample decorrelation (due to motion), this means a reduction of signal-to-noise (SNR) in the measurements. One way to minimize this loss is to replace the first beamsplitter (that combines the reference and sample beams) by a 90:10 beamsplitter, for example. A stronger reference beam will have to be used as a result but this will only be limited by the available laser power and not by safety standards.

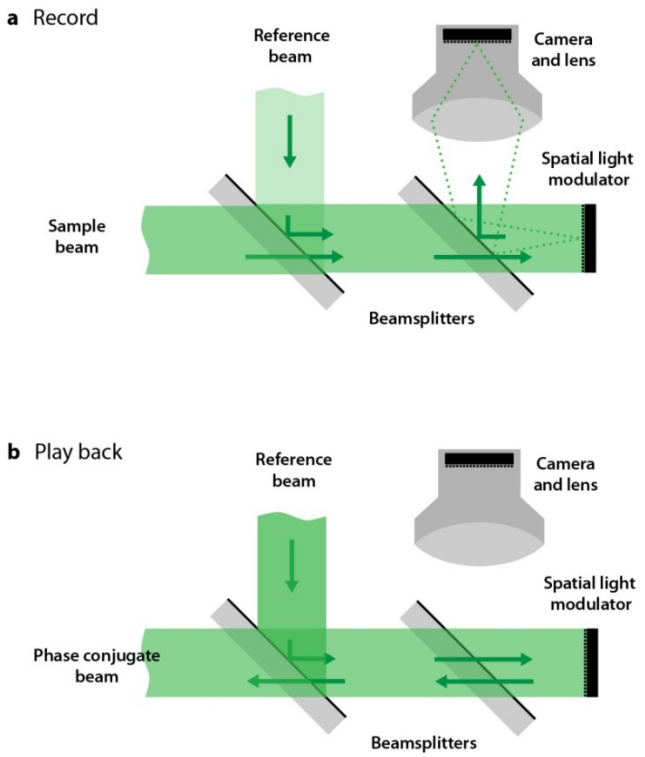

Fig. 3.2 | Second generation DOPC system: In contrast to the scheme proposed earlier by Cui and Yang[1], the spatial light modulator (SLM) is directly imaged by the camera via a beamsplitter in the new system design, allowing for ease of alignment and regular adjustments. **a,** In this configuration, the first beamsplitter combines the sample and reference beam, allowing the two to interfere. The second beamsplitter allows the camera to image the surface of the SLM (and thus eventually the wavefront at the plane of the SLM) directly. **b,** Like before, during the playback step, the reference beam reflects off the spatial light modulator that displays the phase conjugate map. Thus, the reference beam is modified by the SLM to become the phase conjugate beam.

Discussion

There are two main advantages of the DOPC over conventional phase conjugate mirrors (PCMs). First, the DOPC is capable of much higher phase conjugate gain. We noted in chapter 2 that conventional methods in achieving OPC have limited reflectivity. With static holography and stimulated Brillouin scattering, the reflectivity is usually < 1. While it is theoretically possible to achieve greater reflectivity with degenerate four wave mixing, the actual experimental gain possible is limited by the stringent amplification conditions. This is an important barrier to overcome in achieving time reversal of ultrasound-encoded light in scattering media, since the acousto-optically modulated light is very weak. The DOPC overcomes this limitation since its reflectivity is only limited by the intensity of the reference

beam incident on the SLM during playback, which is in turn limited by the damage threshold of the SLM (~2W/cm^2 for the Holoeye PLUTO).

Second, because the wavefront is digitally recorded, we can analyze the recorded wavefront and manipulate the phase conjugate wavefront. These are interesting in the context of understanding propagation through scattering medium, but also practically useful. In our demonstration of digital time reversal of ultrasound encoded light (chapter 4), the ability to easily manipulate the phase conjugate wavefront enabled an adaptive background subtraction technique used to isolate the signal originating from the phase conjugate focus from that due to its background. In the time reversal of variance-encoded light technique (chapter 5), our ability to analyze and manipulate the recorded wavefront enabled us to overcome the resolution barrier set by the ultrasound focus to achieve optical speckle sized focus.

However, the "resolution" at which the DOPC is able to phase conjugate a wavelength is limited by the number of pixels on the SLM and the digital camera. The current DOPC has ~ 2 x 10^6 pixels, limiting the maximum number of recorded and phase conjugated optical modes; whereas a typical nonlinear crystal may be able to record and phase conjugate a few magnitudes of order more, depending on the size of the crystal. In other words, in DOPC, we are sampling and phase conjugating a smaller portion of the transmission matrix (see section 2.2). We will explain the effect of this in section 3.3 with reference to the seminal work of Vellekoop et al. [6,7]

A common consideration for both DOPC and conventional PCMs is speed. This is especially important for experiments with dynamic media (e.g. live tissues, see experiments and discussions in section 3.4). Conventional PCMs are fundamentally limited by the material response time and the photosensitivity of the writing medium, whereas the DOPC is limited by hardware speeds (e.g. SLM and digital camera frame rates, currently 60 Hz and 100 Hz respectively). With foreseeable increases in hardware speeds and detection

sensitivity, we expect that the DOPC would be fundamentally shot-noise limited (see chapter 6), just like an ideal conventional PCM would be.

Various closely related studies of digital measurement and manipulation of optical wavefronts to achieve optical focusing or image transfer through disordered media have provided important theoretical foundation for our work. We will, in the next few sections, discuss these related works and draw from their insights to discuss the effect of incomplete phase conjugation and its impact on the fidelity of the OPC process in random media. Finally, we relate the performance of the DOPC system to the phase errors caused by motion of non-stationary scattering samples and experimentally validate this relationship.

Relation to other work

Other forms and applications of DOPC

The renditions of the DOPC described above are not the only ones that have been reported in literature. Soon after Cui and Yang's report on the first generation DOPC [1], Hsieh et al. presented a digital phase conjugation technique that combines digital off-axis holography with SLM playback of the conjugate wavefront to achieve digital phase conjugation to a second harmonic particle behind turbid media. [8] Hsieh's use of digital off-axis holography instead of digital phase shifting enabled one-shot determination of the wavefront. Incorporating this into our current DOPC setup would potentially enable a four-fold speed improvement. Hsieh's work was then followed by a report by Hillman et al. that incorporates Sagnac interferometry for their version of the DOPC. [9] Interestingly, other than the use of DOPC for correcting for tissue aberrations, the DOPC has also been shown to be able to correct for mode scrambling in multi-mode fibers by Papadopoulos et al. [10] This technique has been shown to be promising in enabling the use of multimode fibers in rigid endoscopes for medical applications. [11]

Wavefront shaping and transmission matrix measurement studies

DOPC is closely related to two other bodies of work—wavefront shaping and transmission matrix measurement. The key principle in both techniques is that the input

and transmitted wavefronts can each be decomposed into independent spatial modes, with the input and transmitted modes linked by a set of "transmission channels", which can be described by a transmission matrix (see chapters 1 and 2). A direct result is that the transmission can be deterministically shaped by controlling the input modes via a spatial light modulator.

In the first demonstrations of using wavefront shaping to control light propagation through scattering media, Vellekoop et al. showed that focusing can be achieved by cycling each input spatial mode through 2π and keeping the phase offset that resulted in the highest transmission to the target output mode. [6,12,13] In a way, we can think of DOPC as a deterministic wavefront shaping method, and in fact they are mathematically equivalent. Both wavefront shaping and DOPC effectively measure one column in the transmission matrix that corresponds to the transmitted mode to be optimized. [14] The optimized wavefront that will pass back through a scattering medium to converge to the initial unscattered input is exactly the phase conjugate.

If, however, the entire transmission matrix could be measured, the complete knowledge of the transmission properties of a sample will allow complete control over the light transmission through sample. Popoff et al. first demonstrated that it is possible to directly measure 60,000 elements of the transmission matrix. [15] Although this is a relatively small portion of a complete matrix, the authors showed that it is possible to use that knowledge to focus light at any desired spot across the sample without requiring further measurements. In another demonstration, Popoff et al. used the knowledge of the transmission matrix to reconstruct an image that had been randomized by the scattering medium. [16]

3.2 PARTIAL PHASE CONJUGATION

Phase conjugation is sometimes loosely described as scattered photons retracing their paths through the distorting medium to back to the location of their source. However, this view ignores the wave nature of light. Complete phase conjugation in fact requires complete

control over the phase, amplitude and polarization of the entire scattered wavefront (including the effervescent components). This is experimentally unfeasible. Because of the finite etendue of real phase conjugate mirrors, only a fraction of the scattered wavefront intercepted is phase-conjugated. As a result, the transmission matrix is no longer unitary, and $\boldsymbol{TT}^{\dagger} \neq \boldsymbol{I}$.

In this case, $\boldsymbol{TT}^{\dagger}$ still has a prominent diagonal but the off-diagonal terms are non-zero. Thus, background always exists. The transmission matrix can instead be approximated by a random matrix with elements independently drawn from a circular complex Gaussian distribution, with $\mu = 0$ and $\sigma_{real} = \sigma_{complex} = \sigma$ (reference [7]) with the following conditions: the sample is a random scattering medium, where only a small subset of the output modes are measured and manipulated; and assuming the correlations between matrix elements are negligible. The fidelity of the phase conjugate focus can be quantified as the focus peak to background ratio (PBR). It is possible to derive the PBR in relation to the number of controls on the phase conjugate mirror. [7,17] Before delving into a more rigorous theoretical proof, we can begin with a more intuitive description (figure 3.3).

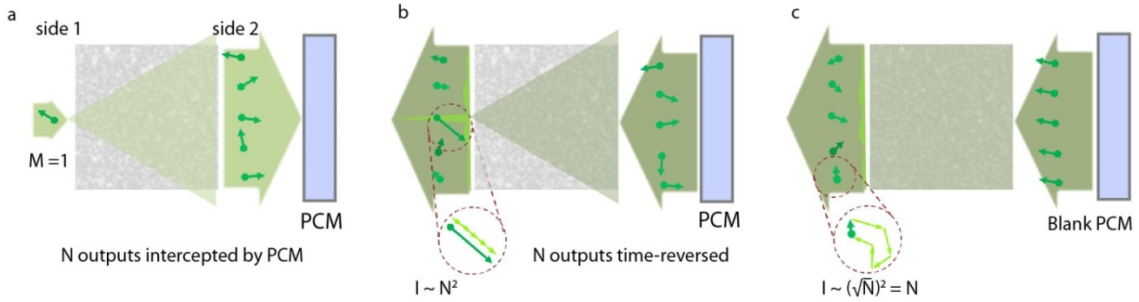

Fig. 3.3 | Intuitive explanation of peak to background ratio. a, recording: The scattering sample maps the input mode onto the N output modes intercepted by the phase conjugate mirror (PCM) on side 2. This mapping is random but deterministic, resulting in a scrambled wavefront on side 2. **b, playback:** We can send back a wavefront (phase conjugate of the recorded wavefront) on side 2 such that each mode on side 2 results in the same phase at a particular optical mode (the input mode in the recording step) on side 1. The amplitude at that location increases due to constructive interference from to each of the N time-reversed inputs, such that the intensity, $I \sim N^2$. **c, background:** At the other spatial modes on side 1, the mapped vector of each of the N time-reversed output modes add randomly, such that their average $I \sim N$. As a result, the expected peak to background ratio when time-reversing to a single spatial mode is ~ N, the number of spatial modes time-reversed by the PCM. This is also the background to be expected if the spatial light modulator displays a blank pattern.

In figure 3.3, the phasor of the single mode input propagating through the sample from side 1 is represented by the dot arrow. The random scattering sample maps the input mode onto the N output modes intercepted by the phase conjugate mirror (PCM) on side 2. This linear mapping is random but deterministic, resulting in a scrambled wavefront on side 2. Keeping in mind the deterministic nature of this mapping, we can send back a wavefront on side 2 to manipulate the wavefront on side 1. We can do so such that each mode on side 2 results in the same phase at the location of the original input mode on side 1. The wavefront that optimally does this is the phase conjugate of the scrambled wavefront. As a result, the phasors at that location add constructively such that the intensity, $I \sim N^2$. Because the other spatial modes are not optimized for, the mapped phasors of each of the N time-reversed output modes add randomly, such that their average amplitudes are $\sim \sqrt{N}$, and their $I \sim N$. As a result, the expected peak to background ratio when time-reversing to a single spatial mode is ~ N, the number of spatial modes time-reversed by the PCM. Given a randomly scattering medium, this is also the background to be expected if the phase conjugate mirror (spatial light modulator) displays a blank pattern.

In the more rigorous discussion below, we follow the framework developed by Vellekoop et al. to describe the peak to background ratio (PBR) of DOPC in two cases—phase and amplitude time reversal and phase only time reversal. The former is relevant to the general case of phase conjugation using photorefractive crystals and digital phase conjugate mirrors with phase and amplitude controls; the latter is specific for our system where only the phase of the scattered field is time-reversed. [7,17]

We consider a single mode input E_a at plane A propagating through a scattering sample described by a transmission matrix $\boldsymbol{T}$ with elements t_{ba}, which maps the input mode a to orthogonal elements b on a wavefront detector outside the sample at plane B. The transmitted (complex) speckle field can be described as $E_{transmitted} = \sqrt{\gamma} E_a \sum_b t_{ba} |b\rangle$, where γ is the phase conjugate gain. For simplicity, we assume $\gamma = 1$. Here, we further assume that the transmission matrix elements follow a complex circular Gaussian distribution (see appendix of chapter 1); the magnitude $|t_{ba}|$ of the elements follow a Rayleigh

distribution, $|t_{ba}| \sim \text{Rayleigh}(\sigma)$; and $|t_{ba}|^2$ follows the Exponential distribution, $|t_{ba}|^2 \sim \text{Exp}\left(\frac{1}{2\sigma^2}\right)$; where $2\sigma^2$ is the ensemble average intensity transmission of each matrix element and is nonzero.

Case 1: Phase and amplitude time-reversal

Assuming the phase conjugate mirror has unit reflectivity and invoking the time-symmetric property of the transmission matrix ($t_{ba} = t_{ab}$), the phase conjugate field at the location of the original input mode at plane A is:

$$E'_{\text{a}} = \sum_{b=1}^{N} t_{ab}\,(t_{ba}E_a)^* = (E_a)^* \sum_{b=1}^{N} |t_{ab}|^2 \tag{3.6}$$

and its intensity is

$$I'_a = I_a\left(\sum_{b=1}^{N} |t_{ab}|^2\right)^2 = I_a\left(\sum_{b=1}^{N} (|t_{ab}|^2)^2 + \sum_{b=1}^{N}\sum_{b\neq b'}^{N} |t_{ab}|^2 |t_{ab'}|^2\right) = I_a\alpha \tag{3.7}$$

Thus, we find that the input speckle considered is reconstructed proportional to the gain of the phase conjugate mirror together with some prefactor, α, determined by the transmission properties of the turbid medium. We can find the ensemble average of α:

$$\begin{aligned}\langle\alpha\rangle = N\langle(|t_{ab}|^2)^2\rangle + N(N-1)\langle|t_{ab}|^2\rangle^2 &= 2N(2\sigma^2)^2 + N(N-1)(2\sigma^2)^2 \\ &= N(N+1)4\sigma^4\end{aligned} \tag{3.8}$$

We will now show that the input modes at plane A with zero input will have non-zero phase conjugate intensities (i.e. $I'_m > 0\ for\ m \neq a$) , constituting a phase conjugate background. We let the transmission through channel n at plane B back to any input mode $m \neq a$ at plane A be t_{mb}. Upon playback of the phase conjugate field for E'_{a}, the intensity at plane A where $m \neq a$ is

$$I'_m = I_{\text{a}} \left|\sum_{b=1}^{N} t_{mb}t_{ba}\right|^2 = I_{\text{a}}\ \beta, \qquad for\ any\ m \neq a \tag{3.9}$$

where the ensemble average of β^2 can be found:

$$\langle\beta\rangle = \langle\left|\sum_{b=1}^{N} t_{mb}t_{ba}\right|^2\rangle = 4N\sigma^4, \qquad for\ m \neq a \tag{3.10}$$

It is clear, then, that there is non-zero average background intensity associated with the phase-conjugated speckle, and that the ratio of that phase-conjugated speckle to its background is:

$$PBR_{phase\ \&\ amplitude,\ \ single\ input\ mode} = \frac{\langle\alpha\rangle}{\langle\beta\rangle} = N + 1 \tag{3.11}$$

When there are M nonzero inputs, this result is scaled by M, such that the focal peak to background ratio (PBR) is [7]

$$PBR_{phase\ \&\ amplitude,\ \ M\ input\ modes} = \frac{N+1}{M} \tag{3.12}$$

Experimentally, N is related to the number of uncorrelated speckles intercepted by the phase conjugate mirror and its upper limit is determined by the number of pixels on the spatial light modulator.

Case 2: Phase only time-reversal

In the case where a phase-only phase conjugate mirror is used, the phase-conjugated electric field and intensity of the input speckle, respectively, are [16,18]

$$E'_{\mathrm{a}} = (E'_{\mathrm{a}})^* \sum_n^N t_{ab} \exp\left[-i \cdot Arg(t_{ba})\right] = \sum_n^N \left|t_{ab}\right|, \tag{3.13}$$

$$E'_{\mathrm{a}} = I_{\mathrm{a}} \left[\sum_n^N \left|t_{ab}\right|\right]^2, \tag{3.14}$$

and the derivation of $PBR_{phase\ only}$ follows exactly that of references [7, 18] for the case of iterative wavefront optimization to multiple targets through scattering medium. We include the derivation here for completeness and comparison: [16,18]

$$I'_a = I_a\left(\sum_{b=1}^N |t_{ab}|\right)^2 = I_a\left(\sum_{b=1}^N |t_{ab}|^2 + \sum_{b=1}^N \sum_{b\neq b'}^N |t_{ab}||t_{ab'}|\right) = I_a\alpha\ , \tag{3.15}$$

$$\langle\alpha\rangle = N\langle|t_{ab}|^2\rangle + N(N-1)\langle|t_{ab}|\rangle^2 = 2N\sigma^2 + N(N-1)\frac{\pi}{2}\sigma^2. \tag{3.16}$$

The background can also be derived:

$$I'_a = I_a \left| \sum_{b=1}^{N} t_{mb} \exp\left[-i \cdot Arg(t_{ba})\right] \right|^2 = I_a \beta \,, \tag{3.17}$$

$$\langle \beta \rangle = N 2\sigma^2 \,. \tag{3.18}$$

Thus, the PBR for phase only optical phase conjugation is:

$$PBR_{phase\ \&\ amplitude,\ \ single\ input\ mode} = \frac{\langle \alpha \rangle}{\langle \beta \rangle} = \frac{\pi}{4}(N-1) + 1 \approx \frac{\pi}{4} N, \quad N \gg 1 \,. \tag{3.19}$$

$$PBR_{phase\ only,\ \ M\ input\ modes} = \frac{\frac{\pi}{4}(N-1)+1}{M} \,. \tag{3.20}$$

Experimental setup and results

Our DOPC system is performs phase-only OPC. The effective number of controls on our system, N, is a useful quantity to determine in our system. We see from equation (3.18) that with sufficiently large N, the PBR (when phase conjugating to a single spatial mode) varies directly with N. Thus, by measuring the PBR achievable with our DOPC, we can directly estimate N. It is also useful to compare the achievable PBR with the theoretically expected PBR. N represents the number of independent spatial modes (essentially, the number of speckles) that are intercepted and phase conjugated. In the ideal case of one independent pixel to one speckle matching, N would simply be limited by the number of pixels on the camera and/or on the SLM. However, this is practically limited by pixel cross talk of the SLM.

The number of speckles in the phase map (see e.g. in figure 3.4) can be estimated as long as we know the average size of speckles on the SLM, which is equivalent to the full-width at half maximum of the speckle intensity autocorrelation or the square of the speckle field autocorrelation. In our experiments, each speckle spans an average of ~2.5 pixels. To measure the achieved PBR, we use an observing camera that images the OPC focus. Figure 3.5a shows a typical OPC intensity field when a phase conjugate field is displayed. To obtain the value of the average background, we digitally shift the phase map to disrupt the OPC

focus (figure 3.5b). Typically, we achieve ~ 25% of the theoretical PBR. The errors can be attributed to SLM pixel cross-talks, alignment errors and phase errors due to deviations from flatness of the SLM, beamsplitters, etc.

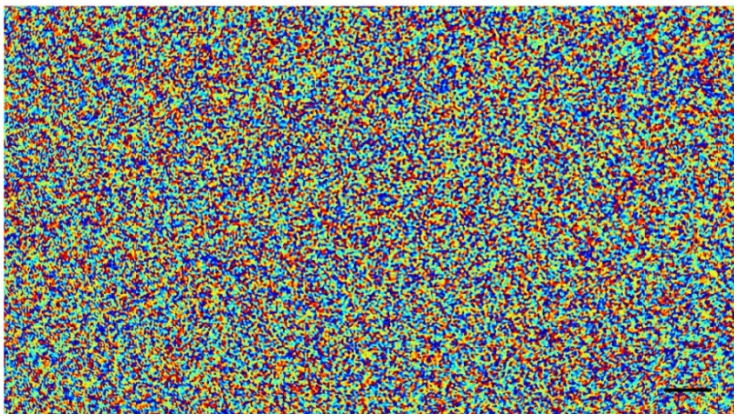

Fig. 3.4 | Representative area of a typical phase map. Average speckle size on SLM occupies ~ 2.5 pixels (~ 20 μm). Scale bar: 500 μm.

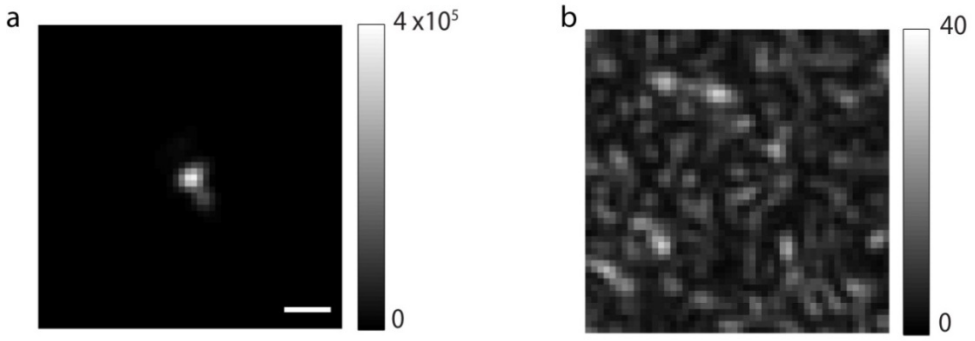

Fig. 3.5 | Results of typical DOPC experiment. a, DOPC focus. **b,** Background. Note: The OPC field detected is not polarized. The background should be halved if a polarized is placed in front of the observation camera. Scale bar: 5 μm.

Discussion

Here we have discussed the effects of partial phase conjugation on the fidelity of the DOPC field as measured by the peak to background ratio (PBR) of the DOPC focus. We have further explained via theoretical derivations by Vellekoop et al. that the PBR is directly

proportional to the N number of controls on the DOPC. [7] Currently, N is limited by the number of pixels on the camera and the SLM (1920 by 1080). As discussed in section 3.1, although the DOPC offers higher optical gain, its N is orders of magnitude lower than traditional nonlinear crystal based PCMs. However, this is set to change with the increasing format of cameras and SLMs.

We should also note here that the derivations discussed here assume perfectly randomly scattering samples with low anisotropy, where the assumption of a random uncorrelated transmission matrix is a good approximation. For a scattering medium with high anisotropy, correlations between matrix elements become significant. [19] Thus, although derived equations give a first order estimation of the PBR, the exact form of the OPC field in cases that deviate from perfectly random scattering can only be obtained through more thorough modeling of the correlations that exists in the specific sample. This is an interesting and important direction for future work.

3.3 SAMPLE MOTION

Up to this point, our models have assumed that the samples are completely stationary. In other words, the transmission matrix does not change over time or between the measurement of the wavefront and the playing back of its phase conjugate. However, in reality, most samples exhibit mechanical instabilities ("sample decorrelation") over time due to Brownian motion, sample translation, diffusion, etc. As a result of these mechanical instabilities, our assumption of an unchanging transmission matrix becomes invalid and we would expect the OPC focus to degrade. Here, we present a mathematical description of how sample decorrelation degrades the OPC peak-to-background ratio. This description is based on the investigations of the effect of phase and amplitude errors in wavefront shaping in reference [18].

Theory

If we play back the phase conjugate field immediately (before the scatterer configuration in the sample changes), we obtain the familiar description of the phase conjugate focus at the input,

$$E_a{}' = E_a \sum_b |t_{ab}|^2 \tag{3.21}$$

where to resultant peak to background ratio is determined by the number of transmitted modes recorded and phase conjugated by the phase conjugate mirror (see Chapter 3).

However, if the sample moves between the recording (time = t1) and playback (time = t2) such that $t_{ab,1} \neq t_{ab,2}$, then the phase conjugate focus would instead be

$$E_a' = \sum_b \left[E_a t_{ba,t1}\right]^* t_{ab,t2} = E_a{}^* \sum_b \left|t_{ab,t2}\right|^2 \ \mathrm{A}e^{-i\Delta\varphi} \tag{3.22}$$

where $A = \frac{|t_{ba,t2}|}{|t_{ba,t1}|}$ and $\Delta\varphi = \arg(t_{ba,t2}) - \arg(t_{ba,t1})$.[18] (i.e., the amplitude ratio and the phase difference between the elements of the transmitted matrix at the two time points. Also, note the resemblance to complex cross-correlation. [18]) Since the OPC background does not change, expected relative decay of the peak to background ratio at t1 and t2 is

$$\frac{I_a''}{I_a'} = \left|\frac{E_a''}{E_a'}\right|^2 = \left|\frac{\sum_b |t_{ab,t2}|^2 A e^{-i\Delta\varphi}}{\sum_b |t_{ab,t1}|^2}\right|^2 \tag{3.23}$$

In phase-only phase conjugate experiments, the expected relative decay of the peak to background ratio at t1 and t2 is

$$\frac{I_a''}{I_a'} = \left|\frac{\sum_b |t_{ab,t2}| e^{-i\Delta\varphi}}{\sum_b |t_{ab,t1}|}\right|^2. \tag{3.24}$$

Since $E_a t_{ba}$, rather than t_{ab} ,is an easily measurable quantity in our DOPC setup (and noting that $t_{ab} = t_{ba}$ due to reciprocity), we can re-express the equation above, obtaining

$$\frac{I_a''}{I_a'} = \left|\frac{\sum_b |E_a t_{ba,t2}| e^{-i\Delta\varphi}}{\sum_b |E_a t_{ba,t1}|}\right|^2. \tag{3.25}$$

The derivations here show that the degradation of the OPC focus is related to the sum of the pixel-to-pixel phase error between the OPC field measured at t = 0 and the OPC field measured at a later time.

Experimental setup and results

To verify this relationship experimentally, we used five different samples: Intralipid in 2% agar (3 mm thick, $\mu_s l$ ~ 18), Intralipid in 4% agar (3 mm thick, $\mu_s l$ ~ 18), 2.5 mm chicken breast tissue ($\mu_s l$ ~ 75 [20,21]), 5 mm chicken breast tissue ($\mu_s l$ ~ 150 [20,21]), and 1 mm chicken breast tissue fixed in ethanol ($\mu_s l$ ~ 33). A schematic of the optical setup is shown in figure 3.6. We measured the transmitted complex field at 12 second intervals.

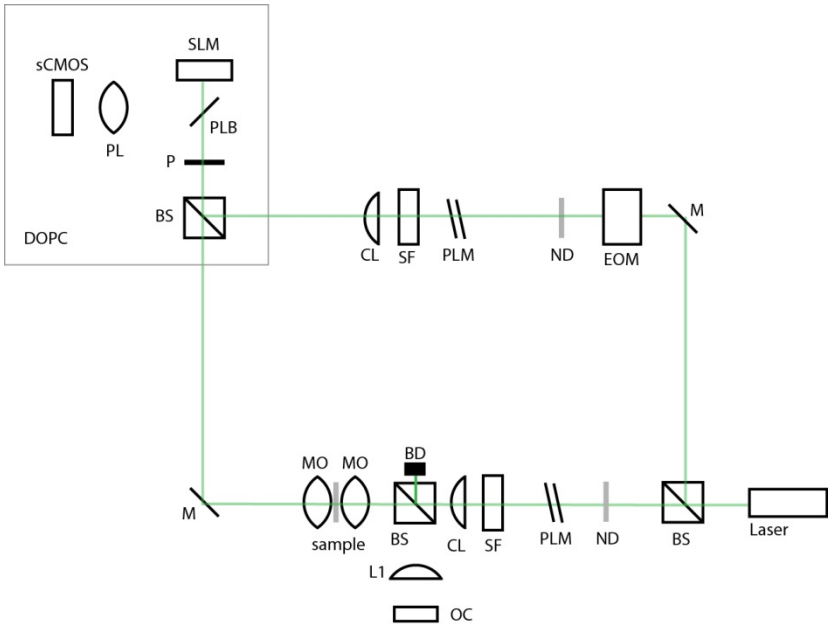

Fig. 3.6 | Schematic of DOPC setup for decorrelation measurements. DOPC, digital optical phase conjugation setup; sCMOS, scientific CMOS camera; PL, photography lens; SLM, spatial light modulation; PLB, plate beamsplitter; P, polarization; BS, cube beamsplitter; CL, collimating lens; SF, spatial filter; PLM, pathlength matching arm; ND, neutral density filter; EOM, electro-optic phase modulator; M, mirror; BD, beam dump; L1, planoconvex lens; OC, observing camera; MO, microscope objective lens.

Playing back the first phase map (phase map at t = 0s) at all later time points, we observe the DOPC focus intensity decay due to sample decorrelation. We calculated the expected DOPC decay according to equation (3.25). Comparing the expected OPC decay with the observed DOPC decay, we obtain the results shown in figure 3.7. We found a good match between the expected DOPC signal decay as predicted by the model derived and the actual DOPC signal decay.

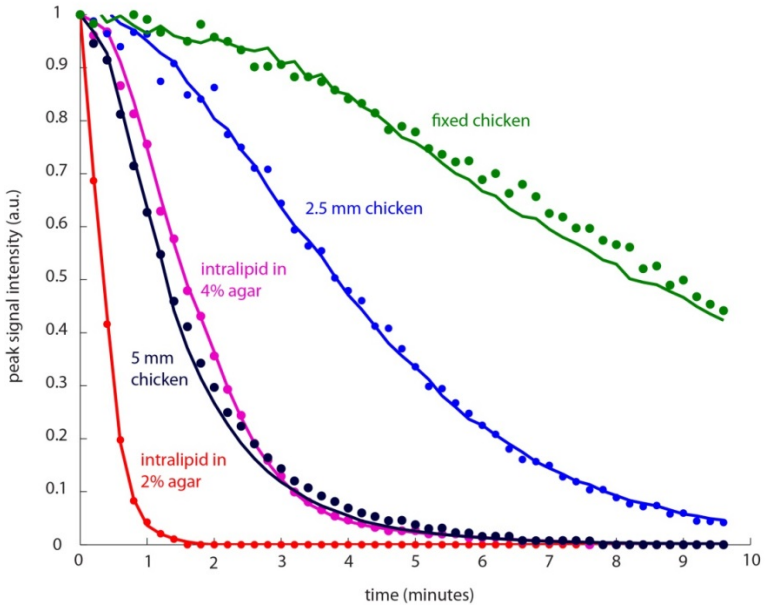

Fig. 3.7 | Phase conjugate focus decay with time due to sample decorrelation. Dots represent measured signal decay and solid lines represent expected signal decay due to measured phase changes. Decay half times: 2% agar with Intralipid, 20 s; 5 mm chicken, 80 s; 4% agar with Intralipid, 95 s; 2.5 mm chicken breast tissue, 230 s; fixed chicken breast tissue, 495 s.

Discussion

We have previously mentioned that an intrinsic assumption in the theoretical descriptions of OPC is that the scattering medium is static (i.e. the transmission matrix is time-invariant). However, this is not true for real samples. Here, we showed that the decay of the DOPC focus is a direct result of phase errors that occur due to sample motion. Intuitively, we can explain this by the following: as the scatterers in the scattering medium move, the transmission matrix changes, resulting in a cumulative phase error that corresponds to the decay of the DOPC focus intensity. The phase errors can be quantified

and their effects on DOPC fidelity can be predicted using the model derived. As the sample decorrelates, the phase error increases, resulting in the decay of the DOPC signal. We note that the decorrelation time constants measured here are highly dependent on mounting, temperature, and time to equilibrate etc. In our experiments, we gave the samples a similar amount of time to equilibrate.

When the samples have high anisotropy, the correlations in the transmission matrix for each specific sample may have to be considered. In addition, when the input field contains many speckles (spatial modes), this analysis will only be valid in describing the average decay of the signal over the various spatial modes. Otherwise, some assumptions will have to be made about the changes in the transmission matrix (i.e. the accumulative errors in each row of the transmission matrix that correspond to each input mode are approximately the same). In our experiments, we ensured a single mode input.

The first measurements of OPC signal decay over time in a live rabbit's ear were reported by Cui, McDowell and Yang. [22] The team used a Lithium Niobate crystal in a static holography setup to perform OPC and found that the OPC signal was robust even in the presence of tissue motion. Because the wavefront was not measured digitally, no measurement of transmission matrix changes could be made. In addition, because of the slow response time of the crystal (5 s), it is possible that some faster dynamics could have been missed. Although our DOPC repetition rate here was not faster, it was sufficient in light of the slower dynamics of the tissue phantoms and the *ex vivo* tissues. With faster cameras and SLMs, it would be possible to push the speed limits of the DOPC to enable *in vivo* measurements with time resolution on the order of tens to hundreds milliseconds (see chapter 6). With speed improvements and the innate ability of the DOPC to measure the changes in the transmission matrix, we expect to be able to gain important insights to the phenomenon of OPC in living systems.

3.4 CONCLUSIONS AND OUTLOOK

In this chapter, we discussed the working principles of DOPC and presented an improved method for easier and more robust construction of the DOPC. We also related the DOPC to other bodies of work in wavefront shaping and transmission matrix measurements. Drawing from the insights from those studies, we discussed the effect of partial phase conjugation and sample motion in relation to DOPC.

So far, we described OPC and DOPC in the context of focusing across scattering samples. We note that for most biomedical applications, it is most important to focus inside. One way to achieve this is to measure and phase conjugate light from a "beacon" within the tissue. Hsieh et al. demonstrated this concept with a second harmonic particle. [8] Because the emission of the second harmonic particle is coherent, the scattered second-harmonic wavefront that originates from the particle, which can be hidden inside a scattering medium, can be measured with a reference beam produced by second harmonic generation with a β-Barium Borate crystal. In another example, Vellekoop, Cui, and Yang recently devised reference free method to phase conjugate fluorescence emission from a bead hidden behind a piece of tissue. [23]

Both examples described above did not depend on direct optical access to the emitting bead. However, the conditions of the presence of a "beacon" and the sparseness of the distribution of the beacon must be fulfilled. This constraint is difficult to meet in real biological studies, unless beads (with emissions distinct from the surrounding biological material) are artificially introduced to the vicinity of targeted imaging areas. In the next two chapters, we present two methods—digital time reversal of ultrasound-encoded light (TRUE) and time reversal of variance-encoded light (TROVE)—that overcome the above constraints using an ultrasound guide star. [21,24]

REFERENCES

1 Cui, M. & Yang, C. Implementation of a digital optical phase conjugation system and its application to study the robustness of turbidity suppression by phase conjugation. *Opt. Express* **18**, 3444-3455, (2010).

2 Yamaguchi, I. & Zhang, T. Phase-shifting digital holography. *Opt. Lett.* **22**, 1268-1270, (1997).

3 Lizana, A. *et al.* in *Advanced Holography - Metrology and Imaging* (ed I. Naydenova) (InTech, 2011).

4 Lazarev, G., Hermerschmidt, A., Kruger, S. & Osten, S. in *Optical Imaging and Metrology: Advanced Technologies* (eds W. Osten & N. Reingand) Ch. 1, (Wiley-VCH Verlag GmbH & Co. KGaA, 2012).

5 van Putten, E.G., Vellekoop, I.M. & Mosk, A.P. Spatial amplitude and phase modulation using commercial twisted nematic LCDs. *Appl. Opt.* **47**, 2076-2081, (2008).

6 Vellekoop, I.M., LagendijkA & Mosk, A.P. Exploiting disorder for perfect focusing. *Nat Photon* **4**, 320-322, (2010).

7 Vellekoop, I.M. *Controlling the propagationg of light in disordered scattering media* PhD thesis, University of Twente, (2009).

8 Hsieh, C.-L., Pu, Y., Grange, R. & Psaltis, D. Digital phase conjugation of second harmonic radiation emitted by nanoparticles in turbid media. *Opt. Express* **18**, 12283-12290, (2010).

9 Hillman, T.R. *et al.* Sagnac-interferometry-based digital optical phase conjugation (DOPC) system for turbidity suppression. 790417-790417, (2011).

10 Papadopoulos, I.N., Farahi, S., Moser, C. & Psaltis, D. Focusing and scanning light through a multimode optical fiber using digital phase conjugation. *Opt. Express* **20**, 10583-10590, (2012).

11 Papadopoulos, I.N., Farahi, S., Moser, C. & Psaltis, D. High-resolution, lensless endoscope based on digital scanning through a multimodeoptical fiber. *Biomed. Opt. Express* **4**, 260-270, (2013).

12 Vellekoop, I.M. & Mosk, A.P. Focusing coherent light through opaque strongly scattering media. *Opt. Lett.* **32**, 2309-2311, (2007).

13 Vellekoop, I.M., van Putten, E.G., Lagendijk, A. & Mosk, A.P. Demixing light paths inside disordered metamaterials. *Opt. Express* **16**, 67-80, (2008).

14 Mosk, A.P., Lagendijk, A., Lerosey, G. & Fink, M. Controlling waves in space and time for imaging and focusing in complex media. *Nature Photonics* **6**, 283-292, (2012).

15 Popoff, S.M. *et al.* Measuring the Transmission Matrix in Optics: An Approach to the Study and Control of Light Propagation in Disordered Media. *Physical Review Letters* **104**, 100601, (2010).

16 Popoff, S., Lerosey, G., Fink, M., Boccara, A.C. & Gigan, S. Image transmission through an opaque material. *Nat Commun* **1**, 81, (2010).

17 Vellekoop, I.M. & Mosk, A.P. Universal Optimal Transmission of Light Through Disordered Materials. *Physical Review Letters* **101**, 120601, (2008).

18 van Putten, E.G. *Disorder-enhanced imaging with spatially controlled light* PhDs thesis, University of Twente, (2011).

19 van Albada, M.P., de Boer, J.F. & Lagendijk, A. Observation of long-range intensity correlation in the transport of coherent light through a random medium. *Physical Review Letters* **64**, 2787-2790, (1990).

20 McDowell, E.J. *et al.* Turbidity suppression from the ballistic to the diffusive regime in biological tissues using optical phase conjugation. *Journal of Biomedical Optics* **15**, 025004-025004, (2010).

21 Wang, Y.M., Judkewitz, B., DiMarzio, C.A. & Yang, C. Deep-tissue focal fluorescence imaging with digitally time-reversed ultrasound-encoded light. *Nat Commun* **3**, 928, (2012).

22 Cui, M., McDowell, E.J. & Yang, C. An in vivo study of turbidity suppression by optical phase conjugation (TSOPC) on rabbit ear. *Opt. Express* **18**, 25-30, (2010).

23 Vellekoop, I.M., Cui, M. & Yang, C. Digital optical phase conjugation of fluorescence in turbid tissue. *Applied Physics Letters* **101**, (2012).

24 Judkewitz, B., Wang, Y.M., Horstmeyer, R., Mathy, A. & Yang, C. Speckle-scale focusing in the diffusive regime with time reversal of variance-encoded light (TROVE). *Nat Photon* **7**, 300-305, (2013).

Chapter 4
Deep Tissue Focal Fluorescence Imaging with Digitally Time-reversed Ultrasound-encoded Light

This chapter is reproduced with some adaptations from the manuscript Wang, Y.M., Judkewitz, B.*, DiMarzio, C.A. & Yang, C. Deep-tissue focal fluorescence imaging with digitally time-reversed ultrasound-encoded light. Nat Commun 3, 928 (2012). The contributions of the authors are as follows: YMW and BJ contributed equally to this work. CY and CAD conceived the initial idea. YMW, BJ and CY developed and the idea and the imaging scheme. The experiments were designed and performed by YMW and BJ. The data analyses were performed by YMW and BJ.*

Fluorescence imaging is one of the most important research tools in biomedical sciences. However, scattering of light severely impedes imaging of thick biological samples beyond the ballistic regime. Here we directly show focusing and high-resolution fluorescence imaging deep inside biological tissues by digitally time-reversing ultrasound-tagged light with high optical gain (~ 5 x 10^5). We confirm the presence of a time-reversed optical focus along with a diffuse background—a corollary of partial phase conjugation—and develop an approach for dynamic background cancellation. To illustrate the potential of our method, we image complex fluorescent objects and tumor microtissues at an unprecedented depth of ~ 2.5 mm in biological tissues at a lateral resolution of 36 μm by 52 μm and an axial resolution of 657 μm. Our results set the stage for a range of deep tissue imaging applications in biomedical research and medical diagnostics.

4.1 INTRODUCTION

Realizing high-resolution fluorescence imaging within scattering biological tissues is a central goal in biomedical imaging. Considerable efforts have been made to extend the imaging depth of optical methods [1-7], but focal excitation of fluorescence has so far been fundamentally limited to a depth of one transport mean free path, or approximately one

millimeter in most biological samples. This is because conventional focusing approaches treat scattered light as noise and select for the ballistic light component, which exponentially decreases with depth. However, scattered light contains important information about the sample, which can in fact be utilized. When light passes through scattering samples, its wavefront is seemingly randomized, but the randomization occurs in a deterministic and time-symmetric way. These properties of elastic light scattering have recently been used to focus light through turbid samples by iterative wavefront optimization [8-15] and by time-reversal using optical phase conjugation [10,16-18]. These methods are, in many ways, analogous to adaptive optics methods used in astronomy to cancel out the effect of atmospheric scattering [19,20]. However, in contrast to astronomy where it is sufficient to image through a turbid medium (the atmosphere), the goal of biomedical imaging is to image inside.

To achieve focusing inside tissues, Xu *et al.* [21] proposed a scheme termed time-reversal of ultrasound encoded light (TRUE), which combines optical phase conjugation [22] with ultrasound encoding [23]. They used focused ultrasound, which is much less scattered than light in biological tissues, to create a virtual source of light frequency-shifted by the acousto-optic effect. Scattered light emanating from this source was then time-reversed by a photorefractive crystal acting as a phase conjugate mirror. The authors inferred the formation of a time-reversed optical focus from a line-scan across millimeter-scale absorbers embedded in tissue-mimicking phantoms. While promising improved absorption contrast [21,24,25], the use of this technique for high-resolution fluorescence imaging in biological tissues remains fundamentally challenging. Because of the low ultrasound modulation efficiency [26], the phase conjugate mirror has to provide orders of magnitude higher than unity gain to excite detectable fluorescence. This requirement have not been met by traditional phase conjugate mirrors based on photorefractive crystals whose gain is typically much less than one [27,28].

Moreover, the significant challenge of undesired background illumination due to partial phase conjugation needs to be addressed. With complete time reversal, the TRUE focusing technique can be conceptually represented as photons retracing their paths back to

the location of the virtual source. However, this view disregards the wave nature of light: complete time reversal requires full control over phase, amplitude and polarization of the entire scattered field over the full solid angle—which is fundamentally unfeasible (see "Setup and Principles"). As a result, even with perfectly aligned optics and noise-free recording of the scattered wavefront, the time-reversed focus is necessarily accompanied by a background [29-31] which would obscure the fluorescence signal originating at the desired optical focus.

Here we present a new strategy to overcome these challenges by combining digital phase conjugation [32] with dynamic wavefront manipulation. We directly visualize the formation of an optical focus, exciting fluorescence between layers of highly scattering tissue. In doing so, we confirm the presence of the accompanying background predicted by theory that can be dynamically reproduced and subtracted. This digital background cancellation procedure, along with the high phase conjugate gain and resolution of our technique, enables the first demonstration of focused fluorescence imaging ~ 2.5 mm deep inside biological tissue.

4.2 SETUP AND PRINCIPLES

Our setup for fluorescence imaging with time-reversed light is diagrammatically shown in figure 4.1. The complete setup diagram can be found in the appendix. Since the performance of our approach critically depends on achievable resolution, phase conjugate mirror gain and fidelity of phase conjugation these parameters deserve further discussion.

Light scatters as it propagates through tissue, resulting in a speckled light field at the ultrasound focus. The speckles within the ultrasound focus are frequency-shifted via the acousto-optic effect, creating a source of frequency-shifted light (figure. 4.1a). Since our technique selectively records and phase conjugates the frequency-shifted light, the size of the ultrasound-modulated volume determines the resolution of the phase conjugated optical

focus. We use a high numerical aperture focused ultrasound with a beam diameter BD of 34 μm, estimated according to [55]:

$$BD = 1.02Fc/fD \tag{4.1}$$

where F is the focal length of the transducer (6 mm), c is the speed of acoustic wave in medium, (~ 1580m/s in polyacrylamide [56] and assumed to be similar in chicken breast tissue in this approximate calculation), f is the frequency (45 MHz in our experiments) and D is the transducer element diameter (6.35 mm). To further confine the ultrasound-modulated volume along the axis of ultrasound propagation, we operate both the ultrasound source and the laser in pulsed mode [33] such that light only enters the sample when the ultrasound pulse has reached the target modulation volume (see Methods). The modulated dimension along the axis of ultrasound propagation d_y can be calculated according to:

$$d_y = v \times t \tag{4.2}$$

where v is the propagation velocity of sound in medium and t is the ultrasound pulse length (~ 53 μm in our experiments). With traditional phase conjugate mirrors, the power in the phase conjugated beam is proportional to the power in the signal beam [28]. Because of the low ultrasound modulation efficiency and the small area ratio between ultrasound focus and scattered wavefront, the scattered light field reaching the phase conjugate mirror consists mostly of light that is not frequency-shifted (f_0) and a minute fraction (in our setup ~ 10^{-5} to < 10^{-4} *[1] of the total power incident on the DOPC) of frequency-shifted, ultrasound-tagged light ($f_0 \pm f_{US}$). Therefore, to excite detectable fluorescence at the optical phase conjugate focus, a phase conjugate mirror with gain orders of magnitude larger than unity is required. This is currently not achievable by traditional phase conjugate mirrors, even with advanced phase conjugation schemes [34-36].

*[1] The estimation was inaccurately expressed as "on the order of 10^{-4}" in original publication. We also note here that the presence of noise in our measurement may have resulted in an overestimation.

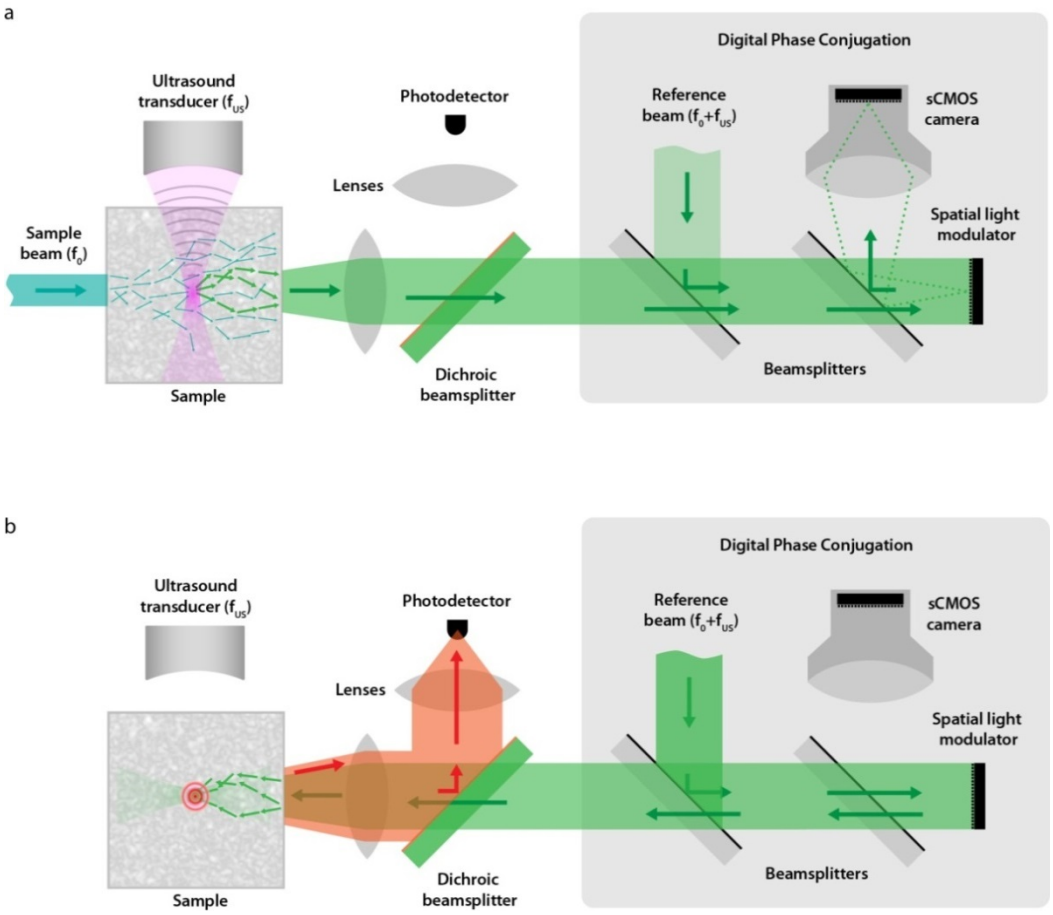

Fig. 4.1 | Schematic of the imaging principle. **a** In the recording step, a 0.8 mm wide sample beam (f0) scatters as it propagates through the tissue sample. A confined region of the scattered light in the tissue sample is frequency-shifted ($f_0 \pm f_{US}$) by a focused ultrasound pulse. The ultrasound focus thus becomes a virtual source within the tissue. Both the frequency-shifted light and the non-shifted light further scatter through the tissue and are collected. This output wavefront interferes with a reference beam (f_0+f_{US}) and the resulting interference pattern is imaged onto a scientific CMOS (sCMOS) camera in the digital phase conjugate mirror module. The digital phase conjugate mirror selectively measures the phase map ($\Phi(x,y)$) of the frequency-shifted light through digital phase-shifting holography. The ultrasound is turned off after recording. **b** In the playback step, the conjugate of the recorded phase map ($-\Phi(x,y)$) is displayed on a spatial light modulator (SLM) placed at the image plane of the sCMOS camera. The reference beam reflects off the spatial light modulator and is transformed into the phase conjugate beam that is propagated back into the tissue, reconstructing an optical focus at the ultrasound modulation location. Any excited fluorescence is collected and measured outside the tissue using a photodetector.

To selectively phase conjugate only the frequency-shifted light with high gain, we implement an improved digital optical phase conjugation scheme (DOPC) that consists of a high dynamic range sCMOS camera and a high-resolution phase-only spatial light modulator (SLM) [32]. The scattered, ultrasound-tagged light field interferes with an equally

frequency-shifted reference beam ($f_o + f_{US}$) and is imaged onto the sCMOS camera. Using digital phase-shifting holography [37], the phase of the frequency-shifted wavefront ($\Phi(x,y)$) with respect to the reference beam is measured. By reflecting off a phase-only spatial light modulator displaying a phase conjugate map ($-\Phi(x,y)$) at the image plane of the camera, the same reference beam is modulated to become a phase-conjugate beam that is sent back into the sample (figure 4.1b). The phase-conjugate beam traverses back through the tissue sample to converge at the location of the ultrasound focus resulting in an optical focus deep inside the tissue sample.

In our DOPC setup, the power in the phase conjugate light that leaves the DOPC setup is only dependent on the power in the reference beam that reflects off the SLM displaying the phase conjugate map; thus, the DOPC is fundamentally not limited in terms of gain. In our experiments, we adjusted the intensity of the reference beam during playback to achieve a gain of ~ 5 x 10^5, such that the phase conjugate focus is sufficiently intense to excite fluorescence that can be collected and detected outside of the tissue by a photomultiplier tube (PMT).

Theoretically, with complete phase-conjugation, the light field within the ultrasound focus can be reconstructed without error (see chapter 2.1). However, the assumption of complete phase-conjugation breaks down in practice—real phase-conjugate mirrors, whether based on photorefractive crystals or spatial light modulators, have finite etendue and can only intercept a fraction of the output wavefront. As a result, a background always exists in the case of partial phase conjugation [29-31]. In a random scattering medium, the ratio of the peak intensity of the phase conjugate focus to the average intensity of the accompanying background, the peak to background ratio (PBR), can be analytically derived. Following the derivations of Vellekoop et. al. [38], we find that the peak to background ratio is determined by the number of optical modes intercepted and time-reversed by the phase conjugate mirror, N, and the number of input modes in the ultrasound focus, M (see chapter 3.3). When both phase and amplitude of the scattered field are time-reversed, a case similar

to the use of traditional phase conjugate mirrors, the peak to background ratio can be estimated as:

$$PBR_{phase\ \&\ amplitude} = \frac{N+1}{M} \tag{4.3}$$

when only the phase of the scattered field is time-reversed, a case similar to our technique employing the DOPC, the peak to background ratio for large N is:

$$PBR_{phase\ only} = \frac{\frac{\pi}{4}(N-1)+1}{M} \approx \frac{\pi}{4} \cdot PBR_{phase\ \&\ amplitude} \tag{4.4}$$

Since N is finite in a real phase conjugation setup, a phase conjugate background is inevitable. In our experimental setup, N is limited by the number of optical modes imaged onto the spatial light modulator and the fact that only the horizontally polarized component is measured and time-reversed. The diffuse background that inevitably results can excite fluorophores outside of the focus, contributing to noise in the detected fluorescence signal. Because of its spatial extent, the total background excitation can drown the desired focal fluorescence signal detected by a single channel PMT outside the sample. We show in our experiments that this background, though indeed significant, can be dynamically subtracted by digital manipulation of the measured phase conjugate map, allowing us to realize high-resolution focal fluorescence imaging in biological tissues.

4.3 RESULTS

Direct visualization of optical focus

To directly visualize and characterize the focus formed by time-reversed light, we placed an optically transparent hydrogel slab containing a thin quantum dot layer between two pieces of *ex vivo* chicken breast tissue, ~ 2.5 mm thick each (figure 4.2a). When we focused light into the tissue with a simple lens without any wavefront manipulation (flat phase display on the spatial light modulator), the light was highly scattered and failed to form a focus (figure 4.2b). In contrast, figure 4.2c shows the fluorescence excited by phase

conjugation of ultrasound frequency-shifted light. A cone of light converging into the location of the ultrasound focus was clearly visible, albeit on a significant background. Taking into account the thickness of the quantum dot sheet (~ 500 μm) and the expected size of the ultrasound focus (34 μm in the x direction, see Methods), the peak to background ratio was determined as ~ 5.5 in this geometry. The peak to background ratio is expected to be lower in geometries where the sample is embedded immediately between tissues.

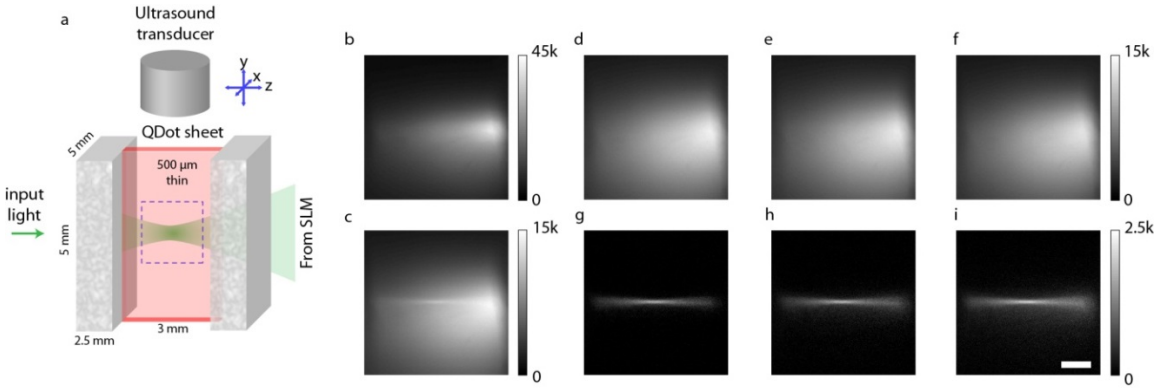

Fig. 4.2 | Demonstration of optical focusing between thick layers of biological tissue. a, Schematic of the sample arrangement, consisting of a thin sheet of quantum dots between two 2.5 mm thick sections of ex vivo chicken tissue. **b-d,** Fluorescence emission camera images of the area (in the y-z plane) indicated by the dashed blue square in (a). **b,** Diffuse illumination pattern obtained by focusing into the tissue without wavefront modulation (flat phase display on the SLM). **c,** Illumination pattern resulting from optical phase conjugation of US-tagged light, showing a focus on top of a diffuse background. **d, top,** background images and (d, bottom) background subtracted maps (positive values) obtained by the following techniques: (i) mechanically shifting the sample by 5 μm to disrupt phase conjugation (ii) digitally shifting the phase map by 50 pixels, and (iii) modulating the original phase map by subdividing it into 8 x 16 areas and alternately adding 0 or π phase shift to each area (see Methods).

Background subtraction

As discussed in the Principles, the diffuse background seen in figure 4.2c is to be expected because of the lack of complete control of the entire light field in a phase conjugation experiment. We further observed that the diffuse background was concentrated around the focus, an effect that was also reported by Vellekoop and colleagues when focusing light through a layer of highly scattering zinc oxide particles [29]. As the number of speckles in the focus increases (see Principles), the presence of this background drastically reduces the contrast at the focus and poses a critical challenge to optical focusing using

time-reversal. With the DOPC system, however, the ability to digitally manipulate the phase conjugate field allows for the possibility of playing back a light field that closely mimics the background, thus enabling background subtraction.

Accurate background subtraction requires better understanding of the cause of its spatial localization. One possible explanation of this effect is that it is caused by correlations in the scattering transmission matrix [29]. Thus, like the fidelity of the optical phase conjugate focus, the presence of a concentrated background would depend on the precise alignment of the sample with the phase conjugated beam. Alternatively, the observed background could be caused by the macroscopic concentration of diffuse light around the target area—an effect that would be expected to be more prominent in highly forward-scattering samples such as biological tissues, and that would be invariant to microscopic misalignments of the sample. To isolate the dominant effect contributing to the background in our forward-scattering sample, we displaced the sample by ~ 5 μm and displayed the conjugate of the phase map recorded before the displacement. As can be seen in figure 4.2d, this shift entirely disrupted the focused beam, while the diffuse background was unaffected. After subtraction of this background from the raw image, a focus was revealed at much higher contrast (figure 4.2g). However, mechanical displacement is an impractical method for background subtraction for most applications. Instead, we can digitally alter the recorded phase maps to mimic the diffuse background illumination. We achieved this by two methods: digitally shifting the phase map by 50 pixels (figure 4.2e, h) or dividing phase maps into large sub-regions and phase-shifting every other sub-region by π (figure 4.2f, i – see Methods)—a strategy related to differential background rejection techniques previously used in two-photon microscopy [40,41]. Since digital shifting may introduce undesirable asymmetry to the phase map, the latter method for background subtraction was chosen for all subsequent experiments. We note that a suitable background image could not be obtained by simply displaying a flat phase map on the SLM (as shown in figure 4.2b). Such approach would fail to adapt to different locations of the ultrasound focus and would be unable to compensate for geometrical aberrations in the tissue.

Performing time-reversal and subtracting the background in this manner for each location of the focus, we scanned the position of the ultrasound transducer and confirmed that the optical focus followed the locations of the ultrasound focus. (See Supplementary Movie of *Wang, Y.M., Judkewitz, B., DiMarzio, C.A. & Yang, C. Deep-tissue focal fluorescence imaging with digitally time-reversed ultrasound-encoded light. Nat Commun 3, 928, (2012),* available online.)

Determining the point-spread-function

To measure the point-spread-function and to quantify the resolution of our imaging system, we placed a fluorescent quantum dot filled polyacrylamide bead (< 20 μm in diameter) between two pieces of *ex vivo* chicken breast tissue (figure 4.3a). Figure 4.3b shows an epifluorescence image of this sample. Due to the highly forward scattering nature of our biological sample, the approximate location of the single bead can be inferred. However, tissue scattering results in very strong blurring that would prohibit imaging at high resolution. In contrast, figure 4.3c shows a well-resolved image of the bead collected using time-reversed light. To obtain the image, the ultrasound focus was scanned in the XY plane and an optical focus obtained by phase conjugation was formed at each scan position indicated by the blue dots. Background subtraction by dynamic digital phase map manipulation was performed at every step. Since the bead is smaller than the ultrasound focus, the imaged size of the bead effectively estimates the three-dimensional resolution of the imaging system. The profiles in each dimension (figure 4.3d, e, f corresponding to the X, Y and Z dimensions respectively) were fit by Gaussian point spread functions with widths of 36 ± 3 μm and 52 ± 5 μm (full width at half maximum) respectively in the plane perpendicular to the axis of light propagation, and 657 ± 169 μm along the axis of light propagation (values ± 95% confidence of fit).

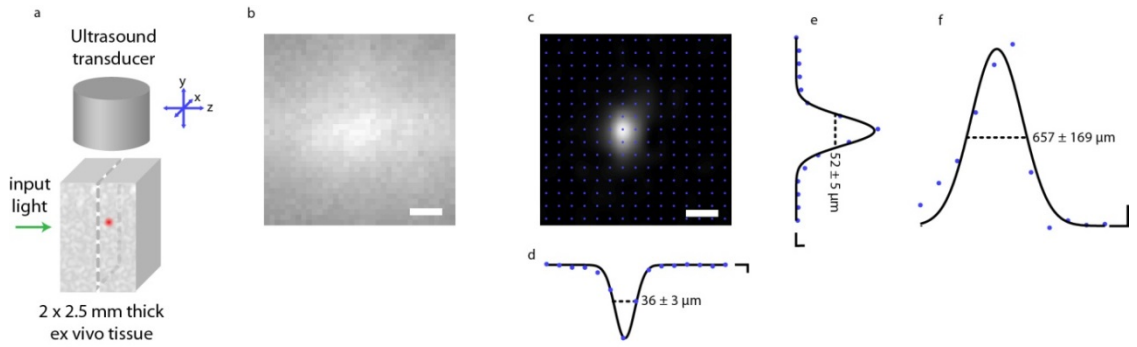

Fig. 4.3 | Determination of point-spread-function. a, Schematic of the setup used for the point-spread-function measurement. A fluorescent bead is embedded between two 2.5 mm thick sections of ex vivo tissue. **b**, Epifluorescence image of the sample, showing very strong blurring due to tissue scattering. **c,** Fluorescence image obtained by scanning the position of the US transducer in X and Y, detecting the fluorescence excited by time-reversed light and using adaptive background cancellation as described in the text. **c.i-iii,** profile of the fluorescent bead in X (i), Y (ii) and Z (iii) direction. Blue dots indicate locations of collected data points. Pixels between data points are interpolated for display using bicubic interpolation.

Fluorescence imaging of complex objects embedded in tissue

We demonstrate the deep tissue imaging capability of our system by raster scanning a known complex feature. We patterned quantum dot features of an abstract "CIT" design in a 500 µm thick polyacrylamide gel patch (a hydrogel that is commonly used for ultrasound phantoms [43]), sandwiched between two pieces of chicken tissue, each ~ 2.5 mm thick (figure 4.4a). Figure 4b shows an epifluorescence image of the features before embedding. Due to tissue scattering, the features cannot be resolved with epifluorescence imaging through the thick tissue (figure 4.4c). In comparison, the "CIT" features are clearly resolved using our method (figure 4.4d).

Fluorescence image of embedded tumor microtissues

We also obtained images of tumor microtissues arranged in a 500 µm thin patch of polyacrylamide gel, sandwiched between two pieces of chicken tissue, each ~ 2.5 mm thick. Figure 4.4e shows an epifluorescence image of the tumors. The tumors embedded between ex vivo tissue are not resolved with epifluorescence imaging (figure 4.4f). In contrast, the tumors imaged with our method are well resolved and the differential fluorescence intensities of the tumors are also reflected in the image (figure 4.4g).

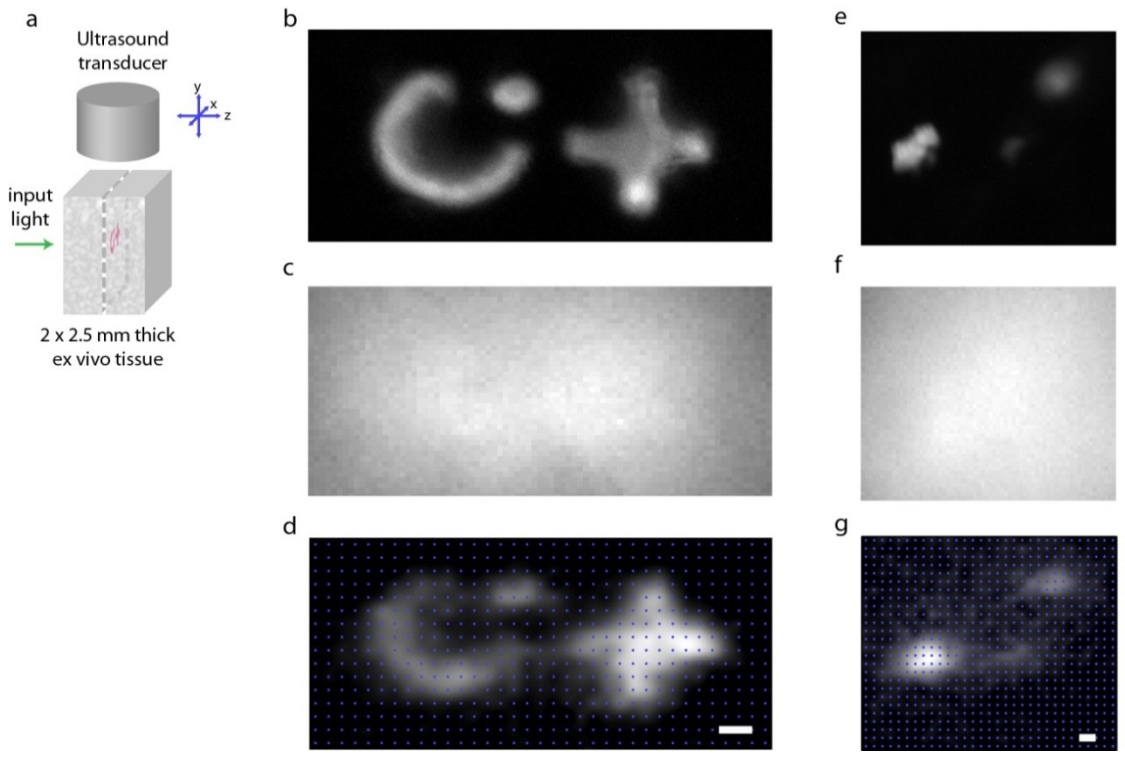

Fig. 4.4 | Fluorescence image of complex objects. a, diagram of sample arrangement **b,** Epifluorescence image of an abstract "CIT" feature. **c,** Epifluorescence image obtained when the sample is placed under 2.5 mm of biological tissue. The features are not resolved. **d,** Raster scanned image of the embedded "CIT" feature obtained using our imaging system. **e,** Epifluorescence image of tumor microtissues. **f**, Epifluorescence image obtained when the sample is placed under 2.5 mm of biological tissue. **g**, Raster scanned image of the embedded tumors obtained using our imaging system. Blue dots indicate locations of collected data points. Pixels between data points are interpolated for display using bicubic interpolation.

4.4 DISCUSSION

Focal fluorescence imaging in biological tissues in highly scattering medium is one of the most important challenges in biomedical optics. In this study, we provide the first demonstration of focal fluorescence imaging in the diffusive regime with time-reversal of ultrasound-tagged light. We implemented a digital optical phase conjugation (DOPC) system with high gain to directly observe the time-reversed optical focus and the accompanying phase-conjugate background. We took advantage of the capabilities of the DOPC to digitally manipulate the phase conjugate map to dynamically estimate and subtract the fluorescence contribution of the phase-conjugate background that would

otherwise obscure the focal fluorescence signal. Using this technique, we characterized the point-spread function of the system as having an anisotropic lateral resolution of 34 μm by 52 μm and an axial resolution of 657 μm. Furthermore, we illustrated the capabilities of our method by successfully imaging fluorescent objects ~ 2.5 mm deep in *ex vivo* tissue.

As confirmed by our results, the imaging resolution perpendicular to the axis of light propagation is determined by the ultrasound focal volume. The system's resolution can therefore be improved by utilizing an ultrasound transducer with a higher central frequency and a higher numerical aperture. However, some expected tradeoffs should be noted. Higher frequency ultrasound is more strongly attenuated in biological tissues [44], thus reducing the practical focusing depth of the ultrasound. Additionally, a smaller modulation volume would further diminish the population of the frequency-shifted light and increase the challenge of detecting a small signal on top of a large background during phase measurement. However, these issues can be addressed by the development of faster, higher dynamic-range cameras, and with advanced filtering methods [45,46]. The point-spread-function along the axis of light propagation is limited by the angular spread of the focused light cone. Since the angular spread is a function of illumination geometry and tissue scattering, the resolution could be improved by using high numerical aperture illumination or—counter-intuitively—by imaging thicker, more scattering samples. Finally, the resolution along the axis of light propagation could further be improved by taking advantage of multiphoton excitation.

We estimate that at the plane of the time-reversed focus, less than 1% of the energy is within the focus. This means that ~ 99% of the remaining energy is spread over the diffuse background, which if uncorrected can obscure focal fluorescence signal. In inhomogeneous fluorescent samples, we showed that dynamic background subtraction effectively uncouples the focal fluorescence signal from that excited by the background. In some applications like photodynamic therapy, where the goal is to deliver more light into the focus, a further increase in peak to background ratio may be desirable. There are two ways to achieve a higher peak to background ratio. First, the number of optical modes (N) intercepted by the

DOPC can be increased by increasing the number of pixels on the SLM. Second, the number of optical modes in the ultrasound focus (M) can be decreased by decreasing the size of the ultrasound focus or increasing the optical wavelength.

Because our method is based on optical time-reversal, it relies on mechanical stability of the sample. The acquisition cycle per pixel should therefore be faster or on the same order of magnitude as the speckle decorrelation of the tissue. This condition is easily met in *ex vivo* experiments: our current pixel acquisition time (6.7 s) was shorter than the decorrelation time of the sample (measured to be ~ 41 s for 5 mm of tissue). For *in vivo* applications, decorrelation times are typically much faster: published values range from millisecond scale [47,48,49] to second scale [50], depending on tissue type and immobilization strategies. For such applications, the pixel acquisition time would have to be reduced accordingly. We anticipate that this will ultimately be possible with the use of faster spatial light modulators [51], and the continuing development of faster, higher dynamic range cameras. In all our experiments, the irradiance of the laser beam at the sample was less than 10 mW/mm^2. The laser power would have to be decreased, or the diameter of the beam increased, to meet clinical safety standards (2 mW/mm^2). Taken together, such improvements would ultimately enable a wide range of *in vivo* applications, including molecular imaging, early cancer diagnosis, photodynamic therapy and targeted excitation of optogenetic tools in deep tissues.

4.5 METHODS

Sample Preparation

Frozen *ex vivo* chicken breast tissue was cut into 2.5 mm thick slices and embedded in 10 % polyacrylamide gel inside an open-top quartz glass sample cuvette with four polished sides (Starna Cells, CA). With 0.5 mm thick chicken breast slices, we found that the scattering coefficient is in agreement with the value of ~ 30/mm reported in ref [31]. Thin slices, rather than thick slices similar to that in our experiments, were used for the measurements because the highly forward scattering nature of biological tissue would result in the underestimation of the scattering coefficient in thick slices [57]. Using the previously

published anisotropy [42] of g = 0.965, we estimated the reduced scattering coefficient as $\mu_s' = \mu_s \cdot (1-g) = 30/mm \cdot (1-0.965) = 1.05/mm$. This is in agreement with the widely referenced approximate value of ~ 1/mm (see e.g. in references [5, 21]).

Polyacrylamide gel (PAA) was polymerized using 4 ml phosphate buffered saline, 1.5 ml Acrylamide, 0.4 ml Bis-acrylamide, 62.5 µl Ammonium persulfate and 25 µl Tetramethylethylenediamine. Polyacrylamide beads containing quantum dots (Qtracker 655 Non-targeted Quantum Dots, Invitrogen), were made using a reverse micelle protocol modified from Beningo and Wang [52] with a starting concentration of 200 nM quantum dots in the aqueous phase. The beads obtained varied in size and were strained through a 40 µm cell strainer (Biologix, USA). The actual sizes of the beads used in all experiments were determined by observation under a fluorescence microscope. The beads were sparsely dispersed in 500 µm thick PAA gel. A gel patch containing one bead was cut out and used as the point-spread-function measurement target.

The "CIT" feature was made by polymerizing clear PAA (500 µm thick) on a SU-8 mold (designed in-house, manufactured by the Stanford Microfluidics Foundry). The patterned depression in the clear PAA gel was then filled with PAA containing quantum dots (Qtracker 705 Non-targeted Quantum Dots, Invitrogen) with a starting concentration of 1 µM in the aqueous phase.

Cancer microtissues, obtained by the hanging-drop technique using HepG2 cells [53], were custom ordered from InSphero AG (Switzerland). The spheroids were fixed with 2% PFA (Sigma-Aldrich, USA), washed with 50 mM borate buffer saline (Thermo Scientific, USA), permeabilized with 0.1% Triton-X 100 (Sigma-Aldrich, USA), and stained with DY-521XL long stokes shift NHS-ester dye (Dyomics, Germany) that binds to the proteins in the cancer microtissues. The concentration of the staining solution was 14 nM. Based on calibration with known fluorophore concentrations, we estimated the resulting stain concentration in the tumor to be ~ 5 µM. The tumor microtissues were arranged and embedded in a 500 µm thick PAA gel.

Measurement of sample scattering coefficient

The scattering coefficient of the chicken tissue was measured interferometrically with a Mach Zehnder interferometer, where one arm is phase modulated by an electro-optic phase modulator. Since only ballistic light will significantly beat with the reference beam (the beatings due to the speckles will average out to zero), the reduction in amplitude of the fringes with and without a sample in the sample beam path can be used to find the scattering coefficient [31]. We also checked this method of measurement against that by propagating the scattering light over ~ 3 meters and measuring the ballistic component. We found that the values are in good agreement.

Setup

All data shown was recorded using a custom-build experimental setup diagrammatically shown in the appendix. A 2.7 W, 532 nm Q-switched laser (Navigator, SpectraPhysics, USA) pulsed at 20 kHz with a pulse width of 7 ns and a coherence length of 7 mm was used as a light source at optical frequency f_0. After passing an optical isolator and a fixed attenuator, it was split into a reference beam and a sample beam. The sample beam was attenuated by a neutral density filter wheel, spatially filtered by a single mode optical fiber (Nufern 460HP, 20 cm length), collimated to a 0.8 mm waist beam and directed into the sample cuvette. The irradiance at the sample is ~ 10 mW/mm^2. We note that this is above the ANSI standards for skin irradiance (2 mW/mm^2).

Inside the sample, a fraction of the light was frequency-shifted to $f_0 + f_{US}$ by an ultrasound transducer (element size: 6.35 mm, focal length: 6 mm; V3330, Olympus NDT, USA) operated at f_{US} = 45 MHz. To achieve maximal resolution along the axis of ultrasound propagation, the transducer was driven with short pulses (pulse length: 1 cycle at 45 MHz, 55 V peak-to-peak) triggered by the laser Q-switch signal at a fixed delay such that the ultrasound pulses coincided with the laser pulses at the ultrasound focus [33] (the trigger delay was jittered by $\pm$ 5.5 ns to minimize the detection of coherent effects between ultrasound-tagged and untagged light). We note here that the ultrasound input power in

this set of experiment is not at maximum recommended input of the transducer (~ 100 V peak-to-peak). Thus, the input power can be potentially increased for higher tagging efficiency.

To scan the ultrasound focus, the transducer was mounted on a three axis computer-controlled micromanipulator (Sutter Instruments, USA). After passing through the sample, the scattered beam was recombined with the reference beam (horizontally polarized), which had also been frequency shifted by f_{us} by an acousto-optic modulator (AFM-502-A1, IntraAction, USA). After passing a horizontally aligned polarizer and another beamsplitter, the combined beams reached the surface of a phase only spatial light modulator (SLM; vis-PLUTO, Holoeye, Germany), carefully aligned (1:1 pixel-to-pixel match) to the image plane of a high dynamic range sCMOS camera (pco.edge, PCO AG, Germany). The lens used to image the SLM onto the sCMOS camera was a commercial compound lens (Nikon Micro-Nikkor 105 mm f/2.8).

Compared to the digital optical phase conjugation system first described by Cui and Yang [32], our improved digital optical phase conjugation (DOPC) system directly imaged SLM pixels onto CCD pixels and thus enabled reliable alignment and day-to-day quality assurance (see below). Since the image had to be reflected by a beamsplitter, we chose a plate beamsplitter (High-Energy Nd:YAG 50/50, Newport Corporation, CA) whose reflective surface faced both SLM and camera, to avoid image aberrations and ensure precise alignment.

SLM curvature compensation

The reliability of digital optical phase conjugation critically depends not only on the precise alignment of SLM and camera, but also on the SLM curvature and reference beam aberrations. Both of these effects can be compensated for digitally by finding a compensation phase map for the SLM that, when displayed, time-reverses the reference beam. Because a time-reversed beam would trace its path back through the spatial filter (the

single mode fiber), the compensation map was optimized by maximizing the power of the light that returned back through the single mode fiber (measured by a photodiode).

Phase recording [*2]

At each scan position, phase recording was achieved in a phase-shifting digital holography setup [37]: the ultrasound pulse was cycled through four phases (0, $\pi/2$, π, $3/2\cdot\pi$). 10-30 frames were recorded (at 30 frames/second) for each phase and averaged, resulting in four intensity maps (I_0, $I_{\pi/2}$, I_π and $I_{3/2\cdot\pi}$), which were used to reconstruct the complex field according to $E = (I_{\pi/2} - I_{3/2\cdot\pi}) + i\cdot(I_0 - I_\pi)$. The phase map was calculated as or $\Phi = \mathrm{Arg}(E)$. To minimize artifacts introduced by slow phase fluctuations of the reference beam, the acquisition of the intensity maps was interleaved by cycling through all four phases for each block of four sequential frames acquired by the sCMOS camera (exposure time: 28 ms, frame rate: 30 Hz). To achieve sufficiently fast cycling and between-frame switching, an arbitrary function generator (AFG 3252, Tektronix, USA) generated two output signals (one 45 MHz sinusoidal cycle with phase-shift of 0 or $\pi/2$), which were each inverted by a RF 180° power splitter (Mini-circuits, USA) to obtain the four phase-shifted signals. A microcontroller board (Arduino, Italy; obtained from SparkFun Electronics, USA) connected to an RF switch (Mini-circuits, USA) was programmed to select the appropriate phase for each frame acquired by the sCMOS camera. Throughout the phase recording, the SLM displayed a flat (all 0) phase map. An acquisition cycle took 6.7 s/pixel. Figure 4.5 shows the complete timing information.

[*2] The optical setup has since been improved to achieve isotropic modulation at higher ultrasound input power. In addition, we did away with the phase jitter. The most updated setup at the point of writing is described in the methods section of chapter 5.

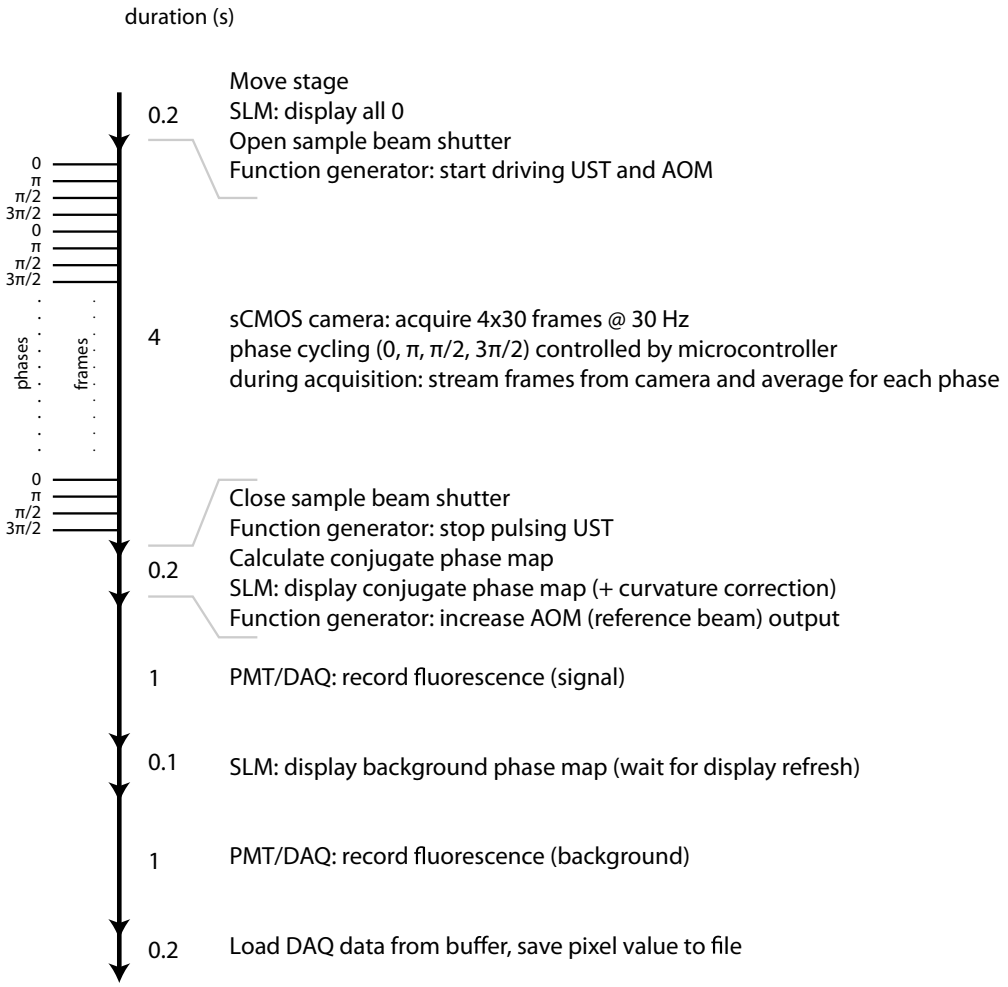

Fig. 4.5 | Timing of acquisition. Abbreviations: Spatial light modulator (SLM), Ultrasound Transducer in sample beam path (UST), Acousto-optic modulator in reference beam path (AOM), Photomultiplier (PMT), Data acquisition device (DAQ). For sequential camera exposures (from frame to frame), the phase is cycled between 0, π, π/2 and 3π/2. Frames corresponding to each respective phase are averaged. The averaged data for each phase shift is used for the calculation of the phase maps. The total duration for acquisition of each data point is 6.7 s.

Since the digital phase shifting holography measurement is based on heterodyne detection, it requires for the sample beam to be coherent with the reference beam. The process of elastic scattering increases the path length of the scattering light. Recalling from the discussion on coherence gating methods in Chapter 1.3, we would see that a short coherence length laser would favor the detection of minimally scattered light. In the case of this experiment, the laser's coherence length is 7 mm. To ensure that the coherence length is

long enough such that it does not limit the detection of scattered photons, we performed a computational analysis using a single layer Monte Carlo simulation [54] of photon transport where a 0.8 mm collimated Gaussian beam was incident on 5 mm cube of sample with scattering properties mimicking that of the 2 x 2.5 mm tissue slabs used in our experiments. Our results showed that 79% of the scattered photons fall within a 7 mm window.[*3]

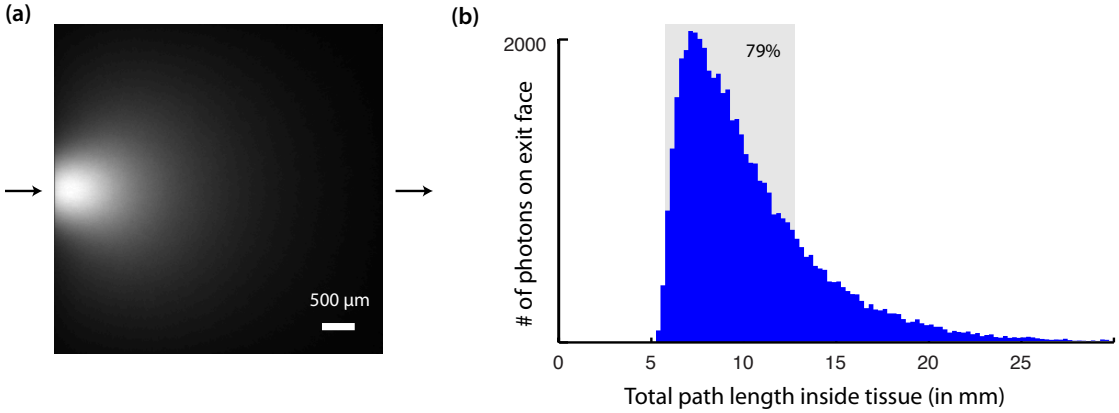

Fig. 4.6 | Effects of coherence length. Only those scattered photons whose path lengths have not spread beyond the laser coherence length (in our case: 7 mm) will be detected by the phase-shifting holography scheme. To confirm that most of the scattered photons fall within this window, we ran a single layer Monte Carlo simulation of photon transport, where a 0.8 mm wide (FWHM) collimated gaussian beam was incident on a (5 mm)^3 cube of tissue, mimicking the two 2.5 mm thick slabs in our experiments (μ_s = 30/mm, g = 0.965). We launched 10^6 photons in this simulation. **a,** shows a 2D projection of the normalized photon flux (summed along the axis going into the page). The path length distribution of the photons leaving the exit face is plotted in **b,**. We find that 79% of the scattered photons fall within a 7 mm window, thus confirming that the majority of the photons will be detected and time-reversed. Scale bar: 500 µm.

A typical ultrasound tagged phase map recorded on the CCD contained N = 8 x 10^4 modes (area of the sensor divided by speckle autocorrelation area). Together with an estimated M of the ultrasound focus of 1 - 2 x 10^3 (estimated by imaging speckles ultrasound-modulated after passing through one layer of 2.5 mm chicken breast) we obtained a theoretical upper bound for the peak to background ratio of ~ 60 (Eq. 4.4). We note that in practice we will have to consider additionally the fact that we are only

*[3] The Monte Carlo simulation and analysis is performed solely by Benjamin Judkewitz, but is included here for completeness.

controlling one polarization state (factor of 2), the alignment quality of the DOPC and the experimental error of the speckle size estimation due to uncertainty of the imaging plane.

Detection of fluorescence excitation by time-reversed light

The time-reversed beam was obtained by reflecting the blank reference beam off the spatial light modulator displaying the measured phase conjugate map. The backscattered fluorescence excited by the time-reversed optical focus was reflected off a dichroic mirror and detected by a single channel PMT fitted with the appropriate bandpass filters (Semrock 650-40, 710-40 or 675-67, for Qtracker 655, Qtracker 705 or DY-521XL long stokes shift NHS-ester dye respectively).

Quality assurance of digital optical phase conjugation

Because of the dependence of our system on precise alignment, mechanical stability and low drift, we included a parallel sample beam path to asses and assure the performance of our setup on a day-to-day basis. Consisting of ground glass diffusers and an additional observing camera, it was analogous to the setups previously used by our group to demonstrate turbidity suppression by phase conjugation [31].

Speckle decorrelation time

With the sample beam turned on, we acquired images of the speckle field on the sCMOS camera at a rate of 1 fps for 180 seconds. We measured the correlation of the first frame with each subsequent frame and defined the decorrelation time as the time after which the correlation fell below $1 - \frac{1}{e}$.

Phase jitter in acoustic wave

Our technique relies on the detection of 45 MHz ultrasound frequency-shifted light in the presence of a large background of non-shifted light. While the reference beam (equally frequency-shifted by 45 MHz) interferes with US-tagged light, interference of the reference beam with the non-shifted light occurs at a beating frequency of 45 MHz (cycle time: 22.2 ns). This beating usually averages out during the much longer integration time of the CMOS

camera. But if the illumination is pulsed, the pulse duration approaches one beating cycle or less and the phase of the beating is locked to the laser trigger output, the interference between the non-shifted beam and the shifted beam may nevertheless be detected. This would not be desirable in our case, since a small phase drift between the non-shifted beam and the reference beam would lead to an added artificial signal on the phase map we measure. To ensure that such coherent effects between the non-shifted beam and the frequency-shifted beam are not detected on our camera, we randomly alternate between two trigger delays of a time difference that corresponds to half a 45 MHz beating cycle (11.1 ns or $\pm$ 5.5 ns). A microcontroller randomly chooses a jitter for each laser sync output pulse (at a rate of 20 kHz) and the jitter is added to the trigger delay of ultrasound transducer as well as reference beam AOM. The relative phase between ultrasound-shifted light and the reference beam therefore remains unaffected.

APPENDIX: FULL SETUP DIAGRAM

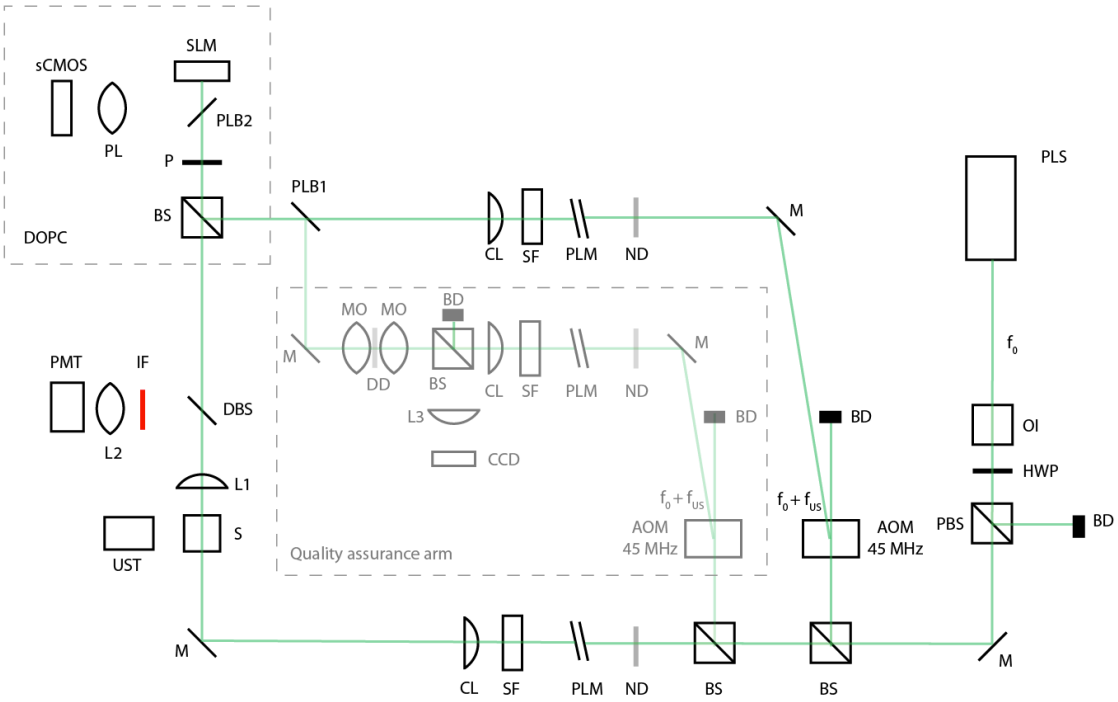

Fig. 4.A | Setup diagram. Abbreviations: Pulsed laser source (PLS), Optical Isolator (OI), Half-wave plate (HWP), Polarizing beamsplitter (PBS), Beam dump (BD), Mirror (M), 50/50 cube beamsplitter (BS), Acousto-optic modulator (AOM), Neutral density filter-wheel (ND), Path length matching arm (PLM), Single-mode fiber acting as spatial filter (SF), Collimating lens (CL), Sample (S), Ultrasound transducer (UST), 50 mm planoconvex lens (L1), Dichroic beamsplitter (DBS), Interference filter (IF), 25 mm planoconvex lens (L2), Photomultiplier tube (PMT), Polarizer (P), 90/10 plate beamsplitter (PLB1), Digital optical phase conjugation setup (DOPC), 50/50 plate beamsplitter (PLB2), Photography compound lens (PL), sCMOS camera (sCMOS), Spatial light modulator (SLM), 300 mm plano-convex lens (L3), Microscope objective (MO), Diffuser disk (DD).

REFERENCES

1. Denk, W., Strickler, J. & Webb, W. Two-photon laser scanning fluorescence microscopy. *Science* 248, 73-76 (1990).
2. Helmchen, F. & Denk, W. Deep tissue two-photon microscopy. *Nat Meth* 2, 932-940 (2005).
3. Minsky, M. Microscopy Apparatus. (USA, 1961).
4. Huang, D., *et al.* Optical coherence tomography. *Science* 254, 1178-1181 (1991).
5. Ntziachristos, V. Going deeper than microscopy: the optical imaging frontier in biology. *Nat Meth* 7, 603-614 (2010).
6. Ntziachristos, V., Ripoll, J., Wang, L.V. & Weissleder, R. Looking and listening to light: the evolution of whole-body photonic imaging. *Nat Biotech* 23, 313-320 (2005).
7. Lichtman, J.W. & Conchello, J.-A. Fluorescence microscopy. *Nat Meth* 2, 910-919 (2005).
8. Vellekoop, I.M., LagendijkA & Mosk, A.P. Exploiting disorder for perfect focusing. *Nat Photon* 4, 320-322 (2010).
9. van Putten, E.G., *et al.* Scattering Lens Resolves Sub-100 nm Structures with Visible Light. *Physical Review Letters* 106, 193905 (2011).
10. Hsieh, C.L., Pu, Y., Grange, R. & Psaltis, D. Digital phase conjugation of second harmonic radiation emitted by nanoparticles in turbid media. *Optics Express* 18, 12283-12290.
11. Popoff, S., Lerosey, G., Fink, M., Boccara, A.C. & Gigan, S. Image transmission through an opaque material. *Nat Commun* 1, 81 (2010).
12. Katz, O., Small, E., Bromberg, Y. & Silberberg, Y. Focusing and compression of ultrashort pulses through scattering media. *Nat Photon* 5, 372-377 (2011).
13. Mudry, E., Le Moal, E., Ferrand, P., Chaumet, P.C. & Sentenac, A. Isotropic Diffraction-Limited Focusing Using a Single Objective Lens. *Physical Review Letters* 105, 203903 (2010).
14. McCabe, D.J., *et al.* Spatio-temporal focusing of an ultrafast pulse through a multiply scattering medium. *Nat Commun* 2, 447 (2011).
15. Katz, O., Small, E., Bromberg, Y. & Silberberg, Y. Focusing and compression of ultrashort pulses through scattering media. *Nat Photonics* 5, 372-377 (2011).
16. Yaqoob, Z., Psaltis, D., Feld, M.S. & Yang, C.H. Optical phase conjugation for turbidity suppression in biological samples. *Nat Photonics* 2, 110-115 (2008).
17. Leith, E.N. & Upatniek.J. Holographic Imagery Through Diffusing Media. *Journal of the Optical Society of America* 56, 523-& (1966).
18. Goodman, J.W., Huntley, W.H., Jackson, D.W. & Lehmann, M. Wavefront-Reconstruction Imaging Through Random Media. *Applied Physics Letters* 8, 311-& (1966).
19. Davies, R. & Kasper, M. Adaptive Optics for Astronomy. *Annual Review of Astronomy and Astrophysics* 50, 1-47 (2012).

20. Zawadzki, R.J., *et al.* Adaptive-optics optical coherence tomography for high-resolution and high-speed 3D retinal in vivo imaging. *Optics Express* 13, 8532-8546 (2005).
21. Xu, X., Liu, H. & Wang, L.V. Time-reversed ultrasonically encoded optical focusing into scattering media. *Nat Photonics* 5, 154-157 (2011).
22. Yariv, A. Phase conjugate optics and real-time holography. *Quantum Electronics, IEEE Journal of* 14, 650-660 (1978).
23. Mahan, G.D., Engler, W.E., Tiemann, J.J. & Uzgiris, E. Ultrasonic Tagging of Light: Theory. *Proceedings of the National Academy of Sciences of the United States of America* 95, 14015-14019 (1998).
24. Liu, H., Xu, X., Lai, P. & Wang, L.V. Time-reversed ultrasonically encoded optical focusing into tissue-mimicking media with thickness up to 70 mean free paths. *Journal of biomedical optics* 16, 086009 (2011).
25. Lai, P., Xu, X., Liu, H., Suzuki, Y. & Wang, L.V. Reflection-mode time-reversed ultrasonically encoded optical focusing into turbid media. *Journal of biomedical optics* 16, 080505 (2011).
26. Kothapalli, S.R. & Wang, L.H.V. Ultrasound-modulated optical microscopy. *Journal of biomedical optics* 13(2008).
27. Feinberg, J., Heiman, D., Tanguay, A.R. & Hellwarth, R.W. Photorefractive effects and light-induced charge migration in barium titanate. *Journal of Applied Physics* 51, 1297-1305 (1980).
28. Gunter, P. & Huignard, J.P. *Photorefractive Materials And Their Applications. 1 Basic Effects*, (Springer, 2006).
29. Vellekoop, I.M. & Mosk, A.P. Universal Optimal Transmission of Light Through Disordered Materials. *Physical Review Letters* 101, 120601 (2008).
30. Gu, C. & Yeh, P.C. Partial phase conjugation, fidelity, and reciprocity. *Optics Communications* 107, 353-357 (1994).
31. McDowell, E.J., *et al.* Turbidity suppression from the ballistic to the diffusive regime in biological tissues using optical phase conjugation. *Journal of biomedical optics* 15, 025004 (2010).
32. Cui, M. & Yang, C.H. Implementation of a digital optical phase conjugation system and its application to study the robustness of turbidity suppression by phase conjugation. *Optics Express* 18, 3444-3455 (2010).
33. Atlan, M., Forget, B.C., Ramaz, F., Boccara, A.C. & Gross, M. Pulsed acousto-optic imaging in dynamic scattering media with heterodyne parallel speckle detection. *Optics Letters* 30, 1360-1362 (2005).
34. Feinberg, J. & Hellwarth, R.W. Phase-conjugating mirror with continuous-wave gain. *Optics Letters* 5, 519-521 (1980).
35. Lanzerotti, M.Y., Schirmer, R.W. & Gaeta, A.L. High-reflectivity, wide-bandwidth optical phase conjugation via four-wave mixing in potassium vapor. *Applied Physics Letters* 69, 1199-1201 (1996).

36. Tschudi, T., *et al.* Image amplification by two- and four-wave mixing in BaTiO3 photorefractive crystals. *Quantum Electronics, IEEE Journal of* 22, 1493-1502 (1986).
37. Yamaguchi, I. & Zhang, T. Phase-shifting digital holography. *Opt. Lett.* 22, 1268-1270 (1997).
38. Vellekoop, I.M. Controlling the propagation of light in disordered scattering media. *University of Twente* Thesis, 1-142 (2008).
39. Vellekoop, I.M. & Mosk, A.P. Focusing coherent light through opaque strongly scattering media. *Optics Letters* 32, 2309-2311 (2007).
40. Leray, A. & Mertz, J. Rejection of two-photon fluorescence background in thick tissue by differential aberration imaging. *Optics Express* 14, 10565-10573 (2006).
41. Leray, A., Lillis, K. & Mertz, J. Enhanced background rejection in thick tissue with differential-aberration two-photon microscopy. *Biophysical Journal* 94, 1449-1458 (2008).
42. Cheong, W.F., Prahl, S.A. & Welch, A.J. A Review of the Optical Properties of Biological Tissues. *Ieee Journal of Quantum Electronics* 26, 2166-2185 (1990).
43. Zell, K., Sperl, J.I., Vogel, M.W., Niessner, R. & Haisch, C. Acoustical properties of selected tissue phantom materials for ultrasound imaging. *Physics in Medicine and Biology* 52, N475-N484 (2007).
44. Goss, S.A., Frizzell, L.A. & Dunn, F. Ultrasonic absorption and attenuation in mammalian tissues. *Ultrasound in Medicine & Biology* 5, 181-186 (1979).
45. Li, Y., Hemmer, P., Kim, C., Zhang, H. & Wang, L.V. Detection of ultrasound-modulated diffuse photons using spectral-hole burning. *Optics Express* 16, 14862-14874 (2008).
46. Gross, M., *et al.* Detection of the tagged or untagged photons in acousto-optic imaging of thick highly scattering media by photorefractive adaptive holography. *Eur Phys J E* 28, 173-182 (2009).
47. Draijer, M., Hondebrink, E., van Leeuwen, T. & Steenbergen, W. Review of laser speckle contrast techniques for visualizing tissue perfusion. *Lasers in Medical Science* 24, 639-651 (2009).
48. Hajjarian, Z., Xi, J., Jaffer, F.A., Tearney, G.J. & Nadkarni, S.K. Intravascular laser speckle imaging catheter for the mechanical evaluation of the arterial wall. *Journal of biomedical optics* 16(2011).
49. Lev, A. & Sfez, B. In vivo demonstration of the ultrasound-modulated light technique. *Journal of the Optical Society of America. A, Optics, image science, and vision* 20, 2347-2354 (2003).
50. Cui, M., McDowell, E.J. & Yang, C. An in vivo study of turbidity suppression by optical phase conjugation (TSOPC) on rabbit ear. *Optics Express* 18, 25-30 (2010).
51. Conkey, D.B., Caravaca-Aguirre, A.M. & Piestun, R. High-speed scattering medium characterization with application to focusing light through turbid media. *Optics Express* 20, 1733-1740 (2012).
52. Beningo, K.A. & Wang, Y.L. Fc-receptor-mediated phagocytosis is regulated by mechanical properties of the target. *Journal of Cell Science* 115, 849-856 (2002).

53. Kelm, J.M., Timmins, N.E., Brown, C.J., Fussenegger, M. & Nielsen, L.K. Method for generation of homogeneous multicellular tumor spheroids applicable to a wide variety of cell types. *Biotechnology and Bioengineering* 83, 173-180 (2003).
54. Wang, L.V. & Wu, H.-I. Biomedical Optics: Principles and Imaging. (Wiley, 2007).
55. Fowler, K. A., Hotchkiss, F. H. C., Yamartino, T. V., & Nelligan, T. *Important characteristics of sound fields of ultrasonic transducers* Olympus NDT website: http://cache.olympus-ims.com/downloads/storage/276824584/ImportantCharacteristicsofSoundFieldsofUltrasonic_2013.pdf?__gda__=1361688369_d1a2ac47b8f588feeef37cc2e0b46ed5
56. Zell, K., Sperl, J.I., Vogel, M.W., Niessner, R. & Haisch, C. Acoustical properties of selected tissue phantom materials for ultrasound imaging. *Physics in Medicine and Biology* 52, N475-N484, (2007).
57. Flock, S.T., Wilson, B.C. & Patterson, M.S. Total attenuation coefficients and scattering phase functions of tissues and phantom materials at 633 nm. *Medical Physics* 14, 835-841, (1987).

Chapter 5
Speckle-scale focusing in the diffusive regime with time-reversal of variance-encoded light (TROVE)

This chapter is reproduced with some adaptations from the manuscript: Judkewitz, B., Wang, Y.M.*, Horstmeyer, R., Mathy, A. & Yang, C. Speckle-scale focusing in the diffusive regime with time-reversal of variance-encoded light (TROVE). Nature Photonics 7, 300-305, (2013). The contributions of the authors are as follows: BJ and YMW contributed equally to this work. BJ conceived the idea. BJ and YMW developed the idea, with the help of RH, AM and CY. BJ and YMW designed the experiment, built the setup, collected data, performed the simulation and data analysis, and wrote the manuscript. RH contributed to the manuscript and to the simulation results. RH and AM contributed to analysis and mathematical derivation. CY supervised the project and contributed to the manuscript.*

Focusing of light in the diffusive regime inside scattering media has long been considered impossible. Recently, this limitation has been overcome with time reversal of ultrasound-encoded light (TRUE), but the resolution of this approach is fundamentally limited by the large number of optical modes within the ultrasound focus. Here, we introduce a new approach, time reversal of variance-encoded light (TROVE), which demixes these spatial modes by variance-encoding to break the resolution barrier imposed by the ultrasound. By encoding individual spatial modes inside the scattering sample with unique variances, we effectively uncouple the system resolution from the size of the ultrasound focus. This enables us to demonstrate optical focusing and imaging with diffuse light at unprecedented, speckle-scale lateral resolution of ~5 μm.

5.1 INTRODUCTION

Scattering of light by inhomogeneous media poses a fundamental challenge to numerous applications in astronomy, biomedical imaging and colloidal optics. For a long time, scattered light has been viewed as a source of noise and many efforts have been made to get rid of them (see chapter 1), such that the only the ballistic light is detected and measured. However, in strong scattering media, the ballistic component approaches zero. Thus, light focusing into diffusive samples have long been considered futile.

In chapters 1 and 3, we discussed various recent developments in the field of wavefront shaping that have changed this view. As introduced before, although a swavefront that has been scattered seem randomized, there is in fact a linear mapping between the optical modes in the input wavefront and the optical modes in the output wavefront. This mapping can be fully described by a scattering transmission matrix (chapters 1, 2 and 3). These linear, deterministic and time-symmetric properties of scattering [1] have been harnessed for focusing and image transfer across complex samples by iterative wavefront optimization [2-7], time reversal [8,9] or directly measuring and inverting the transmission matrix [10-14].

However, a yet remaining limitation to these significant advances is that access to both sides of the medium is required. Thus, in cases where a focus is desired between or inside highly scattering medium, beacons or so-called "guide-stars" are required in the target plane. We discussed in the previous chapters the implementation of fluorescent particles [15]and second-harmonic particles [16] as guide-stars and identified that one limitation is that focusing is limited to the vicinity of the particles. In the previous chapter, we introduced a method termed time reversal of ultrasound-encoded light (TRUE) [17-21], shows much promise for non-invasive imaging by taking advantage of virtual acousto-optic beacons. In this approach, an ultrasound focus frequency-shifts the scattered optical wavefront within a scattering sample thus creating a source of frequency-shifted light. Scattered, frequency-shifted light emanating from this source is recorded outside the tissue and time-reversed by optical phase conjugation to converge back onto the location of the ultrasound focus.

Despite its ability to focus inside scattering samples at unprecedented depths, the resolution of TRUE imaging is fundamentally limited by the size of the ultrasound beacon, which is at least an order of magnitude larger (tens of micrometres at best) than the optical speckle size (micrometre-scale).

Here, we propose a way to overcome this resolution barrier imposed by the size of the beacon by time reversal of variance-encoded light (TROVE). TROVE takes advantage of a spatially unique variance structure imposed by spatially overlapping acoustic foci to encode the spatial location of individual optical speckles within the ultrasound focus. Upon optical time reversal of computationally decoded modes, we achieve focusing at the scale of single optical speckles with diffuse light.

5.2 PRINCIPLES

TRUE and TROVE

Here we explain the resolution limitation of TRUE imaging and how we can overcome this limitation by variance encoding in TROVE. To do so, we conceptually divide a scattering medium into two sections: one, through which the input light passes before reaching the ultrasound focus and a second, through which the ultrasound-shifted light passes on the way out of the medium. This division can be made without loss of generality for different illumination and recording geometries (for example in reflection geometries [18]).

In TRUE (illustrated in figure 1a), an input wavefront is randomized as it passes through the first half of the sample, resulting in a speckled wavefront $\boldsymbol{b}$ at the ultrasound focus. Part of this wavefront is modulated via the acousto-optic effect, resulting in a frequency-shifted optical field $\boldsymbol{b'}$. Because the ultrasound focus is much larger than the optical wavelength, this field contains many optical modes – typically hundreds to thousands of optical speckles for a 30 to 40 μm wide ultrasound focus. This number largely depends on the scattering properties of the sample, the transmission geometry and the wavelength of the illuminating optical source. Since we will eventually only measure and

phase conjugate the frequency-shifted light, we need only consider the frequency-shifted optical field $\boldsymbol{b'}$.

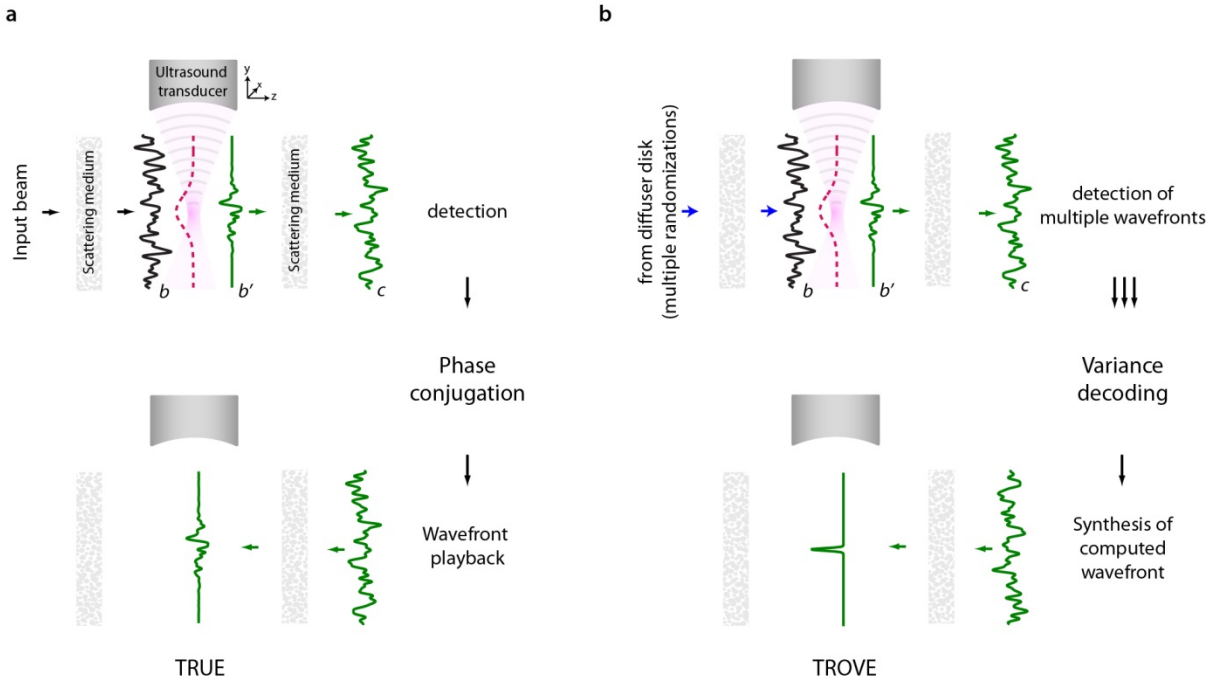

Fig. 5.1 | Schematic comparison of TRUE and TROVE focusing. a, In TRUE focusing, an input beam is randomized as it passes through the scattering medium. The speckled field b reaching an ultrasound focus is then frequency-shifted, but only at the location of the Gaussian-shaped ultrasound focus. The frequency-shifted field b′ continues to propagate through the sample, undergoing another round of scattering before leaving tissue. In TRUE imaging, this wavefront is detected, phase conjugated and played back. This leads to a multimode optical focus within the tissue at the former location of the ultrasound focus. The resolution of this focus is limited by the size of the ultrasound. **b,** TROVE imaging overcomes this resolution limitation by employing multiple presentations of randomized input wavefronts and a statistical decoding procedure that enables demixing of individual optical modes. Once these modes are computed, they are displayed on a digital spatial light modulator (SLM). After propagation back through the sample, they form speckle-sized optical foci – thereby significantly improving the resolution over TRUE imaging.

Next, the frequency-shifted components propagate through the second half of the scattering medium before leaving it as the output field $\boldsymbol{c}$. This output field is measured and subsequently time-reversed (phase conjugated), resulting in an approximation to the conjugate of the field $\boldsymbol{b'}$ at the ultrasound focal plane (the recovery of the multi-modal focus at the location of the ultrasound plus background, as discussed in chapter 3 with reference to [2]). Thus, the limited resolution of TRUE is a result of the fact that all optical modes

passing through the ultrasound focus are collectively detected outside the sample as a linear addition of the contributions of many component fields that can be attributed to each input optical mode (see chapter 1 on introduction to transmission matrices). This detected wavefront is then time-reversed to form a multimode focus at the location of the ultrasound focus.

To achieve micrometer-scale optical focusing, we would instead have to isolate the wavefront component originating from a single optical mode. The TROVE approach addresses this challenge by uniquely encoding the spatial locations of the frequency-shifted optical speckles within the frequency-shifted speckle field with a variance structure imposed by spatially shifted ultrasound foci. Using this variance structure, we computationally decode the wavefront component that corresponds to the desired speckle location.

Experimental illustration of TROVE concept

To illustrate how this is achieved, we sought to measure and characterize the frequency-shifted field $\boldsymbol{b'}$ at the ultrasound focus. We did so by constructing a sample consisting of an agarose-filled glass cuvette with a strongly scattering medium on the side of the input light (figure 5.2a). We confirmed that no detectable ballistic component reached the ultrasound plane. In the absence of a second scattering medium, we imaged the frequency-shifted wavefront at the ultrasound plane via digital phase-shifting holography (see Methods). Figure 5.2b shows a typical speckle pattern at the ultrasound plane. As expected, it had an envelope defined by the ultrasound focus. When we changed the input wavefront reaching the sample by rotating a diffuser disk in the path of the input beam, the measured speckle field changed but the amplitude envelope remained the same. Therefore, the average amplitude of the complex optical speckle field across many presentations of a random input wavefront assumed the shape of the ultrasound focus (Figure 5.2c). The variance of the field across many presentations is proportional to the square of this envelope. Thus, optical modes experienced different levels of variance depending on their spatial location.

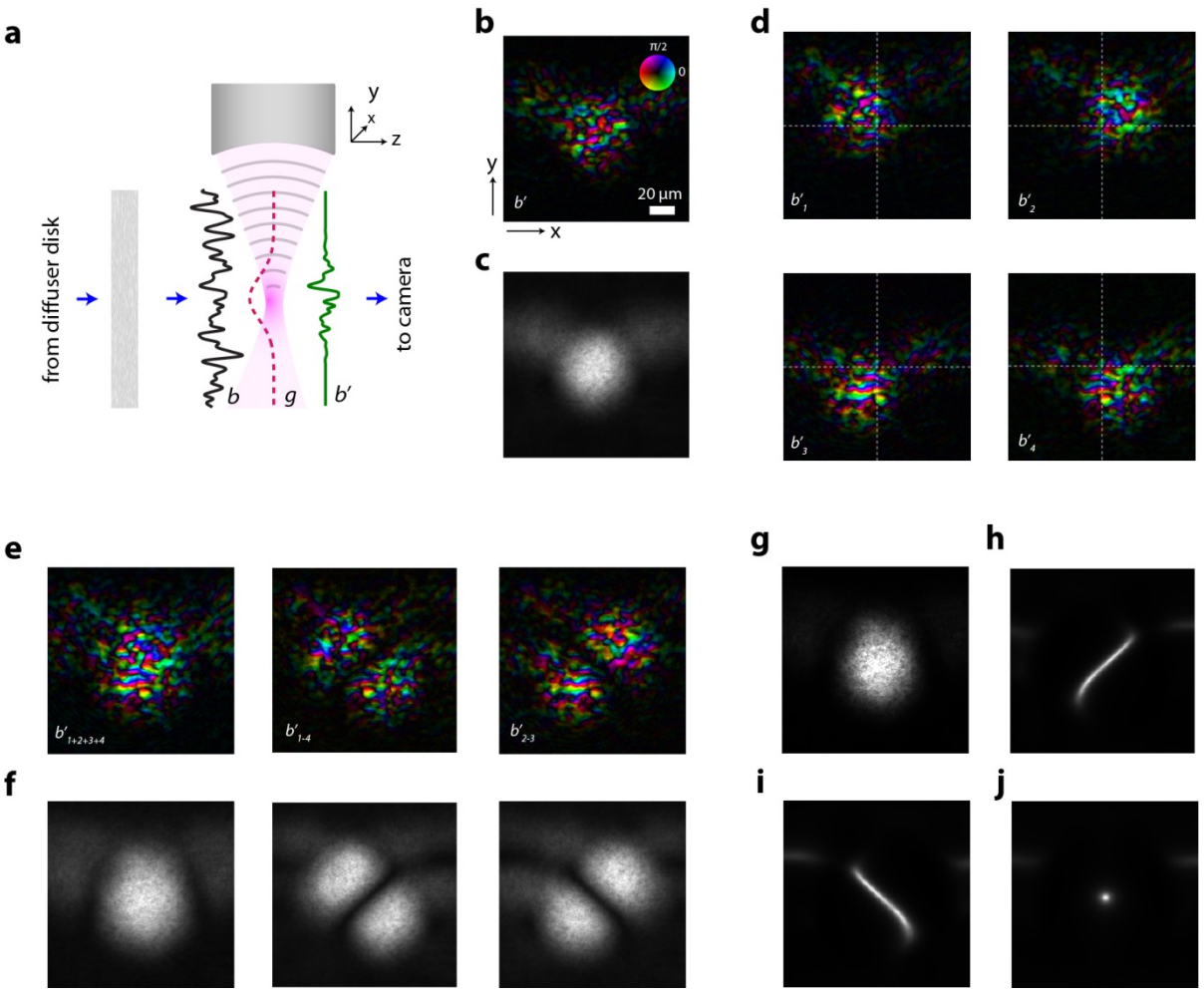

Fig. 5.2 | Characterization of frequency-shifted wavefronts at the ultrasound plane. a, Schematic of the recording setup in the conceptual demonstration of the TROVE concept., in which the second scattering medium is absent to allow optical access to the field *b′*, from the right. **b,** Typical frequency-shifted speckle field at the plane of the ultrasound focus. Colour represents phase and luminance represents normalized amplitude. **c,** Average amplitude of the frequency-shifted optical speckle field, over 1000 realizations. **d,** Complex ultrasound frequency-shifted field at the plane of the ultrasound focus for four shifted locations of the ultrasound. Readers will notice that the underlying speckle pattern is the same, but the ultrasound-modulated envelopes are shifted. **e,** Complex sum and pairwise differences of the fields in panel a, respectively**. f,** Average amplitudes of the fields shown in panel e, over 1000 realizations. **g,** Variance across realizations of $b_{1+2+3+4}$ (square of data shown in fig. f) **h,** Variance of $b_{1+2+3+4}$, divided by variance of b_{1-4}. **i**, Variance of $b_{1+2+3+4}$, divided by variance of b_{2-3}. **j,** Variance of $b_{1+2+3+4}$, divided by the sum of variances of b_{1-4} and b_{2-3}. Scale bar: 20 μm.

Because the Gaussian-shaped ultrasound focus is symmetric, more than one location in the ultrasound plane will experience the same level of variance. In addition, because the Gaussian function has a rather gentle peak, in the presence of noise, optical speckles neighboring to the one at the peak of the ultrasound focus can have similar variances to that

at the peak. To unambiguously encode individual optical modes, we used four overlapping ultrasound foci arranged in a square grid. Figure 5.2d shows the representative complex maps of the frequency-shifted fields $\boldsymbol{b'}_1$, $\boldsymbol{b'}_2$, $\boldsymbol{b'}_3$, $\boldsymbol{b'}_4$. Figure 5.2e shows the complex sum of the four shifted fields ($\boldsymbol{b'}_{1+2+3+4}$) and the pairwise difference between the diagonally shifted fields ($\boldsymbol{b'}_{1-4}$ and $\boldsymbol{b'}_{2-3}$ respectively). By moving the diffuser and repeating the measurement for 1000 random presentations of the input wavefront, we obtained an average amplitude map of the frequency-shifted optical field (figure 5.2f). It is important to note that, in each random presentation, the data for the four foci is recorded for the same diffuser position.

As shown in figure 5.2f, the average amplitude along $\boldsymbol{b'}_{1-4}$ and $\boldsymbol{b'}_{2-3}$, yielded a null zone, which was absent in the average amplitude of $\boldsymbol{b'}_{1+2+3+4}$. This null zone in the average of speckle images was also apparent in their variance across realisations. As can be seen in figure 5.2j, the ratio between the variance of $\boldsymbol{b'}_{1+2+3+4}$ (figure 5.2g) and the sum of variances of $\boldsymbol{b'}_{1-4}$ and $\boldsymbol{b'}_{2-3}$ had a peak at the intersection of the four Gaussians, uniquely defining that point.

While this experimental demonstration illustrates that we indeed get a null point at the ultrasound plane, we need to keep in mind that our ultimate goal is to accomplish focusing between scattering media. Consequently, we would not have access to speckle data at the ultrasound plane. Instead of analysing data at the ultrasound plane, we would only be able to record and analyse wavefronts at the output plane. Since the variance structure of optical modes is preserved as they are transmitted through the scattering medium (see Supplement), we can also find the desired optical modes in the data set recorded at the output plane. We do so by searching for a vector $\boldsymbol{v}$, along which the variance of the measured data $\boldsymbol{c}_{1-4}$ and $\boldsymbol{c}_{2-3}$ is minimal and the variance of the sum $\boldsymbol{c}_{1+2+3+4}$ is maximal. Mathematically, we define the vector $\boldsymbol{v}$ as the one that maximizes the ratio between the variance of $\boldsymbol{c}_{1+2+3+4}$ and the sum of the variances of $\boldsymbol{c}_{1-4}$ and $\boldsymbol{c}_{2-3}$. The computational procedure for finding the vector $\boldsymbol{v}$ can be found in the methods. The resultant vector $\boldsymbol{v}$ is equivalent to the output field that would originate from a single optical mode at the location of the intersection of the four acoustic foci. By displaying the phase conjugate of $\boldsymbol{v}$ on a digital

spatial light modulator (SLM) and propagating it back through the scattering medium, we expect to obtain a high-resolution optical focus at the location of the intersection of the shifted acoustic foci.

Although we assumed (and measured) that the ultrasound foci are Gaussian-shaped, it is worth noting that the validity and performance of the TROVE method does not hinge upon the exact shape of the ultrasound focus, as long as shifted foci intersect such that the ratio between the variance of $\boldsymbol{b'}_{1+2+3+4}$, divided by the sum of variances of $\boldsymbol{b'}_{1-4}$ and $\boldsymbol{b'}_{2-3}$ presents a sharp null point. Thus, this method would be applicable to other ultrasound focus shapes (even with mild aberrations), as long as they satisfy this condition. We note, however, that both the TRUE and TROVE techniques rest on the assumption that the samples induce only mild ultrasound aberrations.

5.3 RESULTS

Direct visualization of TROVE focus

To demonstrate that the TROVE approach can be used to focus inside a scattering sample, we created a sample consisting of a glass cuvette flanked on both sides by strong diffusers that do not transmit a detectable ballistic component (see "Methods" section and figure 5.3a). We filled the cuvette with agarose containing a thin quantum dot sheet, so the TROVE focus could be observed via fluorescence excitation. Without any wavefront manipulation, we observed that light was highly diffused and failed to form a focus within the sample (figure 5.3b). Using the TRUE focusing approach and digitally phase conjugating an unprocessed phase map from a single realization, we observed a focus with a full width half maximum of 31.2 μm, similar to the size of the ultrasound focus (~ 32 μm in agar, where the speed of sound is ~1500 m/s [22]) (figure 5.3c & e). When implementing the TROVE framework, we achieved a focus size of 5.2 μm (figure 5.3d & f), which is close to the optical speckle size in our sample (~5 μm FWHM of the intensity autocorrelation). Thus, the TROVE method yielded a six-fold improvement over the TRUE focusing approach, which was close to the achievable optical limit imposed by the speckle size. A direct consequence

of the reduction of optical modes in the TROVE focus as compared to the TRUE focus was an increase in the peak signal intensity of the time-reversed focus (as discussed in chapter 3 and in reference [23]). We observed in our experiments that the peak signal intensity with TROVE increased by a factor of 20 compared to TRUE.

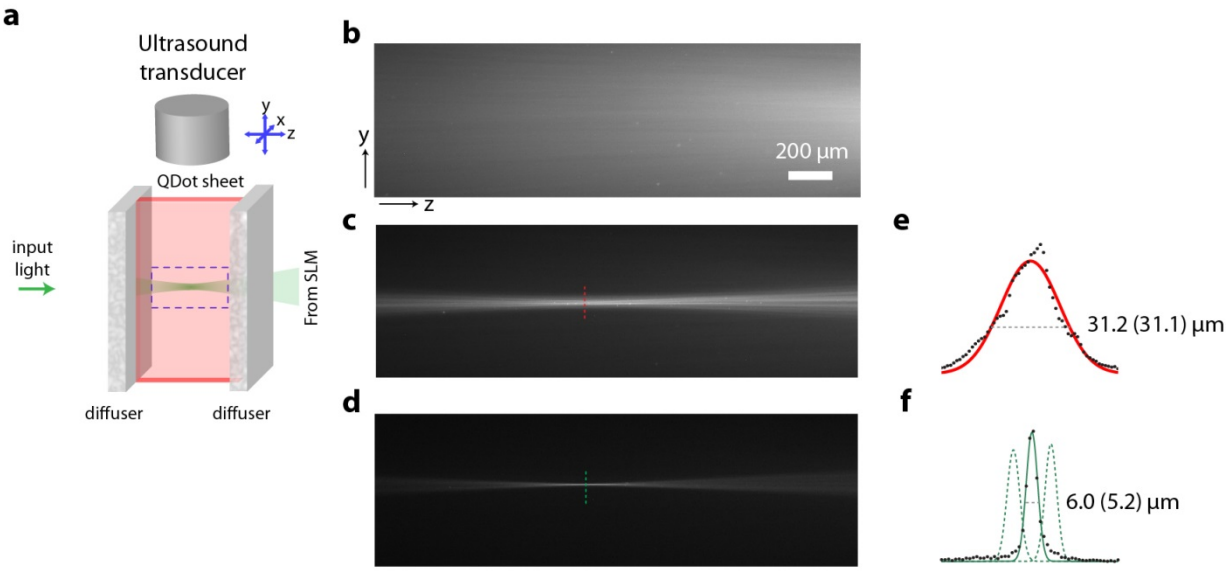

Fig. 5.3 | Visualization of speckle-scale optical focusing. a, Schematic of the experimental setup, consisting of a thin sheet of quantum dots between two strong diffusers. **b - d,** Fluorescence emission images of the area in y-z plane indicated by dotted square in **a**. **b,** Diffuse illumination observed without wavefront manipulation (flat phase display on the SLM). **c,** TRUE focusing results in an optical focus the size of the ultrasound focus. **d,** With TROVE, an optical focus the size of an optical speckle is achieved. **e,** Profile of the TRUE focus width. **f,** Profile of the TROVE focus width (the number in brackets indicates the calculated resolution after deconvolving the profile with the resolution of the camera imaging the dotted square in **a**). Black dots are data points. The dotted lines represent profiles of TROVE foci scanned in y (scan locations separated by 10 µm). Scale bar for b-d: 200 µm

---

A straightforward way to shift the TROVE focus, or access other optical modes at different positions, would be to move the location of the ultrasound foci. This would entail repeating the entire measurement for 1000 diffuser positions. However, the TROVE strategy allows access to multiple optical modes within the ultrasound focus without the need for further acquisition of data. We note that the location of the TROVE focus is entirely determined by the point at which the shifted ultrasound foci intersect (see above). Thus, by

numerically weighing the output wavefronts with respect to each other during post-processing, we can virtually move the point of intersection (and thus the TROVE focus) to any location along the common axis of the shifted ultrasound foci (dotted lines in figure 3f).

Imaging with the TROVE focus

We demonstrated the TROVE focusing and two-dimensional scanning strategy established above by scanning the TROVE focus in two-dimensions over a 1 μm diameter fluorescent bead (figure 5.4a) placed in a cuvette flanked by strong diffusers. We confirmed that, due to scattering, the bead could not be imaged via conventional epifluorescence (figure 5.4b). To acquire a TROVE image, we used a photomultiplier tube placed outside the sample to collect the backscattered fluorescence signal, excited by the scanned TROVE foci. From the TROVE image acquired, we obtained the point spread functions of 5.7 μm and 5.4 μm in the x and y direction respectively (figure 5.4d). As compared to TRUE focusing [20] we again find a resolution improvement of over six-fold (figure 5.4a).

We further demonstrated this resolution improvement by scanning two 1 μm fluorescent beads placed 15 μm apart (figure 5.4e). Due to the limited resolution of the TRUE technique, the TRUE image did not resolve the individual beads (figure 5.4g). In comparison, the two beads were well-resolved with TROVE imaging (figure 5.4h).

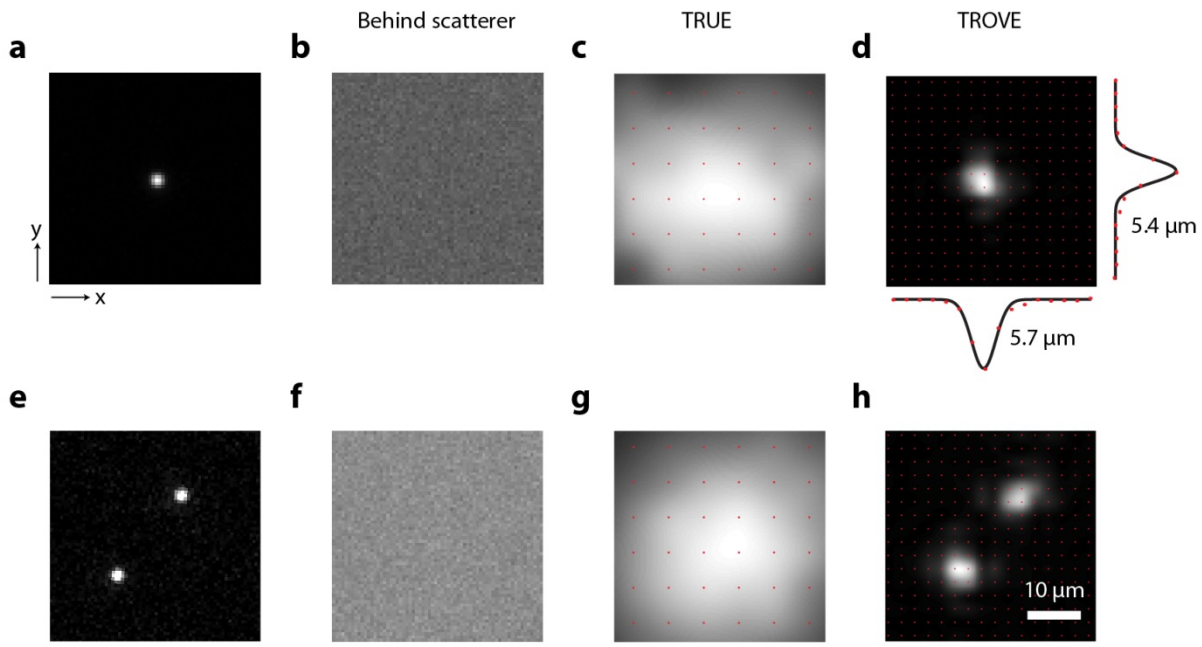

Fig. 5.4 | Point spread function and image acquisition. a, Epifluorescence image of a single bead. **b,** Epifluorescence image of a single bead as seen through a diffuser. **c,** Fluorescence image of single bead obtained by raster-scanning a TRUE focus. **d,** Fluorescence image of single bead obtained using TROVE focusing and scanning technique with profile of the fluorescent bead in x and y direction. **e,** Epifluorescence image of two fluorescent beads. **f,** Epifluorescence image of beads placed behind a diffuser. **g,** Fluorescence image of single bead obtained by raster-scanning a TRUE focus. **h,** TROVE focusing and scanning technique resolves the two beads placed between the strong diffusers. Locations of data points indicated by red dots. Data is interpolated for display using bicubic interpolation. Scale bar: 10 µm

5.4 DISCUSSION

In this work we presented a new method – time reversal of variance-encoded light (TROVE), to focus light at unprecedented, speckle-scale resolution in the diffusive regime. We demonstrated an optical setup that encoded the frequency-shifted speckle field originating from an ultrasound guide-star with a unique variance structure as well as a decoding algorithm that enabled the measurement and subsequent time reversal of individual optical modes at the ultrasound focus between highly diffusive scattering media. In addition to high resolution focusing to just one optical mode, TROVE provides a means to computationally access different optical modes within the ultrasound focus, enabling control of optical wavefronts within a scattering sample at speckle-scale resolution. We

demonstrated this ability to access different optical modes from a single dataset by two-dimensional scanning and imaging of fluorescent features. By 2D scanning over a 1 μm fluorescent bead, we characterized the lateral point spread function of the system to be 5.4 μm by 5.7 μm, a six-fold improvement compared to previous methods (see chapter 4 and also reference [21]). It would be straightforward to extend this method to allow three-dimensional scanning and imaging by repositioning the four ultrasound foci to another plane in the third dimension. However, we note here that the resolution in that dimension is dependent on the numerical aperture of the scattered light just as in digital TRUE described in chapter 3.

Recently, two papers have been published with the aim of achieving high resolution imaging between scatterers without the use of fluorescent or second-harmonic guide-stars. Here, we briefly discuss their relative advantages and disadvantages in comparison to TROVE: Bertolotti et al. present an elegant approach for imaging across scattering media that does not require ultrasound-tagging, but is instead based on the scattering memory effect. [24] The reliance on the memory effect is a hurdle for applications in which the memory effect is expected to be small compared to the area of interest (such as in many biological tissues). The approach outlined in our manuscript (TROVE) does not rely on the memory effect and is therefore not bound by this limitation. TROVE has the added feature that it creates an optical focus, hence not only enabling imaging but also photostimulation and image transfer across scattering media. In the other recent publication, Si et al. reported a method based on iterative time reversal across scattering media to achieve a threefold resolution improvement over TRUE. [25] Their approach is well-suited for moderate resolution improvement (~ 12 μm) and provides comparably fast acquisition times. In contrast, our approach requires more acquisitions, but achieves higher (optical speckle sized) resolution.

In essence, the TROVE method uncouples the resolution of the system from the size of the ultrasound guide-star. The resolution of the system is instead fundamentally determined by the size of the optical speckles at the ultrasound plane. Due to the low numerical

aperture of illumination in our experiments, the size of the optical speckles was 5 μm (full width at half maximum). The size of the speckles could be made smaller with different illumination configurations to yield higher resolution. However, this would require a corresponding increase in the number of wavefront measurements required, resulting in longer acquisition times.

This is an important trade-off because TROVE is based on optical time reversal, and is thus crucially reliant on the mechanical stability of the sample. Therefore, the duration of wavefront measurements and decoding computations should be shorter than the decorrelation time of the sample. In our demonstration, the time required for the measurement of a data set that enabled us to access a 30 μm by 30 μm field of view was 2 hours. Although current hardware speeds restrict the applicability of our method to mechanically stable samples, we anticipate that this requirement can be significantly relaxed; with the advent of faster cameras, spatial light modulators [26] and wavefront scramblers, applications even in more dynamic samples can ultimately be made possible.

5.5 METHODS

Optical setup

All data shown was acquired using a custom built setup that was based that of digital TRUE described in chapter 4 and in reference [20] (see figure 5.5): Briefly, a 2.7 W, 532 nm Q-switched laser (Navigator, SpectraPhysics, USA) pulsed at 20 kHz with a pulse width of 7 ns and a coherence length of 7 mm was used as a light source. After passing an optical isolator and a fixed attenuator, it was split into a reference beam and a sample beam. The sample beam was attenuated by a neutral density filter wheel, spatially filtered by a single mode optical fibre (Nufern 460HP, 20 cm length), collimated to a 0.8-mm waist beam and directed onto an optical diffuser disk on a rotation mount. The diffuse light exiting the disk was relayed to the surface of our sample with an irradiance of < 10 mW/mm^2. Inside the sample, a fraction of the light was frequency-shifted by an ultrasound transducer (element

size: 6.35 mm, focal length: 6 mm; V3330, Olympus NDT, Olympus, USA) operated at 50 MHz. To achieve maximal resolution along the axis of ultrasound propagation, the transducer was driven with short pulses (50 MHz, 100 V peak-to-peak carrier oscillation with a Gaussian pulse envelope of 13 ns full width at half maximum) triggered by the laser Q-switch signal at a fixed delay such that the ultrasound pulses coincided with the laser pulses at the same location, forming an ultrasound focus confined in three dimensions. To translate the ultrasound focus, the transducer was mounted on a computer-controlled micromanipulator (Sutter Instruments, USA). After passing through the sample, the scattered beam was recombined with the horizontally-polarized reference beam, which had also been frequency-shifted by an acousto-optic modulator (AOM; AFM-502-A1, IntraAction, USA). After passing a horizontally-aligned polarizer and another beamsplitter, the combined beams reached the surface of a phase-only spatial light modulator (SLM; vis-PLUTO, Holoeye, Germany), carefully aligned (1:1 pixel-to-pixel match) to the image plane of a high dynamic range sCMOS camera (pco.edge, PCO AG, Germany) (see Chapter 3 and appendix for principles and alignment).

Detection of fluorescence excitation by time-reversed light

The time-reversed beam was obtained by reflecting the blank reference beam off the SLM displaying the computed phase conjugate map. To directly visualize the time-reversed focus, the fluorescence emission from the quantum dot sheet was imaged with a 4x magnification onto a digital camera (Stingray F145, AVT, USA) fitted with a longpass filter (BLP02-561R, Semrock, USA) through the clear window between the scattering media.

This direct visualization was not utilized in subsequent experiments where fluorescent beads were imaged. For the time reversal of variance-encoded light (TROVE) imaging experiments, the emitted fluorescence that passed back through the scattering medium was reflected off a dichroic mirror (FF541-SDi01, Semrock, USA) and detected by a single-channel photomultiplier tube (H7827-002, Hamamatsu, Japan) fitted with a bandpass filter (FF01-572/28, Semrock, USA). Because of the comparatively low signal in the TRUE imaging experiments, a camera (Stingray F145, AVT, USA) was used to collect the fluorescence

emitted through the clear window between the diffusers. It is important to note that the camera was not used to resolve the bead, but just as a single pixel detector to collect the fluorescence emitted. In both TROVE and TRUE scanning experiments, we suppressed the fluorescence excited by the time reversal background with adaptive background subtraction (described in chapter 4 and in reference [20]).

Phase recording

We recorded the frequency-shifted field at the SLM plane and the frequency-shifted field at the ultrasound plane with digital phase-shifting holography. [27] The carrier oscillation driving the ultrasound transducer was shifted by 0, $\pi/2$, π and $3\pi/2$ phase delay relative to the oscillation driving the reference beam AOM and a frame was acquired for each phase delay. This 4-frame cycle was repeated 10 times and frames recorded at the same phase delay were averaged, resulting in four intensity maps that were used to reconstruct the complex field according to $E = (I_{\pi/2} - I_{3\pi/2}) + i(I_0 - I_\pi)$ (wherever we refer to amplitude and phase of the complex field, we used amplitude, A, and phase, θ, as in $E = A \cdot \exp(i \cdot \theta)$, as introduced in chapter 2). To obtain phase maps for each of the four overlapping ultrasound focus locations required for TROVE, we translated the ultrasound focus laterally using the micromanipulator (by 26 μm) and vertically by adjusting the delay of the ultrasound pulses (by 20 ns) versus the laser pulses.

Measurement and calculation of variance-encoded modes

We represent the speckled wavefront at the ultrasound by the vector $\boldsymbol{b}$, which describes the optical field values as a function of position. Part of this wavefront is frequency-shifted via the acousto-optic effect, resulting in a frequency-shifted optical field $\boldsymbol{b'} = \boldsymbol{b} \cdot \boldsymbol{G}$ (where $\boldsymbol{G}$ denotes a diagonal matrix whose diagonal elements $\boldsymbol{g}$ describe the Gaussian-shaped ultrasound focus). The frequency-shifted optical field $\boldsymbol{b'}$ propagates through the second section of the scattering medium (mathematically described by the scattering matrix $\boldsymbol{T_{BC}}$) before leaving the tissue as the output field $\boldsymbol{c} = \boldsymbol{b'} \cdot \boldsymbol{T_{BC}}$. In other words, $\boldsymbol{c}$ can be described as a

linear superposition of many optical transmission modes (or rows in $\boldsymbol{T_{BC}}$) and the weights of this superposition are given by $\boldsymbol{b'}$.

By randomizing the input beam to the ultrasound focus, we obtain many possible realizations of $\boldsymbol{b}$ and thus different frequency-shifted wavefronts $\boldsymbol{b'}$ and $\boldsymbol{c}$. We can represent each realization of $\boldsymbol{b}$, $\boldsymbol{b'}$ and $\boldsymbol{c}$ as rows of the matrices $\boldsymbol{B}$, $\boldsymbol{B'}$ and $\boldsymbol{C}$ respectively. Thus, the field recorded outside the sample at each diffuser position (each row in $\boldsymbol{C}$) will be a different linear combination of transmission modes (rows in $\boldsymbol{T_{BC}}$) originating from individual optical modes within the ultrasound focus. To resolve the ambiguity due to the symmetry of the ultrasound focus, we move the ultrasound between four overlapping positions (1 – 4), resulting in four slightly shifted ultrasound foci represented by $\boldsymbol{g_1}$, $\boldsymbol{g_2}$, $\boldsymbol{g_3}$ and $\boldsymbol{g_4}$ respectively. Since the data for the four foci are recorded for the same diffuser position in each presentation (or each row in $\boldsymbol{B}$ and $\boldsymbol{C}$), we get $\boldsymbol{B'_{1,2,3,4}} = \boldsymbol{B}\cdot\boldsymbol{G_{1,2,3,4}}$ and $\boldsymbol{C_{1,2,3,4}} = \boldsymbol{B'_{1,2,3,4}}\cdot\boldsymbol{T_{BC}}$. In other words, the underlying speckle patterns are the same for each of the four measurements.

To find a vector for phase conjugation back to a single mode, we looked for a vector v with high variance along the sum $\boldsymbol{C_1}+\boldsymbol{C_2}+\boldsymbol{C_3}+\boldsymbol{C_4}$ (short: $\boldsymbol{C_{1+2+3+4}}$) and low variances along the differences $\boldsymbol{C_{1-4}}$ and $\boldsymbol{C_{2-3}}$. We achieved this by finding the vector v that maximizes the ratio of variances $\boldsymbol{Q} = v^*(\boldsymbol{C_{1+2+3+4}}^*\boldsymbol{C_{1+2+3+4}})v/(v^*(\boldsymbol{C_{1-4}}^*\boldsymbol{C_{1-4}} + \boldsymbol{C_{2-3}}^*\boldsymbol{C_{2-3}})v)$. Since $\boldsymbol{Q}$ is a generalized Rayleigh Quotient, it can be maximized by $v = \mathrm{eig}[(\boldsymbol{C_{1-4}}^*\boldsymbol{C_{1-4}} + \boldsymbol{C_{2-3}}^*\boldsymbol{C_{2-3}})^{-0.5}(\boldsymbol{C_{1+2+3+4}}^*\boldsymbol{C_{1+2+3+4}})\ (\boldsymbol{C_{1-4}}^*\boldsymbol{C_{1-4}} + \boldsymbol{C_{2-3}}^*\boldsymbol{C_{2-3}})^{-0.5}\ ]$, where eig[…] denotes a function returning the principal eigenvector. Because the size of $\boldsymbol{C}$ is 1,000 x 500,000 in our experiments (number of realizations by number of pixels on the detector), a direct calculation of this eigenvector would involve a 500,000 x 500,000 matrix and would be computationally impractical. In the supplement, we derive an alternative approximation of v that involves only 1,000 x 1,000 matrices to achieve computational efficiency (see the appendix of this chapter). To digitally scan the time-reversed focus in space, we addressed different optical modes at the ultrasound focal plane by weighing the datasets $\boldsymbol{C_{1,2,3,4}}$ with prefactors that virtually moved the intersection point of the Gaussian foci.

Scanning / orthogonalisation of modes

To ensure separation between spatial modes corresponding to nearby points in the ultrasound plane, we used the following orthogonalisation strategy: First, by weighing the data matrices as described above, we obtained 100 optical modes v, corresponding to a 2D 6 x 6 grid of points at the XY-plane at the ultrasound focus (grid spacing: 5μm) and created a matrix $\boldsymbol{V}$ containing all vectors v in its columns. We then orthogonalised this matrix with the aid of its singular value decomposition: $\boldsymbol{V} = \boldsymbol{PQR'}$, where $\boldsymbol{Q}$ is a diagonal matrix; and $\boldsymbol{P}$ and $\boldsymbol{R}$ are orthogonal matrices. The orthogonalised version of $\boldsymbol{V}$ was then calculated as $\boldsymbol{V_o} = \boldsymbol{PR'}$. When each of the columns of $\boldsymbol{V_o}$ was time-reversed, we achieved focusing to the corresponding point on a grid with 5μm separation. To obtain a final 12 x 12 grid with 2.5 μm spacing, we performed the above procedure 4 times with shifted grids (with (0/2.5) μm shift in X and (0/2.5) μm shift in Y).

Sample

An open-top quartz glass cuvette with four polished sides (Starna Cells , CA) was filled with 2% (wt/wt) agarose gel (Invitrogen, USA). The glass cuvette was flanked on two sides with highly diffusing films (3M Scotch model #810, ~ 60 μm thick) that did not transmit a detectable ballistic component (measured with a detection threshold of less than 10^{-8} of the transmitted power – see chapter 4 and also reference [20] for description setup). The quantum dot sheet used to directly visualize the time-reversed foci were made with Qtracker 655 (Non-targeted quantum dots, Invitrogen) diluted in agarose such that the final concentration of quantum dots was 0.4 μM. The 1 μm diameter fluorescent beads (FluoSphere, Orange fluorescent) used for point spread function characterization and imaging demonstration were obtained from Invitrogen, USA. The fluorescent bead samples were obtained by drying a thin layer of the dilute fluorescent bead suspension on a piece of gel. Using a fluorescence microscope, the patch of gel with the desired fluorescent bead configuration is selected and cut out for embedding in the cuvette.

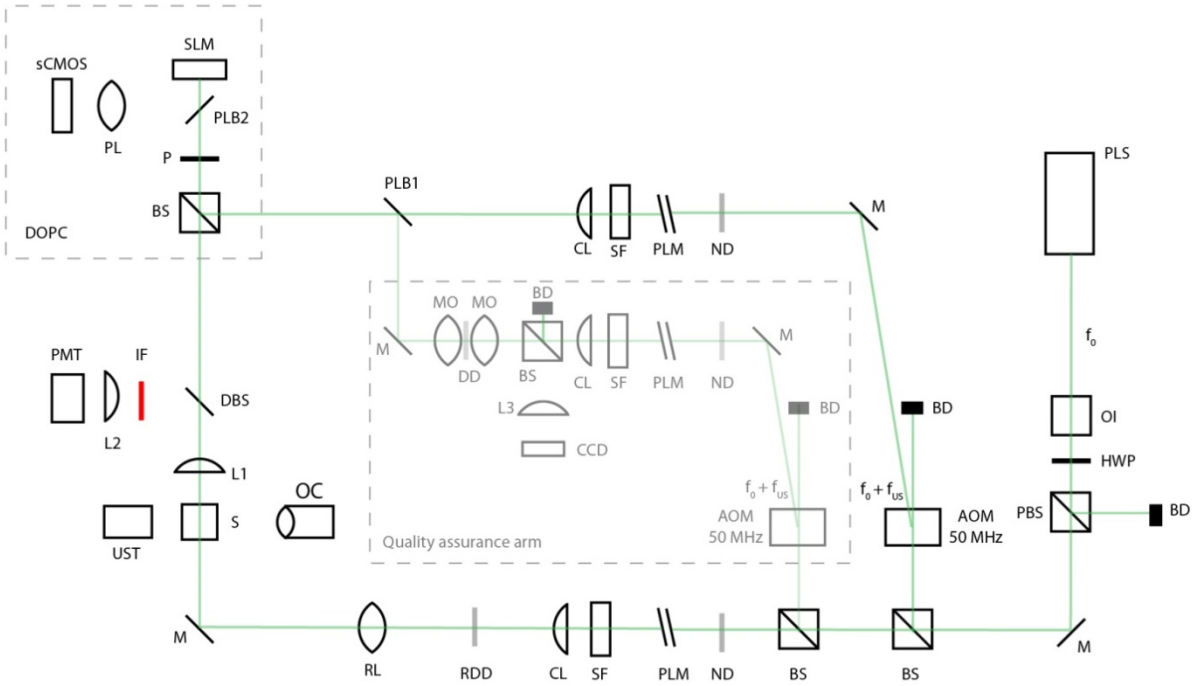

Fig. 5.5 | Setup diagram. Abbreviations: Pulsed laser source (PLS), Optical Isolator (OI), Half-wave plate (HWP), Polarizing beamsplitter (PBS), Beam dump (BD), Mirror (M), 50/50 cube beamsplitter (BS), Acousto-optic modulator (AOM), Neutral density filter wheel (ND), Path length matching arm (PLM), Single-mode ber acting as spatial filter (SF), Collimating lens (CL), Sample (S), Ultrasound transducer (UST), 50 mm planoconvex lens (L1), Dichroic beamsplitter (DBS), Interference filter (IF), 25 mm planoconvex lens (L2), Photomultiplier tube (PMT), Polarizer (P), 90/10 plate beamsplitter (PLB1), Digital optical phase conjugation setup (DOPC), 50/50 plate beamsplitter (PLB2), Photography compound lens (PL), sCMOS camera (sCMOS), Spatial light modulator (SLM), 300 mm plano-convex lens (L3), Microscope objective (MO), Diffuser disk (DD), Di user Disk on Rotation mount (RDD), Relay lens system (RL) imaging the illuminated spot on the diffuser disk onto the sample (RL), Observing camera (OC).

APPENDIX: SUPPLEMENTARY METHODS

Y.M.W did not make lead contributions towards most of the sections below. However, they are included for completeness and better understanding of the work presented in this chapter. The 'simulations' section is the work of B.J., with inputs from Y.M.W. The work described in 'Derivation of a computationally efficient decoding algorithm' is the work of R.H., with inputs from B.J, Y.M.W and A.M.. B.J, Y.M.W and R.H contributed to the section "Preservation of variance".

Simulations

As a first confirmation of our ability to encode and decode individual spatial transmission modes, we implemented the TROVE framework in a numerical simulation (see supplementary figure 5.Aa). As shown in supplementary figure 5.Ab, we generated complex random (normally distributed) matrices $\boldsymbol{B}$ and $\boldsymbol{T_{BC}}$ and chose two overlapping 1-D Gaussian functions $\boldsymbol{g_1}$ and $\boldsymbol{g_2}$, representing the shifted ultrasound foci that convert $\boldsymbol{B}$ into $\boldsymbol{B'_1}$ and $\boldsymbol{B'_2}$, respectively. We then calculated the matrices $\boldsymbol{C_1}$ and $\boldsymbol{C_2}$ that would have been measured outside the scattering medium in a real experiment. With the decoding strategy outlined in the Methods section, using only $\boldsymbol{C_1}$ - $\boldsymbol{C_2}$, we calculated the vector $\boldsymbol{v}$ that maximized the ratio of variances along $\boldsymbol{C_{1+2}}$ and $\boldsymbol{C_{1-2}}$ (supplementary figure 5.Ac). When this vector was time-reversed (multiplied by $\boldsymbol{T_{BC}^*}$ in the simulation), we were able to achieve a tight speckle-sized focus at the intersection of the two functions $\boldsymbol{g_1}$ and $\boldsymbol{g_2}$ (see supplementary figure 5.Ae). Comparatively, when we simulated the TRUE framework by time-reversing one row of either the $\boldsymbol{C_1}$ or the $\boldsymbol{C_2}$ matrix, we found that the resultant field consisted of a multi-mode focus, the size of the much larger Gaussian-shaped ultrasound ($\boldsymbol{g_1}$ or $\boldsymbol{g_2}$) (supplementary figure 5.Ad).

The simulations of TRUE and TROVE focusing described above were implemented using custom routines written in MATLAB (The Mathworks). The simulations were divided into three modules: First, we generated the complex random matrices $\boldsymbol{B_{1,2}}$ (1000 repetitions

by 200 pixels at ultrasound plane) and $\boldsymbol{T_{BC}}$ (200 pixels at ultrasound plane by 1000 pixels at the detection plane; the size of $\boldsymbol{T_{BC}}$ was chosen to be as large as the memory of our computer would permit). To simulate speckle autocorrelation, we convolved $\boldsymbol{B_{1,2}}$ with a speckle autocorrelation function (a Gaussian of FWHM = 5). We then chose Gaussian functions representing $\boldsymbol{g_{1,2}}$ the ultrasound foci (FWHM = 50, σ = 21, shifted by 2σ) and calculated the matrices $\boldsymbol{C_{1,2}} = \boldsymbol{B}\cdot\boldsymbol{G_{1,2}}\cdot\boldsymbol{T_{BC}}$. Second, we performed the same analysis on $\boldsymbol{C_{1,2}}$ which we also performed on experimentally measured data to obtain the vector $\boldsymbol{v}$ maximizing the Rayleigh quotient (see above). Third, we simulated time reversal of this vector by multiplying its complex conjugate by $\boldsymbol{T_{BC}^T}$. Finally, the time-reversed focus was moved by computationally shifting the intersection point between the two Gaussian foci. This is achieved by changing the scalar k in the equation $\boldsymbol{C_{1\text{-}2}} = \boldsymbol{C_1} - k\boldsymbol{C_2}$. The intersection between $\boldsymbol{g_1}$ and $k\cdot\boldsymbol{g_2}$ could be shifted predictably according to $k = 2e^{x/\sigma}$ (where $\boldsymbol{g_1}$ and $\boldsymbol{g_2}$ are Gaussian functions whose means are separated by 2σ, and x is the shift of the intersection point).

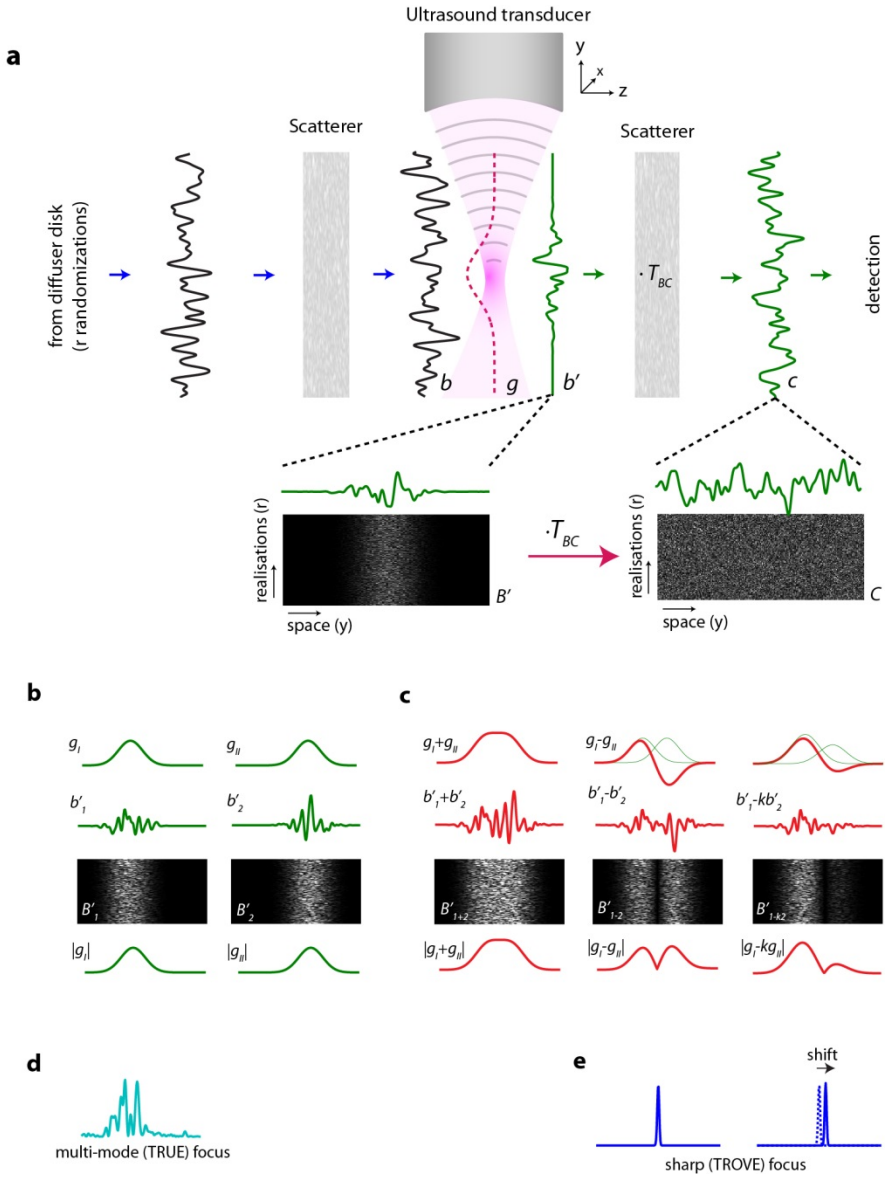

Figure 5.A | Variance encoding of optical transmission modes. **a,** Schematic of the scattering process and the setup: An input wavefront illuminates the sample and is randomized as it reaches the ultrasound focal plane (represented as a 1D vector (b). A fraction of the randomized wavefront passing the Gaussian-shaped ultrasound focus (g) gets frequency-shifted by the acousto-optic effect (b'), before propagating through the second tissue section (represented by the scattering matrix T_{BC}). The frequency-shifted wavefront leaving the tissue (c) is then selectively detected using digital phase-shifting holography. As the input wavefront reaching the sample is randomized by rotating a diffuser disk, all realizations of the wavefronts can be inserted into the rows of one data matrix for each plane. **b,** Exemplary shifted ultrasound foci $g_{1,2}$, wavefronts $b'_{1,2}$ and data sets $B'_{1,2}$ (displaying the absolute of the complex valued matrices). Due to the complex normal statistics of speckle, the expected variance along the columns of $B'_{1,2}$ is $|g_{1,2}|^2$. **c,** Sum (left) and difference (middle and right) data sets calculated from the two data sets shown in panel b. Note

that the expected variance along columns of B'_{1-2} and B'_{1+2} will follow $|g_1-g_2|^2$ and $|g_1+g_2|^2$, respectively. Right: difference of differentially weighted datasets, with shifted null-point of variance. **d,** Simulation of regular time reversal (TRUE focusing), resulting in a speckled optical focus the size of the ultrasound focus. **e,** Simulation of time reversal of variance-encoded light (TROVE), resulting in a focus the size of an individual speckle, which can be computationally shifted. (Plots show normalized intensity).

Derivation of a computationally efficient decoding algorithm

The proposed eigenvalue formula used to determine the optimal phase pattern $\boldsymbol{\nu}^*$ to display on the spatial light modulator, given an acquired data set, is justified as follows. We limit this proof to a two dimensional geometry, with straightforward extension to three dimensions. We assume the scattering events between the ultrasound focus at the ultrasound plane and the detector at the output plane are represented by a transmission matrix $\boldsymbol{T}$. The detector collects m measurements across n pixels of speckle data with the ultrasound focus located first at position 1, and then at position 2. We assume the underlying speckle field along $\boldsymbol{b}$ does not change between measurements with the ultrasound focus at these two different locations. This allows us to express the recorded data with a shared underlying speckle data matrix (at the ultrasound plane), $\boldsymbol{B}$, modified by two different Gaussian envelopes representing the ultrasound at two different positions, described by diagonal matrices $\boldsymbol{G_1}$ and $\boldsymbol{G_2}$, respectively. Thus, the recorded ultrasound modulated speckle patterns are $\boldsymbol{BG_1T}$ and $\boldsymbol{BG_2T}$. The two calculated data matrices of interest are,

$$\boldsymbol{C_{1+2}} = \boldsymbol{BG_1T} + \boldsymbol{BG_2T} = \boldsymbol{BG_{1+2}T} \quad (1)$$

$$\boldsymbol{C_{1-2}} = \boldsymbol{BG_1T} - \boldsymbol{BG_2T} = \boldsymbol{BG_{1-2}T}, \quad (2)$$

where $\boldsymbol{G_1}$ and $\boldsymbol{G_2}$ are n x n square with a shifted Gaussian function along the diagonal and zeros elsewhere. $\boldsymbol{G_{1+2}}$ and $\boldsymbol{G_{1-2}}$ are also square diagonal matrices containing the sum and difference of the Gaussian functions respectively. The m x n underlying data matrix $\boldsymbol{B}$ contains independent speckle field measurements along its rows. Note that due to our ordering of matrices, the spatial covariance matrix of the above data will take the form $\boldsymbol{CC}^*$,

while the data's Gram matrix will take the form $\boldsymbol{C}^{*}\boldsymbol{C}$, which is opposite from common notation.

As discussed in the main text, TROVE's computational goal is to identify a single mode at the ultrasound plane corresponding to the intersection of the two Gaussian ultrasound envelopes centred at g_1 and g_2. This goal is achieved by finding a vector $\boldsymbol{v}$ along which the variance of $\boldsymbol{C}_{1+2}$ is maximal and the variance of $\boldsymbol{C}_{1-2}$ is minimal. Such a vector $\boldsymbol{v}$ will maximize the Rayleigh Quotient $\boldsymbol{Q}$ of the covariance matrices of the two datasets, $\boldsymbol{C}_{1-2}^{*}\boldsymbol{C}_{1-2}$ and $\boldsymbol{C}_{1+2}^{*}\boldsymbol{C}_{1+2}$:

$$\boldsymbol{Q} = \boldsymbol{v}^{*}\boldsymbol{C}_{1+2}^{*}\boldsymbol{C}_{1+2}\boldsymbol{v}/(\boldsymbol{v}^{*}\boldsymbol{C}_{1-2}^{*}\boldsymbol{C}_{1-2}\,\boldsymbol{v}). \tag{3}$$

The maximization of the Rayleigh Quotient above is associated with a solution to the generalized eigensystem,

$$\boldsymbol{C}_{1+2}^{*}\boldsymbol{C}_{1+2}\boldsymbol{v} = \boldsymbol{C}_{1-2}^{*}\boldsymbol{C}_{1-2}\lambda\boldsymbol{v}, \tag{4}$$

with eigenvalue λ. We express the eigenvector $\mathbf{v}$ associated with the maximum eigenvalue λ of this general eigensystem as,

$$\boldsymbol{v} = \mathrm{eig}[(\boldsymbol{C}_{1-2}^{*}\boldsymbol{C}_{1-2})^{-1}\boldsymbol{C}_{1+2}^{*}\boldsymbol{C}_{1+2}], \tag{5}$$

where eig[…] represents a principal eigenvector identification operator. In practice, due to the high n x n dimensionality of the spatial covariance matrices $\boldsymbol{C}_{1+2}^{*}\boldsymbol{C}_{1+2}$ and $\boldsymbol{C}_{1-2}^{*}\boldsymbol{C}_{1-2}$, Equation (5) is difficult to computationally evaluate. Instead, we desire an eigenvector solution based on the much smaller m x m Gram matrices $\boldsymbol{C}_{1+2}\boldsymbol{C}_{1+2}^{*}$ and $\boldsymbol{C}_{1-2}\boldsymbol{C}_{1-2}^{*}$.

We apply two approximations about the structure of the recorded speckle data to determine a computational solution based on two m x m Gram matrices. First, we suppose that the complex random Gaussian transmission matrix $\boldsymbol{T}$ satisfies $\boldsymbol{T}\boldsymbol{T}^{*} \approx \boldsymbol{I}$. This approximation commonly underlies phase conjugation experiments, and the associated error approaches zero as $\boldsymbol{T}$ increases in size (i.e. more transmitted speckles are measured and phase conjugated) – as long as long-range (C_2) and infinite-range (C_3) correlations can

be neglected. [28] Such higher-order correlations may be neglected in samples with many open channels, including those used in our experiments as well as biological tissue. Second, we also assume the matrix $\boldsymbol{B}$ comprising the many recorded underlying speckle fields at the ultrasound focus is also complex random Gaussian. As the recorded data matrix is rectangular (m x n, $n > m$), this leads us to the approximations $\boldsymbol{B}^*\boldsymbol{B} \approx \boldsymbol{I}_{nxn}$ and $\boldsymbol{B}\boldsymbol{B}^* \approx \boldsymbol{I}_{mxm}$, where $\boldsymbol{I}$ is the identity matrix, following the same approximation applied to T. The latter approximation improves as m approaches n.

Proceeding with the derivation, we first move $\boldsymbol{C}_{1\text{-}2}{}^*\boldsymbol{C}_{1\text{-}2}$ in equation (4) to the left side by taking its inverse:

$$(\boldsymbol{C}_{1\text{-}2}{}^*\boldsymbol{C}_{1\text{-}2})^{-1}\boldsymbol{C}_{1+2}{}^*\boldsymbol{C}_{1+2}\boldsymbol{v} = \lambda\boldsymbol{v}. \tag{6}$$

Then, plugging equation (1) and equation (2) into equation (6) leads to,

$$(\boldsymbol{T}^*\boldsymbol{G}_{1\text{-}2}\boldsymbol{B}^*\boldsymbol{B}\boldsymbol{G}_{1\text{-}2}\boldsymbol{T})^{-1}(\boldsymbol{T}^*\boldsymbol{G}_{1+2}\boldsymbol{B}^*\boldsymbol{B}\boldsymbol{G}_{1+2}\boldsymbol{T})\boldsymbol{v} = \lambda\boldsymbol{v}. \tag{7}$$

Applying our second approximation that $\boldsymbol{B}^*\boldsymbol{B} = \boldsymbol{I}$, this simplifies to,

$$(\boldsymbol{T}^*\boldsymbol{G}_{1\text{-}2}{}^2\boldsymbol{T})^{-1}(\boldsymbol{T}^*\boldsymbol{G}_{1+2}{}^2\boldsymbol{T})\ \boldsymbol{v} = \lambda\boldsymbol{v}. \tag{8}$$

Evaluating the inverse and using our first approximation that $\boldsymbol{T}^{-1} = \boldsymbol{T}^*$ leads to,

$$\boldsymbol{T}^*\boldsymbol{G}_{1\text{-}2}{}^{-2}\boldsymbol{G}_{1+2}{}^2\boldsymbol{T}\boldsymbol{v} = \lambda\boldsymbol{v}. \tag{9}$$

Here, $\boldsymbol{G}_{1\text{-}2}{}^{-2}$ is a square matrix with $\boldsymbol{G}_{1\text{-}2}{}^{-2}(i,j) = 1/\boldsymbol{G}_{1\text{-}2}{}^2(i,j)$ for all $i=j$ and $\boldsymbol{G}_{1\text{-}2}{}^{-2}(i,j) = 0$ for all $i\sim=j$. Equation (9) can be transformed from an n x n matrix eigensystem to a smaller m x m matrix eigensystem by attempting to solve for a new eigenvector $\boldsymbol{y}$, where $\boldsymbol{v} = \boldsymbol{T}^*\boldsymbol{B}^*\boldsymbol{y}$. Plugging this relationship into equation (9) yields,

$$\boldsymbol{T}^*\boldsymbol{G}_{1\text{-}2}{}^{-2}\boldsymbol{G}_{1+2}{}^2\ \boldsymbol{T}(\boldsymbol{T}^*\boldsymbol{B}^*\boldsymbol{y}) = \lambda(\boldsymbol{T}^*\boldsymbol{B}^*\boldsymbol{y}). \tag{10}$$

Applying our first approximation to the left side and then multiplying both sides by $\boldsymbol{T}$ from the left leads to,

$$\boldsymbol{G}_{1\text{-}2}^{-2}\,\boldsymbol{G}_{1+2}^{2}\boldsymbol{B}^{*}\boldsymbol{y} = \boldsymbol{B}^{*}\lambda\boldsymbol{y}. \tag{11}$$

Multiplying by an additional factor $\boldsymbol{B}$ from the left on either side and applying our second approximation to the right side leads to,

$$\boldsymbol{B}\boldsymbol{G}_{1\text{-}2}^{-2}\boldsymbol{G}_{1+2}^{2}\boldsymbol{B}^{*}\boldsymbol{y} = \lambda\boldsymbol{y}. \tag{12}$$

Again, following our approximation that $\boldsymbol{B}^{*}\boldsymbol{B} = \boldsymbol{I}$, we can insert this term into the middle of Equation (12) to produce,

$$(\boldsymbol{B}\boldsymbol{G}_{1\text{-}2}^{-2}\boldsymbol{B}^{*})(\boldsymbol{B}\,\boldsymbol{G}_{1+2}^{2}\boldsymbol{B}^{*})\boldsymbol{y} = \lambda\boldsymbol{y}. \tag{13}$$

$\boldsymbol{G}_{1\text{-}2}^{-2}$ is a diagonal matrix, and under our second assumption $\boldsymbol{B}$ and $\boldsymbol{B}^{*}$ setup an orthogonal basis for the term in parentheses on the left. Thus, Equation (13) is equivalent to,

$$(\boldsymbol{B}\boldsymbol{G}_{1\text{-}2}^{2}\boldsymbol{B}^{*})^{-1}\,(\boldsymbol{B}\boldsymbol{G}_{1+2}^{2}\boldsymbol{B}^{*})\boldsymbol{y} = \lambda\boldsymbol{y}. \tag{14}$$

Here, we see that the two terms in the parenthesis can be expressed in terms of the original data matrices $\boldsymbol{C}_{1+2}$ and $\boldsymbol{C}_{1\text{-}2}$ as,

$$(\boldsymbol{C}_{1\text{-}2}\boldsymbol{C}_{1\text{-}2}^{*})^{-1}(\boldsymbol{C}_{1+2}\boldsymbol{C}_{1+2}^{*})\boldsymbol{y} = \lambda\boldsymbol{y}, \tag{15}$$

which is the desired re-expression of the eigensystem in Equation (4) in terms of the smaller m x m Gram matrices $\boldsymbol{C}_{1+2}\boldsymbol{C}_{1+2}^{*}$ and $\boldsymbol{C}_{1\text{-}2}\boldsymbol{C}_{1\text{-}2}^{*}$. Our first approximation is used once more while transforming Equation (14) to Equation (15). We can find the originally desired eigenvector $\boldsymbol{\nu}$ associated with the largest eigenvalue λ by solving Equation (15) for the largest eigenvector $\boldsymbol{y}$, and then solving $\boldsymbol{\nu} = \boldsymbol{T}^{*}\boldsymbol{B}^{*}\boldsymbol{y}$:

$$\boldsymbol{\nu} = \boldsymbol{T}^{*}\boldsymbol{B}^{*}\cdot\mathrm{eig}[(\boldsymbol{C}_{1\text{-}2}\boldsymbol{C}_{1\text{-}2}^{*})^{-1}(\boldsymbol{C}_{1+2}\boldsymbol{C}_{1+2}^{*})\,] = (\boldsymbol{B}\boldsymbol{T})^{*}\cdot\mathrm{eig}[(\boldsymbol{C}_{1\text{-}2}\boldsymbol{C}_{1\text{-}2}^{*})^{-1}(\boldsymbol{C}_{1+2}\boldsymbol{C}_{1+2}^{*})]. \tag{16}$$

Since the experiment does not allow direct access to the data matrix $\boldsymbol{B}\boldsymbol{T}$, we use the approximation $\boldsymbol{B}\boldsymbol{G}_{1+2}\boldsymbol{T} \approx \boldsymbol{B}\boldsymbol{T}$ to instead generate the approximate eigenvector evaluation,

$$\boldsymbol{\nu} \approx \boldsymbol{C}_{1+2}^{*}\cdot\mathrm{eig}[(\boldsymbol{C}_{1\text{-}2}\boldsymbol{C}_{1\text{-}2}^{*})^{-1}(\boldsymbol{C}_{1+2}\boldsymbol{C}_{1+2}^{*})] \tag{17}$$

This final approximation is justified as follows. We should expect a successful solution to Equation (16) to take the general form $\boldsymbol{\nu} = (\boldsymbol{d}(x)\cdot\boldsymbol{T})^{*}$, where $\boldsymbol{d}(x)$ is a row vector with 1 in

row x and 0's elsewhere. This is supported by the intuitive notion that our goal is to refocus to a small delta function-like spot at a position x, which is equivalent to determining one row of $\boldsymbol{T}$. Under such an assumption, inserting a diagonal matrix $\boldsymbol{G}$ between $\boldsymbol{d}(x)$ and $\boldsymbol{T}$ does not alter their matrix product up to a constant scaling factor, given $\boldsymbol{G}(x,x)$ is non-zero, which is guaranteed by setting $\boldsymbol{G}=\boldsymbol{G}_{1+2}$ and ensuring the desired mode x is near the intersection of the two summed Gaussians.

Finally, for computational efficiency, the above equation can be rewritten to involve an eigendecomposition of a Hermitian matrix:

$$\boldsymbol{v} \approx \boldsymbol{C}_{1+2}^{*} \cdot (\boldsymbol{C}_{1-2}\boldsymbol{C}_{1-2}^{*})^{-1/2} \cdot \mathrm{eig}[(\boldsymbol{C}_{1-2}\boldsymbol{C}_{1-2}^{*})^{-1/2}(\boldsymbol{C}_{1+2}\boldsymbol{C}_{1+2}^{*})(\boldsymbol{C}_{1-2}\boldsymbol{C}_{1-2}^{*})^{-1/2}] \tag{18}$$

No additional approximations are required to obtain equation (18) from equation (17).

This derivation can be easily extended to the 2D case, where we find $\boldsymbol{v}$ along which the variance of $\boldsymbol{C}_{1+2+3+4}$ is maximal and the sum of the variances of $\boldsymbol{C}_{1-4}$ and $\boldsymbol{C}_{2-3}$ is minimal, obtaining:

$$\boldsymbol{v} \approx \boldsymbol{C}_{1+2+3+4}^{*} \cdot (\boldsymbol{C}_{1-4}\boldsymbol{C}_{1-4}^{*} + \boldsymbol{C}_{2-3}\boldsymbol{C}_{2-3}^{*})^{-1/2} \cdot \mathrm{eig}[(\boldsymbol{C}_{1-4}\boldsymbol{C}_{1-4}^{*} + \boldsymbol{C}_{2-3}\boldsymbol{C}_{2-3}^{*})^{-1/2}(\boldsymbol{C}_{1+2+3+4}\boldsymbol{C}_{1+2+3+4}^{*})(\boldsymbol{C}_{1-4}\boldsymbol{C}_{1-4}^{*} + \boldsymbol{C}_{2-3}\boldsymbol{C}_{2-3}^{*})^{-1/2}] \tag{19}$$

Preservation of variance

The main article refers to the fact that variance across realizations is preserved as modes propagate through a scatter. We derive and justify the statement as follows: We note that the covariance of realizations in the dataset $\boldsymbol{B'}$ is expressed as $\boldsymbol{B'B'}^{*}$. Using the approximation $\boldsymbol{TT}^{*} \approx \boldsymbol{I}$ described above, we can derive

$$\boldsymbol{CC}^{*} = (\boldsymbol{B'T})(\boldsymbol{B'T})^{*} = \boldsymbol{B'TT}^{*}\boldsymbol{B'}^{*} \approx \boldsymbol{B'B'}^{*} \tag{20}$$

This equation states that the realizations covariance at the ultrasound plane can be approximated by the realizations covariance at the output plane.

REFERENCES

1 Freund, I. Looking through Walls and around Corners. *Physica A* **168**, 49-65, (1990).

2 Vellekoop, I.M., Lagendijk, A. & Mosk, A.P. Exploiting disorder for perfect focusing. *Nat Photon* **4**, 320-322, (2010).

3 Vellekoop, I.M. & Mosk, A.P. Focusing coherent light through opaque strongly scattering media. *Opt. Lett.* **32**, 2309-2311, (2007).

4 Katz, O., Small, E. & Silberberg, Y. Looking around corners and through thin turbid layers in real time with scattered incoherent light. *Nat. Photonics* **6**, 549-553, (2012).

5 Katz, O., Small, E., Bromberg, Y. & Silberberg, Y. Focusing and compression of ultrashort pulses through scattering media. *Nat. Photonics* **5**, 372-377, (2011).

6 van Putten, E.G. *et al.* Scattering Lens Resolves Sub-100 nm Structures with Visible Light. *Physical Review Letters* **106**, 193905, (2011).

7 Aulbach, J., Gjonaj, B., Johnson, P.M., Mosk, A.P. & Lagendijk, A. Control of Light Transmission through Opaque Scattering Media in Space and Time. *Phys. Rev. Lett.* **106**, (2011).

8 Lerosey, G., De Rosny, J., Tourin, A. & Fink, M. Focusing beyond the diffraction limit with far-field time reversal. *Science* **315**, 1120-1122, (2007).

9 Yaqoob, Z., Psaltis, D., Feld, M.S. & Yang, C.H. Optical phase conjugation for turbidity suppression in biological samples. *Nat. Photonics* **2**, 110-115, (2008).

10 Popoff, S., Lerosey, G., Fink, M., Boccara, A.C. & Gigan, S. Image transmission through an opaque material. *Nat. Commun.* **1**, 81, (2010).

11 Popoff, S.M. *et al.* Measuring the transmission matrix in optics: an approach to the study and control of light propagation in disordered media. *Phys. Rev. Lett.* **104**, 100601, (2010).

12 Cizmar, T. & Dholakia, K. Exploiting multimode waveguides for pure fibre-based imaging. *Nat. Commun.* **3**, 1027, (2012).

13 Choi, Y. *et al.* Scanner-Free and Wide-Field Endoscopic Imaging by Using a Single Multimode Optical Fiber. *Physical Review Letters* **109**, 203901, (2012).

14 Choi, W., Mosk, A.P., Park, Q.H. & Choi, W. Transmission eigenchannels in a disordered medium. *Phys. Rev. B* **83**, 134207, (2011).

15 Vellekoop, I.M., Cui, M. & Yang, C.H. Digital optical phase conjugation of fluorescence in turbid tissue. *Appl. Phys. Lett.* **101**, (2012).

16 Hsieh, C.L., Pu, Y., Grange, R. & Psaltis, D. Digital phase conjugation of second harmonic radiation emitted by nanoparticles in turbid media. *Opt. Express* **18**, 12283-12290, (2010).

17 Xu, X., Liu, H. & Wang, L.V. Time-reversed ultrasonically encoded optical focusing into scattering media. *Nat. Photonics* **5**, 154-157, (2011).

18 Lai, P., Xu, X., Liu, H., Suzuki, Y. & Wang, L.V. Reflection-mode time-reversed ultrasonically encoded optical focusing into turbid media. *J. Biomed. Opt.* **16**, 080505, (2011).

19 Liu, H., Xu, X., Lai, P. & Wang, L.V. Time-reversed ultrasonically encoded optical focusing into tissue-mimicking media with thickness up to 70 mean free paths. *J. Biomed. Opt.* **16**, 086009, (2011).

20 Wang, Y.M., Judkewitz, B., DiMarzio, C.A. & Yang, C.H. Deep-tissue focal fluorescence imaging with digitally time-reversed ultrasound-encoded light. *Nat. Commun.* **3**, (2012).

21 Si, K., Fiolka, R. & Cui, M. Fluorescence imaging beyond the ballistic regime by ultrasound-pulse-guided digital phase conjugation. *Nat Photon* **6**, 657-661, (2012).

22 Zell, K., Sperl, J.I., Vogel, M.W., Niessner, R. & Haisch, C. Acoustical properties of selected tissue phantom materials for ultrasound imaging. *Physics in Medicine and Biology* **52**, N475-N484, (2007).

23 Vellekoop, I.M. *Controlling the propagationg of light in disordered scattering media* PhD thesis, University of Twente, (2009).

24 Bertolotti, J. *et al.* Non-invasive imaging through opaque scattering layers. *Nature* **491**, 232-234, (2012).

25 Si, K., Fiolka, R. & Cui, M. Breaking the spatial resolution barrier via iterative sound-light interaction in deep tissue microscopy. *Sci. Rep.* **2**, (2012).

26 Conkey, D.B., Caravaca-Aguirre, A.M. & Piestun, R. High-speed scattering medium characterization with application to focusing light through turbid media. *Opt. Express* **20**, 1733-1740, (2012).

27 Yamaguchi, I. & Zhang, T. Phase-shifting digital holography. *Opt. Lett.* **22**, 1268-1270, (1997).

28 van Albada, M.P., de Boer, J.F. & Lagendijk, A. Observation of long-range intensity correlation in the transport of coherent light through a random medium. *Physical Review Letters* **64**, 2787-2790, (1990).

Chapter 6
Future work and conclusion

6.1 FUTURE WORK

Here, we briefly discuss some improvements to digital TRUE and TROVE and the considerations in determining the ultimate limits to these improvements.

System improvements

Dependence on the detection of ultrasound tagged photons

Both digital TRUE and TROVE critically depend on the detection of ultrasound tagged photons to elucidate the appropriate time reversal field. Because of the low ultrasound tagging (frequency-shifting) efficiency, the frequency-shifted beam is very weak. Thus, the limitations in improvements on the systems are crucially tied to the amount of frequency-shifted signal present and the ability to detect it.

In our systems, the ultrasound tagged photons are detected interferometrically such that the detected intensity on the camera is

$$I(x,y) = I_{ref} + I_{untagged} + I_{tagged} + 2\sqrt{I_{ref} I_{tagged}}\cos[\Delta\varphi(x,y)] \tag{6.1}$$

where I_{ref} is the intensity of the reference beam, $I_{untagged}$ is the intensity of the non-frequency-shifted light in the sample beam, I_{tagged} is the intensity of the ultrasound frequency-shifted light, and $\Delta\varphi(x,y)$ is the spatially varying phase difference between the reference beam and the ultrasound frequency-shifted light field. To simplify our discussions, we assume a shot-noise-limited system (ignoring detector noise and limited camera well depth etc.), such that the signal-to-noise ratio (*SNR*) can be estimated (assuming the amplitude of the AC component approximates the signal) as

$$SNR = \frac{2\tau\varepsilon\sqrt{I_{ref}I_{tagged}}A_{det}/hf}{\sqrt{\tau\varepsilon A_{det}\left(I_{ref} + I_{untagged} + I_{tagged}\right)/hf}} \approx 2\sqrt{\frac{\tau\varepsilon I_{tagged}A_{det}}{hf}} \propto \sqrt{N_{tagged}} \quad (6.1)$$

where A_{det} is the detector area, h is the Planck constant, f is the frequency of light, ε is the detector efficiency and τ is the integration time of the detector. We see from the above exercise that in the shot-noise limited regime, assuming the untagged light and the tagged light are far lower in intensity than the reference beam, the SNR is proportional to the number of signal photons (ultrasound-tagged photons) that are collected by the detector over a certain time period.

Although the power of tagged photons is a fixed fraction of the light input to the tissue and can be increased by adjusting the input power, this is limited by the safety limit of light irradiation on tissue (ANSI standard: 2 mW/mm^2 for visible light on skin). We see from the derivation above that even with a small population of tagged photons, we can increase the detector integration time τ to achieve adequate SNR. However, τ is practically limited by the time constant of sample motion (see chapter 3.3). Thus, the specification of the speed of the improved TRUE or TROVE designs has to be informed by the decorrelation times of living tissues.

As we will see in the discussions below, the limits to the targeted improvements in TRUE and TROVE resolution, depth of penetration, system speed and TRUE peak-to-background ratio all closely relate to the number of tagged photon counts and thus the detection SNR. An understanding of their relationships will allow the construction of a complete model that investigates the interplay between these parameters.

Hardware speed

Because digital TRUE and TROVE are based on time reversal, they are crucially dependent on the mechanical stability of the samples over the time of wavefront measurements and playback. Currently, the time taken to form a digital TRUE focus in our

demonstration is on the order of seconds. Because of the number of wavefront recordings required for computation, TROVE required 2 hours for a data set that allowed focusing over a field of view of 30 by 30 microns. Although the recording and playback times for the respective methods are sufficiently short for the samples used, they are too long for *in vivo* biological applications that typically have decorrelation times on the order of milliseconds. [1-3] In order for digital TRUE and TROVE to be useful in photostimulation applications, the techniques will have to be sped up to the order of the decorrelation times. For practical imaging purposes, at least an additional order of magnitude improvement will be required.

A moderate improvement in wavefront acquisition speed can be obtained with the use of off-axis one-shot wavefront measurements or the reduction in number of phase steps in phase-shifting holography that sacrifices phase accuracy. In our digital TRUE and TROVE demonstrations, often several frames will have to be acquired to achieve an optimal signal-to-noise ratio. The use of faster cameras with deeper well capacities and faster spatial light modulators that operate at speeds on the order of kilohertz (e.g. digital micromirror devices, deformation mirror arrays) can potentially speed up the digital TRUE refresh rate to tens of milliseconds. These hardware and technologies are already available commercially and we anticipate further technology improvements will enable corresponding improvements. Where camera frame rates are limited by exposure time and the camera well depth is not limiting, the rate of wavefront acquisition will be fundamentally bound by SNR considerations as discussed in the previous section. We anticipate that a better understanding of SNR considerations in relation to time reversal fidelity will allow us to make an informed trade-off between SNR and acquisition time.

Resolution

The resolution of TRUE is fundamentally limited by the focused ultrasound beam diameter *BD*, which is related to the focal length of the ultrasound transducer F, the speed of acoustic wave in medium c, the ultrasound frequency f and the transducer element diameter

D. [4]

$$BD = 1.02Fc/fD$$

The beam diameter of currently available focusing transducers closely approaches the diffraction limit of ultrasound (on the order of wavelength). The ultrasound transducer we utilized in our experiments has a central frequency of 50 MHz and is able to produce a focal diameter of ~30 μm. With higher central frequency, this can be further reduced. However, we note that ultrasound attenuation increases logarithmically with frequency (see figure 6.1), contributing to the issue of ultrasound tagged photon detection. Along the same lines, a smaller ultrasound focus will intercept a smaller portion of the scattered wavefront resulting in less ultrasound tagged photons. Although these could be countered by increasing ultrasound power, the damage thresholds of the ultrasound transducer elements set limits to this approach, especially since the attenuation with frequency is logarithmic.

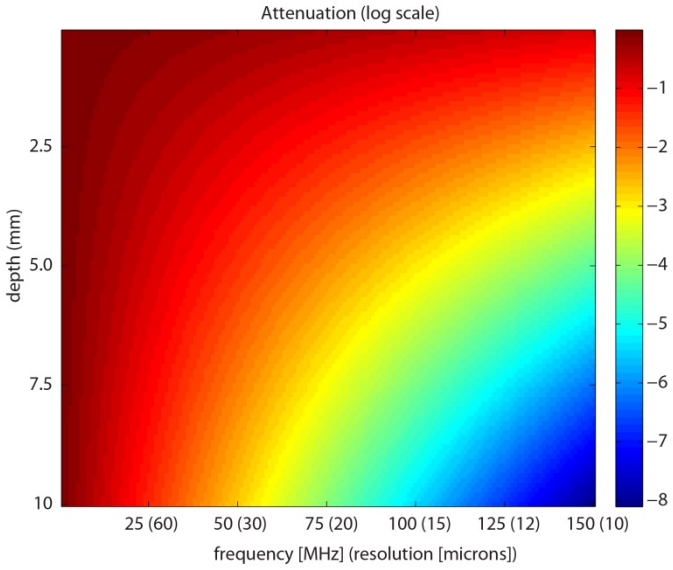

Fig. 6.1 | Plot of ultrasound attenuation with depth and frequency. It is known that the attenuation of ultrasound varies with depth of propagation and the frequency of the acoustic wave according to Attenuation [dB] = $\alpha \cdot f \cdot l$, where α is the tissue attenuation coefficient; is the ultrasound frequency; l is ultrasound path length. Here we assume a value of 0.54/MHz/cm for soft tissues. [5] We estimate the resolution as the wavelength of the ultrasound in soft tissues, with speed ~1500 m/s (equation (4.1)).

The resolution of TROVE is limited by the optical speckle size. This is in turn dependent on the wavelength of incident light, the scattering properties of the sample and the geometry of illumination. However, with a smaller ultrasound focus and thus less modulated speckles, it would be possible to decrease the acquisition time of TROVE.

Depth of penetration

The penetration depth of TRUE and TROVE are limited by ultrasound attenuation which scales logarithmically also with depth (see figure 6.1). In addition, the light diffusion with depth also decreases the proportion of the scattered wavefront that passes through the focus. Thus, the penetration depth limit again critically determines the photon budget and thus the SNR of the system.

Setup geometry

The discussion above is not limited to the transmission geometry that is utilized in our demonstrations of digital TRUE and TROVE. Indeed, a reflection geometry where the illumination beam, ultrasound transducer and DOPC are on the same side of the tissue (i.e. back reflected light is phase conjugated) would be more practical for biomedical applications. This has been shown to be feasible for absorption contrast by Lai et al. using a photorefractive crystal based phase conjugate mirror and at millimetre-scale resolution. [6] Its feasibility in our setup would be primarily bound by the previously discussed photon budget considerations which can be estimated with photo transport models (building upon, for e.g., diffusion theory, Monte Carlo simulation [7]) that incorporate all of the factors described above.

Time reversal peak-to-background ratio

We will discuss the time reversal peak-to-background ratio (PBR) in two scenarios—one in which the number of optical modes probed and time reversed is hardware-limited and the other which is limited by signal detection .

In the hardware limited regime, the PBR is related to the number of independent controls on the phase conjugate mirror and the number of optical modes at the focus (see chapter 3). In TRUE experiments, because of the larger number of optical modes in the ultrasound focus, the PBR of the time reversal focus is low. The PBR is expected to decrease further with increasing scattering. We teased out the in focus fluorescence signal from the background contributions using an adaptive background subtraction method. This is effective for optical imaging and sensing applications. However, the background light intensity can be particularly undesirable in optical manipulation applications, for example in spatially targeted optogenetics and photoablation. There are two straightforward ways to increase the PBR: (1) increase the number of independent controls on the DOPC, and (2) decrease the number of optical modes at the ultrasound focus.

With the development of larger format spatial light modulators (SLMs) and digital cameras, the increase in number of controls on the DOPC is foreseeable. It is also possible to multiplex SLMs and cameras to achieve the same aim. We do not exclude the possibility of improvement in nonlinear materials or gain media that may allow high reflectivity optical phase conjugation while providing innately high numbers of degrees of freedom. Some work in this direction has recently been reported, although the gain is still rather modest. [8] The decrease in number of optical modes at the ultrasound focus can simply be achieved by increasing the wavelength of the laser source or using an ultrasound transducer that produces a smaller focal size (i.e. a resolution improvement is couple to a PBR improvement). We note that the latter is effectively the case in TROVE, where the computationally derived phase conjugate field focuses to one optical speckle, although the acquisition time is an important trade-off.

We also point out here that the current framework for the calculation of PBR and its decay assumes that the scattering of light through the sample can be characterized by a matrix with independent, uncorrelated random elements. In highly forward scattering

biological samples, this framework serves as an estimate. It would be beneficial to extend this framework to samples with non-negligible correlations and relate these correlations to the commonly used parameters that describe scattering (e.g. scattering anisotropy).

At the ultimate limit where the number of wavefront controls is not hardware limited, we expect the achievable PBR will be SNR limited (i.e. the number of optical modes measured and time-reversed is fundamentally limited by the number of photons detected). Because it is critical to the ultimate system limitations and performance, future work should include careful investigations on the system's detection SNR and its relation to the phase measurement accuracy and thus phase conjugate fidelity.

Potential applications

With continued improvements, we believe the methods presented in this thesis could potentially applicable to extend the applicability of many optical methods to depths that are currently prohibitive. Beyond fluorescence imaging, TRUE and TROVE can be extended to other forms of optical contrast (e.g. Raman spectroscopy, intrinsic fluorescence, second harmonic) at depths that are inaccessible by conventional optical modalities. This can ultimately broaden the utility of optical methods to the study of thick tissues, small organisms and animal models, and even to medical diagnosis.

Beyond imaging and sensing applications, the ability to deliver confined light deep into tissues can also benefit optogenetics where depth penetration of light is currently a significant limitation. Because of this limitation, optogenetically modified deep brain structures are currently only accessible through fiber implantation, which causes significant tissue damage and also limits the spatial range of manipulation. This challenge can be overcome with digital TRUE's ability to generate a high intensity optical focus that can be scanned over a wide spatial range by moving the ultrasound focus. This advantage may also find use in photodynamic therapies which are currently also limited to superficial tissue layers due to the penetration depth of light.

Finally, the ability to focus light at high intensities may eventually extend the utility of medical laser applications to deep tissues; for example, enabling photoablation in deep tissues without injury to superficial layers and potentially minimizing scarring and risks of infection, and also enabling spatially targeted photodynamic therapy in deeper set tumors.

6.2 CONCLUSION

Realizing high resolution fluorescence imaging in scattering biological tissues is a central goal in biomedical optics. This is a tremendous challenge because tissues are highly scattering and the amount of unscattered light decreases exponentially with depth. In the methods presented in this thesis—digital time reversal of ultrasound-encoded light (digital TRUE) and time reversal of variance-encoded light (TROVE)—we instead selectively measure and phase conjugate frequency-shifted scattered light originating from an ultrasound focus to achieve focusing and fluorescence imaging in diffusive media. [9,10]

With digital TRUE, we demonstrated high intensity optical focusing and fluorescence imaging ~2.5 mm deep in ex vivo tissues. The resolution of digital TRUE is ultimately limited by the size of the ultrasound focus. In the demonstration of TROVE, we used variance-encoding to uncoupled the resolution of the ultrasound-guided time reversal focusing technique from that of the ultrasound focal width to achieve optical speckle-sized resolution (5 microns with our setup) between strong scattering media. Due to current hardware speeds, these methods are not yet mature for practical biomedical applications. In the sections above, we explored future directions for system improvements and considerations in pushing the systems to their ultimate limitations.

With the advent of faster cameras and spatial light modulators, continued system optimizations and increasing understanding of optical scattering and wavefront engineering, we believe that digital TRUE and TROVE, or variations thereof, will pave the way for the application of a wide range of optical techniques in deep tissues.

REFERENCES

1 Hajjarian, Z., Xi, J., Jaffer, F.A., Tearney, G.J. & Nadkarni, S.K. Intravascular laser speckle imaging catheter for the mechanical evaluation of the arterial wall. *J. Biomed. Opt.* **16**, (2011).

2 Draijer, M., Hondebrink, E., van Leeuwen, T. & Steenbergen, W. Review of laser speckle contrast techniques for visualizing tissue perfusion. *Lasers Med. Sci.* **24**, 639-651, (2009).

3 Lev, A. & Sfez, B. In vivo demonstration of the ultrasound-modulated light technique. *J. Opt. Soc. Am. A* **20**, 2347-2354, (2003).

4 Fowler, K.A., Hotchkiss, F.H.C., Yamartino, T.V. & Nelligan, T. Important characteristics of sound fields of ultrasonic transducers.

5 Culjat, M.O., Goldenberg, D., Tewari, P. & Singh, R.S. A Review of Tissue Substitutes for Ultrasound Imaging. *Ultrasound in medicine & biology* **36**, 861-873, (2010).

6 Lai, P., Xu, X., Liu, H., Suzuki, Y. & Wang, L.V. Reflection-mode time-reversed ultrasonically encoded optical focusing into turbid media. *J. Biomed. Opt.* **16**, 080505, (2011).

7 Wang, L.V. & Wu, H.-I. *Biomedical Optics: Principles and Imaging*. (Wiley, 2007).

8 Jayet, B., Huignard, J.P. & Ramaz, F. Optical phase conjugation in Nd:YVO4 for acousto-optic detection in scattering media. *Opt. Lett.* **38**, 1256-1258, (2013).

9 Wang, Y.M., Judkewitz, B., DiMarzio, C.A. & Yang, C. Deep-tissue focal fluorescence imaging with digitally time-reversed ultrasound-encoded light. *Nat Commun* **3**, 928, (2012).

10 Judkewitz, B., Wang, Y.M., Horstmeyer, R., Mathy, A. & Yang, C. Speckle-scale focusing in the diffusive regime with time reversal of variance-encoded light (TROVE). *Nat Photon* **7**, 300-305, (2013).

Appendix: Building a DOPC

Schematic

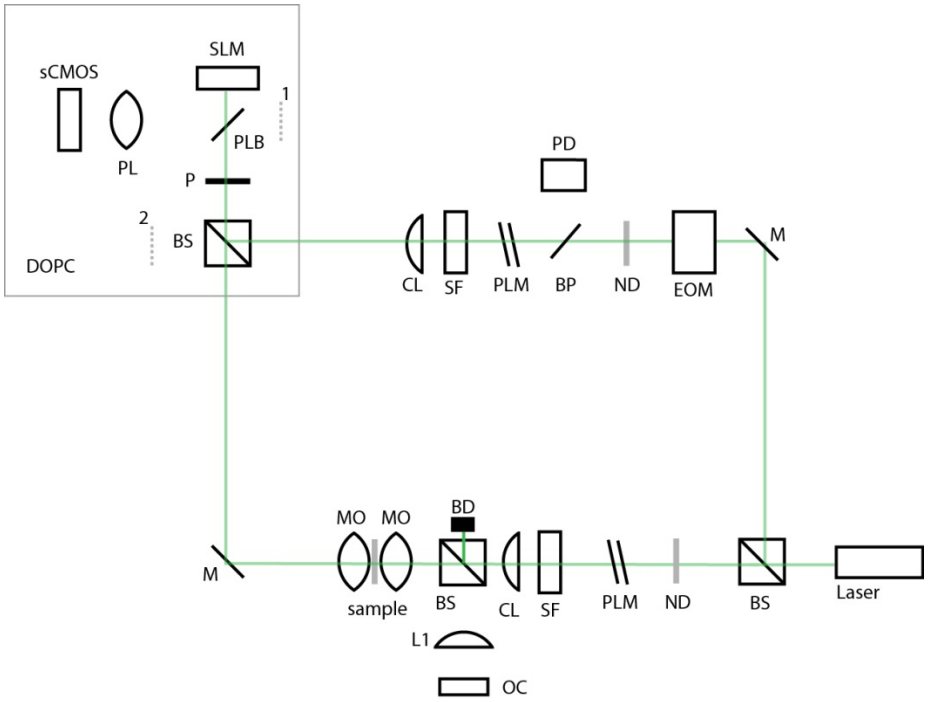

Fig. A.1 | Detailed schematic of a typical DOPC system. Abbreviations: Mirror (M), 50/50 cube beamsplitter (BS), Path length matching arm (PLM), Single-mode fiber acting as spatial filter (SF), Collimating lens (CL), 300 mm planoconvex lens (L1), Polarizer (P), Photography compound lens (PL), sCMOS camera (sCMOS), Spatial light modulator (SLM), Plate beamsplitter (PLB), Microscope objective (MO), Observing camera (OC), Beam picker (BP), Photodiode (PD), dotted lines 1 and 2 indicate positions of mirror and retroreflector (respectively) used at various points in alignment procedure (noted in text).

Materials

Here is a list of parts and materials (with suggestions for models and vendors in brackets). Note: some parts may be wavelength specific. This list assumes the use of a 532 nm source. Laser source, mirrors, mounts and mounting posts are not listed.

1. Single mode fiber (460HP, ~0.2 m, FC/APC, Thorlabs)
2. Fiber coupler (PA-X-11-A, Thorlabs)

3. Achromatic lens (50.4 mm, f = 200 mm)
4. 1-axis translation stage (UMR5.16A, Newport)
5. Plate beamsplitter (20Q20HBS.27P, Newport)
6. Non-polarizing beamsplitter (10BC16NP.3, Newport)
7. sCMOS camera (pco.Edge, PCO)
8. Spatial light modulator (PLUTO phase only SLM, Holoeye)
9. 3-axis stage (562F-XYZ, Newport)
10. Goniometer (561-GON, Newport)
11. Piezoelectric tip/tilt mirror mount (AG-M100L, Newport)
12. Objective lenses (Nikon Apo VC 20x, NA 0.75)
13. Photodetector (2001-FS, New Focus)

Procedures

A schematic of a typical DOPC is shown in figure A.1. Below is a step-by-step procedure of the alignment process. Steps in grey are non-critical suggestions. A few tips:

- Decide on a beam height and check for and maintain that height at each step. This makes subsequent fine checks for alignment easier.
- Always make sure that the beams are normally incident and at the center of the lenses.

Initial setup

The basic setup of the DOPC resembles a Mach-Zedner interferometer.

1. The output of the laser is split by a beamsplitter into two—a reference beam and a sample beam.
2. This step ensures a mechanism for phase shifting. Either the sample beam or the reference beam is directed into an electro-optic phase modulator (EOM) that has been calibrated for phase versus input voltage. Alternatively, each beam is

directed into an acousto-optic modulator (AOM), so that phase-shifting can be achieved by the relative phase delays of the driving acoustic signals. Note: AOMs are employed usually only for DOPCs integrated with time reversal of ultrasound-encoded light experiments.

3. Each beam is spatially filtered using a single mode fiber to ensure a single mode Gaussian output.
4. The reference beam is collimated with an achromatic doublet (here, we use f = 200 mm) mounted on a translation stage (for fine adjustment of collimation). Using an achromatic doublet produces less aberration in the reference beam than using a simple planoconvex lens. The choice of focal length depends on the beam size required to obtain an almost uniform illumination on the spatial light modulator (SLM) (i.e. the full width at half maximum of the collimated reference beam should be at least the longer length of the SLM).
5. This step checks for the collimation of the reference beam. Place a retro-reflector at the position indicated by dotted line 2 in figure A.1. If the reference beam is well collimated and flat, the retro-reflected beam should be optimally focused by the collimation lens, and maximally coupled and propagated back through the fiber. A beam picker (a glass slide) is placed before the fiber to direct any light back-propagating through the fiber to a photodetector (see figure A.1). Adjust the position of the collimating lens to maximize the back-propagating light power detected by the photodetector. Block the retroflector in subsequent steps.
6. The reference beam is reflected off a cube beamsplitter (that is subsequently used to interfere the sample beam with the reference beam) and is directed through a plate beamsplitter before normally reflecting off the spatial light modulator mounted on a piezoelectric tilt/tip mirror mount on a goniometer on a three-axis translation stage. This gives five degrees of freedom, which may

appear excessive but is useful for fine positioning of the SLM with respect to the camera.

7. The reflection from the spatial light modulator is further reflected off the plate beamsplitter and directed into the compound camera lens mounted on the camera.
8. The recommended camera lens has a tunable focal length (coupled to demagnification). Adjust the focal length (demagnification) such that one SLM pixel is de-magnified to the size of one camera pixel.
9. Place the SLM at the imaging distance corresponding to the correct demagnification.
10. Using the translation stage, adjust the position of the SLM until it comes into focus on camera. A good indication of this is when a $0/\pi$ checkerboard pattern displayed on the SLM exhibit sharp transitions on the camera image due to the phase jumps (see figure A.2).

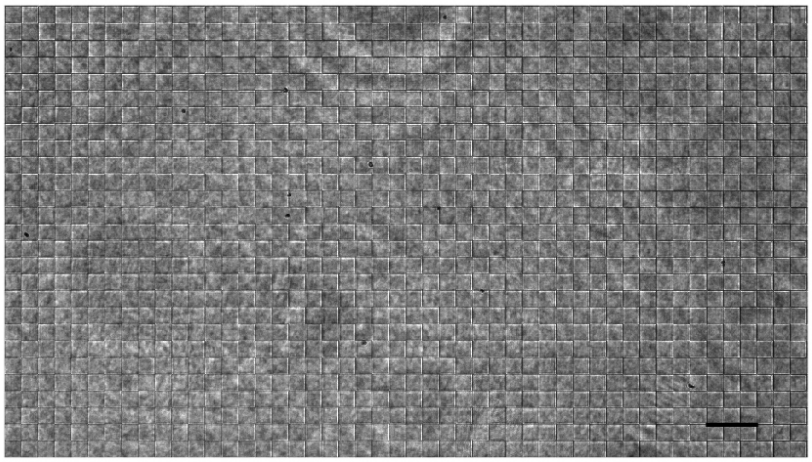

Fig. A.2 | Imaging the SLM onto the camera. A $0/\pi$ checkerboard pattern displayed on the SLM exhibits sharp transitions on the image due to the phase jumps. A representative area on the SLM is shown here. Scale bar: 60 pixels.

11. Checkpoint: place a pinhole in the path of the reference beam at the correct beam height and centered, such that a narrow beam of light is let through. Ensure that this beam of light is spot center on the SLM* and eventually spot center when imaged onto the camera. *This can be aided by displaying a $0/\pi/\pi/0$ pattern that is centered on the SLM.
12. The $0/\pi$ checker-box pattern (figure A.2) as imaged onto the camera also gives a good preliminary indication of
    a. whether the SLM is tilted with respect to the camera, by ensuring that thes lines at the sharp phase transitions are equally sharp at different regions of the SLM.
    b. whether the magnification set on the lens is right, by making sure that the active area on the SLM fits exactly into the corresponding field of view (FOV) on the camera (i.e. in this case the SLM is 1920 x 1080 and the corresponding FOV on the camera should be the same).

SLM curvature compensation

13. Since the SLM is not perfectly flat, we need to perform phase compensation. This can be done by placing a mirror at the position indicated by dotted line 1 in figure A.1. In such a way, the reflected beam provides a reference to interfere with the reflection off the SLM. Ensure that the interference pattern is to the best approximation a centered bull's-eye pattern, but keep in mind that centering is not crucial since adjustments are made in later steps. Imposing a global 0, $\pi/2$, π, $3\pi/2$ phase-shift on the SLM, we can measure its curvature using phase-shifting holography (see figure A.3). By displaying the phase conjugate of that curvature map on the SLM, we have a first approximation to the compensation of the SLM surface curvature.

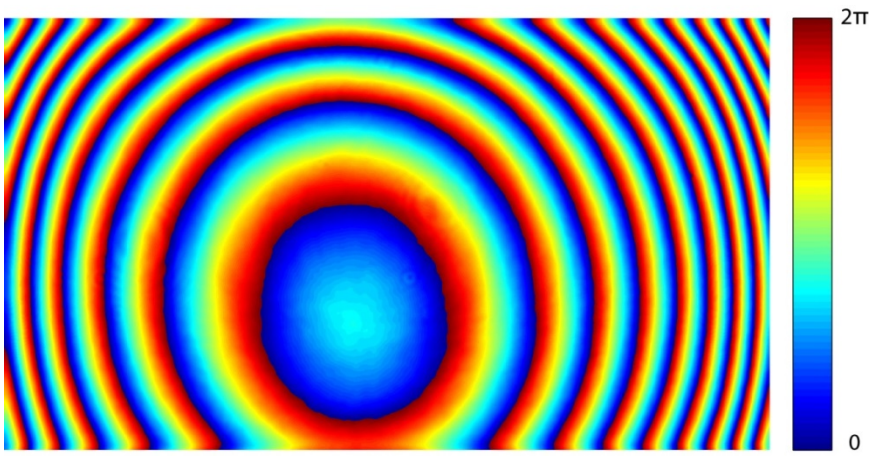

Fig. A.3 | A typical SLM phase curvature compensation map. Phase map is Gaussian blurred to remove sharp transitions. The complete phase compensation map (1920 x 1080 pixels) is shown here.

Fine alignment

14. Set the phase of isolated single pixels, at known locations, to π. Ensure that
    a. The abrupt phase changes show up as sharp "dots" (see figure A.4).
    b. The dots appear at the correct pixel locations on the camera. To ensure accuracy, observe dots at various locations on the camera.
15. Troubleshoot:
    a. If the dots do not appear sharp, adjust the SLM location and tilt to ensure that it is at the image plane.
    b. If the dots do not appear at the right pixel locations, use the translation stage to match the dots to the desired pixel locations.
    c. If there is a systematic accumulation of position errors, the magnification setting on the lens may be wrong.
    d. Note: these steps may have to be iterated to obtain a reasonable alignment. On a day to day basis, if the performance of the DOPC becomes sub-optimal, these also provide a good means to check for misalignments.

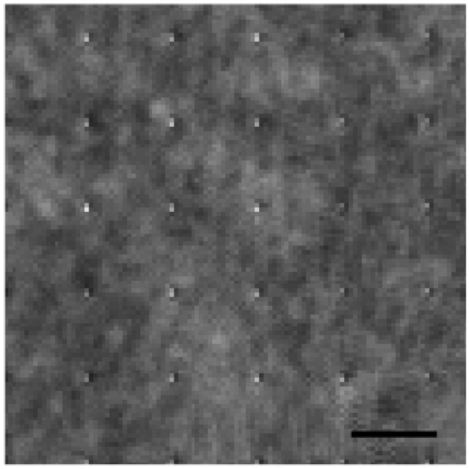

Fig. A.4 | Dots displayed and imaged for fine alignment. Representative area on camera image showing dots displayed on SLM for pixel-to-pixel alignment. Scale bar: 20 pixels.

Fine tuning the SLM phase curvature

16. By iteratively adjusting the phase offsets of groups of pixels on the SLM and measuring the light return through the fiber (like in step 5), we find the phase offsets of each group of pixels required to maximize the light returned through the fiber. This gives the additional phase offsets required to ensure flatness of the SLM. This iterative adjustment of groups of pixels can theoretically be done with any basis, we utilized the Hadamard basis to improve signal to noise ratio of the photodiode measurement. This procedure is done before every DOPC experiment.

Building the sample beam path

17. The sample beam can be similarly collimated with a planoconvex or achromatic lens and directed through a pair of objective lenses, between which the sample is placed (figure A.1).
18. A beamsplitter is inserted before the first objective lens so that the phase conjugate light that has back-propagated through the sample can be directed and focused (by a planoconvex lens) onto an observing digital camera (figure

A.1). This allows us to monitor the phase conjugate field and to measure the peak to background ratio (see chapter 3).